Dissertation
submitted to the
Combined Faculties for the Natural Sciences and for Mathematics
of the Rupertus-Carola University of Heidelberg, Germany
for the degree of
Doctor of Natural Sciences

Put forward by

Master-Phys.: Alexey Sokolov
Born in: Kingisepp, Russia

Oral examination: 29.01.2010

Charge breeding investigation in EBIS/T and collision study of ions with cold atoms for HITRAP

Referees: Priv. Doz. Dr. Wolfgang Quint
Prof. Dr. Andreas Wolf

Untersuchungen zum Ladungsbrüten in EBIS/T und Kollisionsexperimente mit kalten Atomen für HITRAP Langsame oder sich in Ruhe befindliche hochgeladene Ionen sind interessante Systeme für atomphysikalische Experimente. Für Untersuchungen an schweren hochgeladenen Ionen wurde die Ionenfallenanlage HITRAP (Highly charged ion trap) an der GSI/Darmstadt aufgebaut, die gekühlte Strahlen hochgeladener Ionen bei einer Energie von 5 keV/q liefern wird. Die hochgeladenen Ionen werden in einer Stripper-Folie bei relativistischen Energien erzeugt und im Experimentierspeicherring ESR und in der HITRAP-Anlage abgebremst, bevor sie zu den Experimenten geliefert werden. Ein Experiment ist der Mehrelektronen-Ladungsaustausch in Stößen hochgeladener Ionen mit kalten Atomen, die mit der MOTRIMS-Methode erforscht werden. Ein Stoßexperiment mit leichten Ionen aus einer EZR-Ionenquelle und kalten Atomen in einer magnetooptischen Falle als Target wurde durchgeführt und die Resultate werden dargestellt. Eine Elektronenstrahl-Ionenfalle (EBIT) für die Inbetriebnahme der HITRAP-Experimente wurde getestet und optimiert. Der Prozess des Ladungsbrütens wurde in der EBIT erfolgreich mit Edelgasen und einem Alkali-Element, das aus einer externen Ionenquelle eingeschossen wurde, erfolgreich untersucht.

Charge breeding investigation in EBIS/T and collision study of ions with cold atoms for HITRAP Highly charged ions (HCI) at low velocities or at rest are interesting systems for various atomic physics experiments. For investigations on HCI of heavy stable or radioactive nuclides the HITRAP (Highly charged Ion TRAP) decelerator facility has been set up at GSI to deliver cooled beams of HCI at an energy of 5 keV/q. The HCI are produced in a stripper foil at relativistic energies and are decelerated in several steps at ESR storage ring and HITRAP before they are delivered to experimental setups. One of the experiments is the investigation of multi-electron charge exchange in collisions of heavy HCI with cold atoms using novel MOTRIMS technique. Collision experiments on light ions from an ECR ion source colliding with cold atoms in a MOT have been performed and the results are described. An electron beam ion trap (EBIT) has been tested and optimized for commissioning of the HITRAP physics experiments. The process of charge breeding in the EBIT has been successfully studied with gaseous elements and with an alkaline element injected from an external ion source.

The machine does not isolate man from the great problems of nature but plunges him more deeply into them.

Antoine de Saint-Exupery

Contents

List of Tables

List of Figures

Chapter 1

General Introduction

Ions are of great interest for different branches of science, and of course are one of the main topic for atomic physics. They are used in a huge variety of experiments which are carried out for fundamental investigations and practical applications.

Experiments to study cross sections of electron capture and ionization in ion - atom collisions, or radiative and dielectronic recombination cross sections in ion - electron collisions have been intensely conducted for different elements and charge states, but still a huge amount of information is missing especially for heavy, highly charged ions.

Atomic properties are rather well described by relativistic quantum mechanics, however, for heavy elements the electrons in the vicinity of the nucleus are influenced by an extreme electric field and thus the quantum electrodynamical (QED) treatment has to be included to calculate accurately atomic properties, like energy levels or magnetic moments. Experiments with few-electron systems, e.g. hydrogen-, helium- or lithium- like heavy ions are of special interest because they provide a clear evidence of QED contributions increasing with higher nuclear charge Z. Such systems provide direct access to the deeply bound states and allow very sensitive comparison of experiment and QED theory. In bound electron g - factor calculations an important term is $Z\alpha$, where $\alpha \approx 1/137$ is the fine-structure constant. The term comes closer to unity with increasing nuclear charge and thus non - perturbative theoretical techniques should be employed in the calculations. So, high-precision g - factor measurements provide an unique test for the theory and calculational techniques, and can even give higher accuracy of several fundamental constants (like m_e), nuclear magnetic moment and radius.

The creation of ions for the above experiments is a separate field of research. As one goes further up in ion production along the periodic table from the lightest element, hydrogen, removing more and more electrons from the atom needs higher energy and more complicated setups.

A possibility for the production of intense beams of highly charged ions (HCI) is offered by large accelerator facilities, like GSI, where singly or mul-

tiply charged ions can be accelerated up to few GeV/u and passed through a stripper foil which removes electrons. A typical kinetic energy of ions for HCI production at GSI is 400 MeV/u. The energy can be decreased in the Experimental Storage Ring (ESR), after the stripping, down to a few MeV/u. For some kinds of high-precision atomic physics experiments, like g - factor measurements, the ions should have at most several keV/u kinetic energies[1]. To achieve such low velocities one should further decelerate the ions. That is done in a unique facility called HITRAP [Klu05] which will be able in the future to decelerate heavy highly charged ions like bare uranium down to 6 keV/u in the amount of several 10^5 ions every 10 seconds. A description of the status and the design of the HITRAP facility and an overview of the experimental programme are given in the 2nd chapter. The HITRAP facility will be used for ion-atom collision experiments at low velocities, which are the topic of the 3rd and 4th chapter and for precise measurements of the bound electron g - factor in hydrogen-like ions (e.g.$U^{91+}, Pb^{81+}, Bi^{82+}$), of hyperfine transitions and there lifetimes [Vog05, Klu07, Qui08] and for mass measurements [Her06].

The electron beam ion trap/source (EBIT/S) devices offer a possibility for low- and medium-Z highly charged ion production. During this work intense study of two different ion sources was done. The first source, MAXEBIS, was a powerful device with superconducting magnet and 3 A - electron gun, the second was a SPARC[2] EBIT with permanent magnets and 50 mA - electron gun. Charge breeding in these sources was investigated and showed individual peculiarities for each charge breeding apparatus. An overview on the EBIT/S devices in total can be found in chapter 5. The design and parameters of two studied ion sources and possibilities to increase the amount of ions in a certain charge state for further applications are described in the 6th chapter,

Electron cyclotron resonance ion sources (ECRIS) offer another possibility for ion production, one of such a devices was used in the ion - atom collision experiment. A short overview on the basic principles of ECR ion sources is given in the 5th chapter. Additionally two singly charged ion sources: a sputter ion gun and a surface ion source used for this thesis are briefly mentioned in the same chapter.

The easiest way of HCI production in the EBIS/T devices is to inject a gas into the ionization chamber where the atoms are stripped via electron impact ionization, this makes the number of elements to be produced in highly charged states limited. To increase the number of available elements from these devices one can inject externally singly charged ions, which can be captured in the ionization region and further charge bred up to certain charge states. Increasing the charge state is in principle also possible for rare isotopes which can be further extracted and delivered to experimental setups or to a post ac-

[1]During the high-precision measurements themselves the ion energy is only a few meV, which is achieved by electrostatic deceleration, electron or (and) resistive cooling.

[2]The EBIT is a part of the SPARC project (Stored Particles Atomic Physics Research Collaboration).

celerator facility. Our successful charge breeding experiment with the SPARC EBIT will provide the HITRAP project with numerous low Z HCI for measurements. The possibilities and techniques of charge breeding are discussed in the 7th chapter with experimental results and conclusions.

The main contributions of this work were done in the commissioning of the HITRAP decelerator facility, preparation to the low energy HCI - atom collision experiments and installation of the electron beam ion trap for future off - line measurements and testing of the low-energy section at HITRAP. Additionally in this thesis ion optical simulations for different optical elements and setups dedicated to the HITRAP project are included. Results of simulations are presented in several chapters.

Chapter 2

HITRAP

2.1 Overview

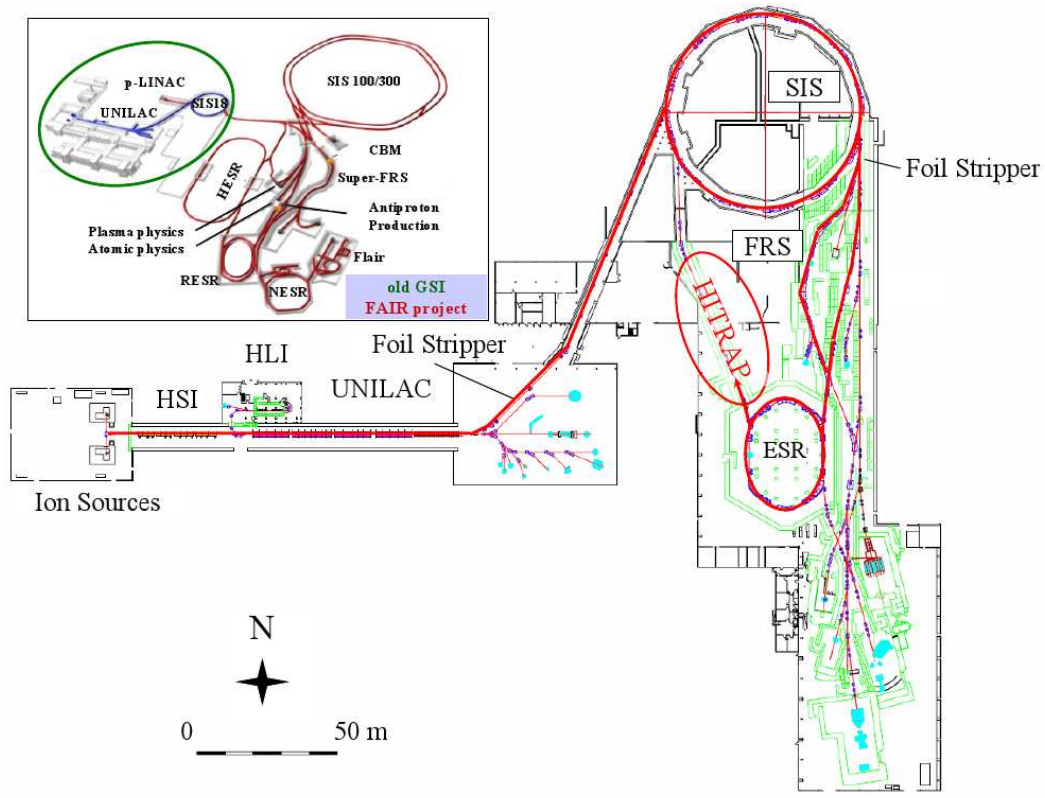

Figure 2.1: Overview of the GSI accelerator complex, which includes Ion sources, UNILAC and SIS-18, where ions are produced, accelerated and stripped. FRagment Separator (FRS) is used to select the radioactive isotopes produced in nuclear reactions. In the Experimental Storage Ring (ESR) the first deceleration and cooling takes place. Afterwards the beam is transported to the HITRAP facility.(GSI-webpage)

HITRAP is a facility for deceleration of HCI with $M/q \leq 3$. In the following one can find a description of the HITRAP project. In fig. 2.1 the GSI accelerator complex is sketched. The ion production starts in the (CHORDIS, MUCIS, MEVVA) setups which are huge arc discharge ion sources producing different elements in singly or lowly charged states (up to U^{4+}). The acceleration starts (see Injector Group webpage) in the UNIversal Linear ACcelerator (UNILAC). A high current injector (HSI) section consisting of a Radio Frequency Quadropole (RFQ) and a couple of Interdigital H-type (IH) - structures (see IH-structures section) are used for primary acceleration of ions to pass the gas prestripper where they lose there electrons in collisions with a gas. After the prestripping section, multiply charged ions (like U^{28+}) are injected into a 4 - fold linear accelerator (Alvarez) on the exit of which they obtain a kinetic energy of 11.4 MeV/u. Additionally to the HSI there is a highly charged ions injector (HLI) which consists of an ECR ion source and RFQ - IH combination to preaccelerate ions before injection into the Alvarez. After the 4-fold linear accelerator ions at 11.4 MeV/u energy pass through a foil stripper where they obtain higher charge states, the most abundant charge state for uranium ions is 73+. After the UNILAC the HCI are sent to the heavy ion synchrotron (SIS-18) which is a circular accelerator capable of increasing the ion's kinetic energies up to 1 GeV/u. After the SIS-18 the ions can impinge either on a target to be stripped further or on another target for production of rare isotopes. For example in case of U^{73+} at 400 MeV/u the $40\mu g/cm^2$ copper target can give a 30 % stripping efficiency in production of bare uranium [Dah04]. The necessary charge species are selected and in case of rare isotope production the FRagments Separator (FRS) is used.

Then the beam is transported to the first deceleration stage, i.e. the Experimental Storage Ring (ESR). The ESR (see fig. 2.2) is designed mostly for high energies, thus the bending magnets and the RF-systems are not adjustable to the required parameters and allow deceleration only down to 3 MeV/u, which is already 2 orders of magnitude less in energy. Of course, the ion beam suffers higher and higher losses when decreasing energy. The 4 MeV/u energy was chosen to satisfy the low energy requirements and sufficient intensity of the beam for injection into the HITRAP facility. The deceleration in the ESR happens in two steps separated by a 5 s electron cooling at 30 MeV/u energy. The beam is also cooled right after the injection into the ESR for 10 s and before the extraction (time is dependent on the energy and emittance optimization). To speed up the cooling process the electron cooling can be exchanged (or applied in parallel) with stochastic cooling [Mar04]. The time necessary to decelerate and cool the ion beam is presently around 40 s; after that time a 1 μs bunch of approximately $5 \cdot 10^5$ (for U^{92+}) ions can be injected into the HITRAP decelerator.

The full HITRAP facility is represented in fig. 2.3. The ion beam from the ESR is transported first through a Double-Drift Buncher (DDB) where the RF - cavities form short bunches of the beam before injection into the

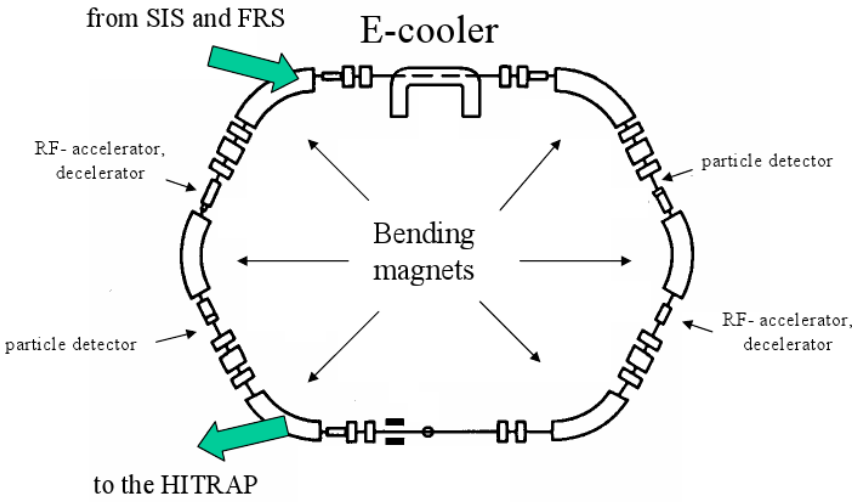

Figure 2.2: Experimental Storage Ring (ESR).

IH - structure. The IH - structure decelerates the ion beam from 4 MeV/u down to 0.5 MeV/u. The next deceleration stage is performed in the Radio - Frequency Quadrupole (RFQ) which slows the ions down to 6 keV/u. Table 2.1 summarizes the main parameters of the mentioned sections.

Table 2.1: Ion beam energies, transmissions and normalized emittances[1] ϵ before and after different sections of the HITRAP decelerator.

	DDB	IH	RFQ
Entrance energy [MeV/u]	4	4	0.5
Exit energy [MeV/u]	4	0.5	0.006
Normalized $\varepsilon_{xx'(yy')}$ entrance [mm mrad]	0.2	0.21	0.34
Normalized $\varepsilon_{xx'(yy')}$ exit [mm mrad]	0.21	0.3	0.36
Transmission [%]	98	70	85

As the HCI have big electron capture cross section at small velocities in collisions with the residual gas molecules, the vacuum conditions should be drastically improved after the RFQ to be less than 10^{-10} mbar. This is done in the Low Energy Beam Transport (LEBT) section, where electrostatic lenses

[1]The normalized emittance is the emittance multiplied by $\beta\gamma$ [Gru03], where β and γ are the Lorentz factors.

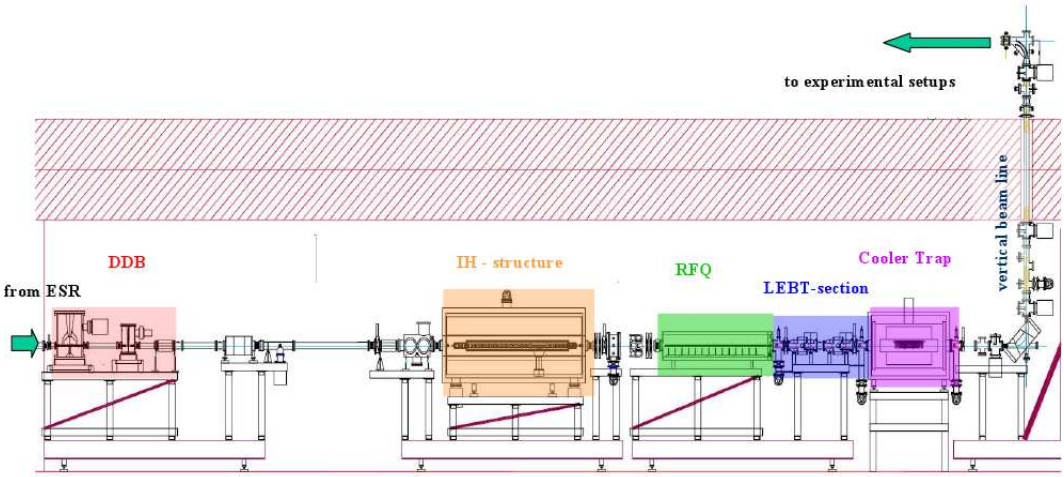

Figure 2.3: The HITRAP beam line include the ground floor with decelerator facility itself and the first floor with experimental setups. The decelerator consists of several sections, i.e. Double-Drift Buncher (DDB), Interdigital H-type linac (IH-structure), Radio Frequency Quadropole (RFQ), Low Energy Beam Transport section (LEBT) and Cooler Trap (see description in the text). After the Cooler Trap the ion beam will be transported to the first floor via the vertical beam line and delivered towards different experimental setups.

focus the beam through small diaphragms used for differential pumping. The other task of the LEBT is to focus the beam into the magnetic field of the Cooler Trap - a cryogenic Penning trap, where electron cooling down to 10 eV and resistive cooling down to 4 K are applied to improve the beam quality after deceleration. From the Cooler Trap the ions are sent to the upper floor towards the experimental setups.

The HITRAP facility will be also used to slow and cool down not only highly charged ions, but also antiproton beams at the FAIR project (see the insertion in fig. 2.1). Thus the experiments with low - energy antiprotons will be available, like antiproton g - factor measurements or antimatter (e.g. anti - hydrogen) - matter collision research.

2.1.1 Double-Drift Buncher

The $1\mu s$ pulse from the ESR of HCI is too long for efficient deceleration in the IH-structure (see next subsection) operating at high frequency with a period of 9.2 ns. To increase the efficiency, the ion pulse should be bunched correspondingly to match the deceleration period. This is done with four- and two-gap RF cavities in the DDB section (see fig. 2.4) operating at 108.408 MHz and 216.816 MHz respectively [Bei03]. The four-gap buncher was chosen because of it's moderate need of RF power, only up to 2 kW. The second buncher "helps" the first one to form rectangular ion beam pulses before injection into

the IH-structure, with similar RF power below 2 kW.

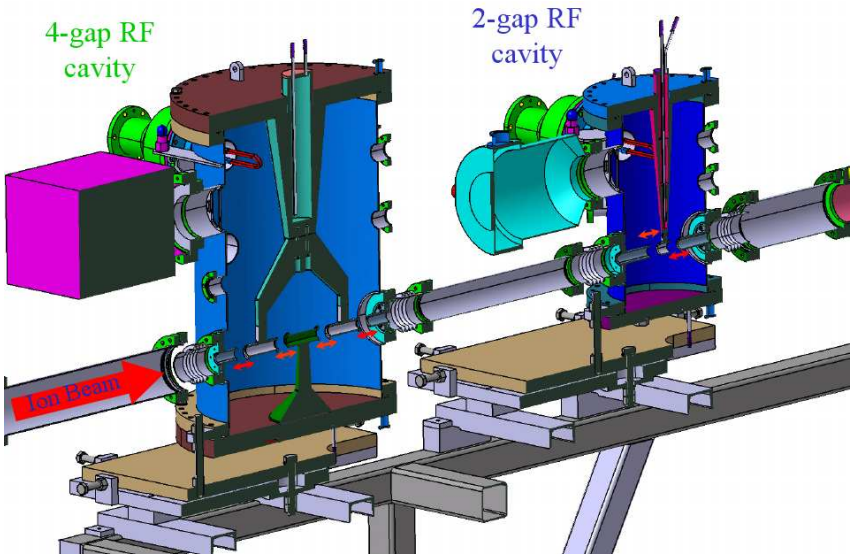

Figure 2.4: Four- and two-gap RF cavities of the Double-Drift Buncher (DDB), operating at 108.408 MHz and 216.816 MHz, respectively.

The DDB was installed in 2007. In the same year two beamtimes with $^{64}Ni^{28+}$ and $^{20}Ne^{10+}$ ion beams were conducted to commission the bunchers. In those experiments the beam transmission, the bunch length and the emittance after the RF cavities have been measured. The transmission was obtained from comparison of the ion beam currents on Faraday Cups[1] (FCs) before and after the DDF section. The current-to-voltage converter (CVC) was used to convert and amplify the signal from the FC, the signal was afterwards monitored on an oscilloscope fig. 2.5. The transmission was measured to be 80% and thus slightly less than expected. This was due to the lack of cooling in the ESR and thus increased emittance in comparison with the designed value.

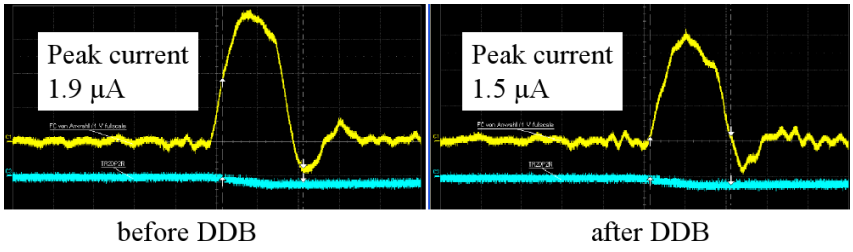

Figure 2.5: Comparison of the ion current on FCs before and after the DDB section. Signals on the oscilloscope.

[1]Along the beam line up to the RFQ several FCs and scintillator (Yttrium aluminium garnet - YAG) screens were installed to allow current and beam profile measurements.

Before the run the pepper-pot emittance meter [Zha96] was installed after the DDB. The emittance was mostly the same with and without RF power, as expected [Pfi09].

The bunch monitoring was performed with a couple of phase probes - short electrodes on which the image current from the passing by ion beam is induced, and additionally with a poly-crystalline diamond detector[1] [Koz08] which showed nicely resolved time structure of the beam with expected 9.2 ns period (fig. 2.6). Thus the DDB section was completely commissioned and aproved to have the designed parameters, i.e. high transmission, independence of emittance (for On and Off cases) and bunched beam. Later on, during next runs, the emittance after the DDB was measured for the cooled beam from the ESR using a multi-gradient-method (described in [Kes92], see Appendix C) and was around 0.2 π mm·mrad (normalized value) and even less, dependent on the cooling in the ESR [Pfi09].

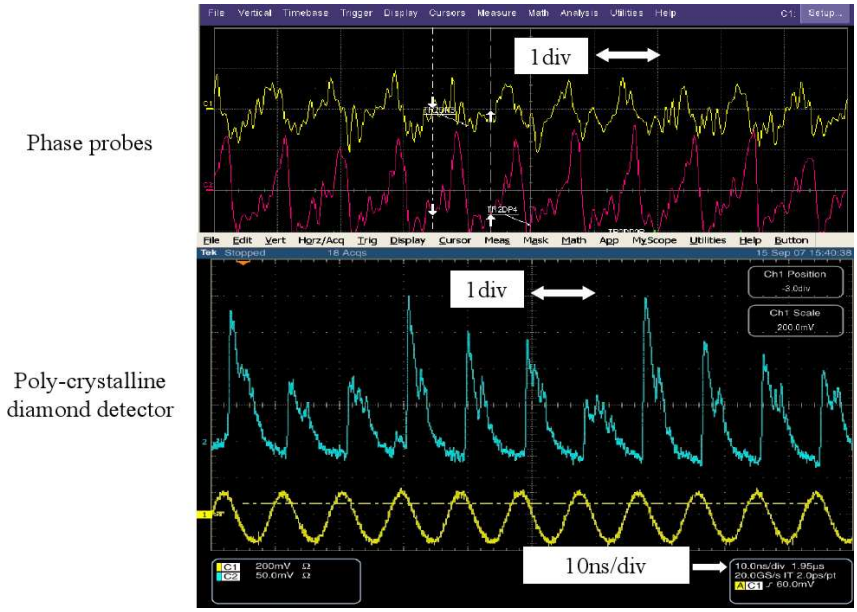

Figure 2.6: Signals on the oscilloscope after the DDB from the phase probes and poly-crystalline diamond detector.

[1]During this work two diamond detectors were used. The first was a poly-crystalline diamond detector composed of aggregates of individual crystals and sensitive to intense ion beams. The second was a single-crystal diamond detector which was sensitive to single ions. Both detectors had 3 mm diameter of active area. The impinging ion creates electron-hole pairs in the detector, which are separated under applied voltage and create a signal on the end cap electrodes. Due to the high electron and hole mobilities in the bulk of the crystal the response of the detectors is very fast.

2.1.2 IH-structure

After the double-drift buncher the ions are decelerated from 4 MeV/u down to 0.5 MeV/u with the IH - structure. The decelerator (fig. 2.7) is essentially a quarter-wave coaxial line. The 25 gaps between which the RF-field of 108.408 MHz frequency is applied are progressively decreasing along the beam-flight direction. This is done to fit the neccessary RF phase to the decelerated beam bunch appearence between the gaps. Between the first 15 gaps of the high energy section and the 10 gaps of the low energy section a quadrupole triplet is integrated to focus the transversely expanding beam. The IH - structure can be operated up to 200 kW RF-power to apply 10.5 MV overall effective voltage neccessary to decelerate the ions.

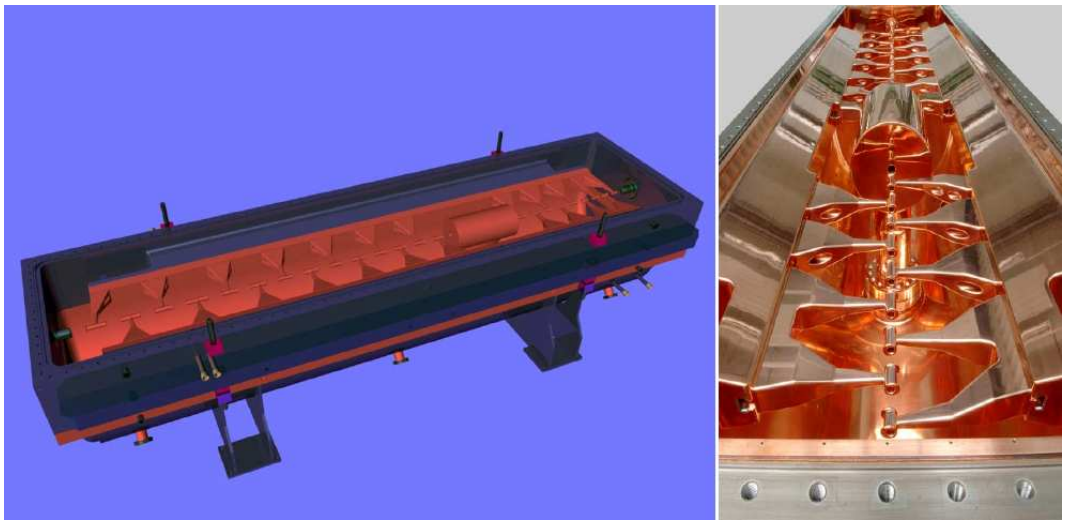

Figure 2.7: Interdigital H-type (IH) structure.

Several beamtimes were conducted to test the IH-structure. In order to analyze the ion beam after the deceleration a single crystal diamond detector (SCDD) was used, which produces from a single ion a signal that is proportional to the ion's energy. Additionally for the energy separation a magnetic steerer (dipole) was installed after the IH - structure in front of the SCDD. To map the energy spread of the beam the detector was moved with a step motor perpendicularly to the beam axis and to the magnetic field lines. Signals from ions close to the geometrical axis (4 MeV/u) and several mm off-axis (0.5 MeV/u) have been monitored on the scope and can be seen in fig. 2.8. Signal widths were more or less the same and the main parameter to estimate the ion energy was the amplitude. On the pictures from the scope one can see a clear difference in amplitude for 4 MeV/u and 0.5 MeV/u ions. For the settings used during the run in February 2009 the decelerated fraction of the beam, obtained after the scan perpendicular to the axis, was only 12% from the total 70% of the beam transported through the IH (measured with FCs).

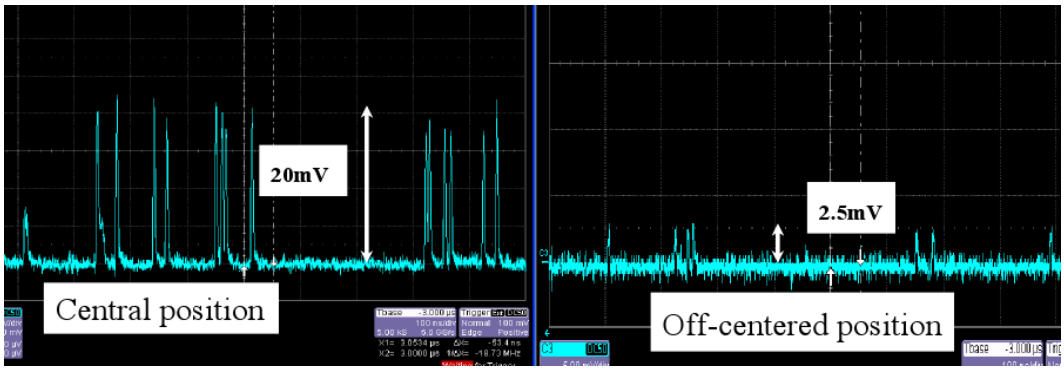

Figure 2.8: Signals from the single crystal diamond detector measured after the magnetic steerer on-axis (high energy beam, 4 MeV/u) and off-axis (decelerated beam, 0.5 MeV/u). Amplitude of the signal is proportional to the kinetic energy of the impinging ion.

During the run in April 2009 the beam line settings were tested again. This time the ion signal in the SCDD was still proportional to the energy, but due to the defects in the crystal not to the signal's amplitude anymore, thus one had to integrate the areas under the peaks. Histogram of the areas is depicted in fig. 2.9, though obtained with slightly damaged detector and less resolution, the figure is close to the simulations performed for the IH-structure [Cle08]. Estimated from the measurements deceleration efficiency thus is around 25%.

The emittance measurement for 0.5 MeV/u ion beam was difficult to perform, but the estimated from 3-gradient method normalized value was around 0.3 π mm·mrad [Pfi09]. A difficulty to measure the emittance comes from the mixture of different energies after the IH and thus not clearly defined 0.5 MeV/u beam. The energy selection will be done in the future by a dipole magnet after the IH-structure.

The test of the IH showed expected transmission and emittance, the deceleration efficiency (25%) was less than expected, but still the settings are not the best in the moment and efficiency of 70% is expected.

2.1.3 RFQ and LEBT section

The radio frequency quadrupole (RFQ) is the next deceleration stage from 0.5 MeV/u to 6 keV/u (fig. 2.10, left). The design and simulations for the RFQ were the topics of the PhD thesis [Hof07]. Right before the RFQ a Re-Buncher is installed, a 2-gap RF-cavity, to restore the bunched structure of the beam. The RFQ itself is essentially a 4-rod structure with a specially modulated profile along the beam direction. Two rods are schematically drawn on fig. 2.10, right. The ion beam moving along the axis is radially confined in the harmonic potential well created by high RF voltage (up to 77.5 kV) with a frequency of 108.408 MHz. Longitudinally the beam is effected by the

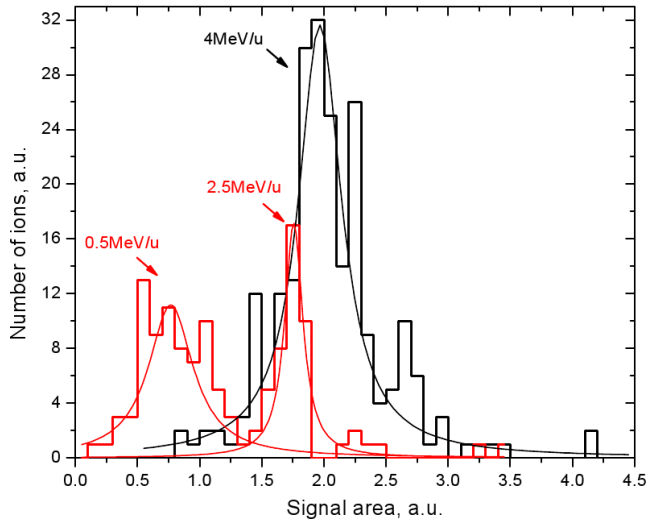

Figure 2.9: Analysis of the ion signal areas on the SCDD after the IH-structure. The single peak (black histogram) corresponds to 4 MeV/u ion beam after the IH with RF power switched off. The double peak structure (red histogram) is obtained with RF power on. Two peaks are assumed to be from 2.5 MeV/u and 0.5 MeV/u energy beams as it was predicted in simulations [Cle08].

non-perpendicular component of the electric field which decelerates the beam the same way as in the IH-structure. The modulation along the axis changes to fit the phase of the slowing down, bunched beam to the appropriate phase of the RF voltage. After the quadrupole another 2-gap RF cavity (De-Buncher) is mounted to decrease the energy spread of HCI, for better injection into the Cooler Trap.

The ions after the RFQ are guided through the Low Energy Beam Transport line equipped with 6 electrostatic Einzel lenses for focusing. Two lenses in the very beginning and at the end of the LEBT are called LEBT adapters and both have 4-sigmented electrodes for steering. Other four lenses are specially designed for high voltage (around -40 kV) to focus the ion beam through the two diaphragms. As it was mentioned the diaphragms are neccessary for differential pumping down to 10^{-11} mbar before the Cooler Trap.

The LEBT section is equipped with a couple of KVI diagnostics each containing a FC and a special Multi-Channel Plate (MCP) - phosphor screen combination[1], because the phosphor screen alone is not sensitive to the low energy ions. The FC current measurements showed a good transmission of the beam through the RFQ during the run in April 2009. The beam profile was also seen on the MCP-phosphor screen combination as well as on a recently designed [Pfi09] MCP-based pepper-pot emittance meter, temporally integrated

[1]MCP is essentially an ion beam amplifier producing and accelerating numerous electrons along a small (diameter $\approx \mu$m) tube as soon as the ion hit the surface. The electrons pass through the channel and hit the phosphor screen producing the light detected with a camera.

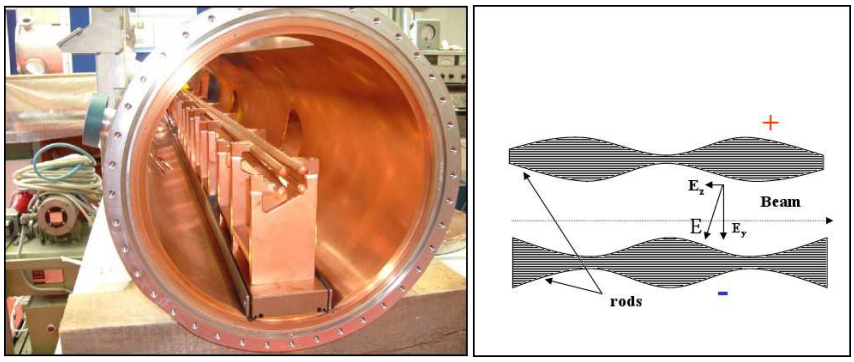

Figure 2.10: Photo of the radio frequency quadrupole (left) and two rods of the RFQ (right) to explain the main principle of the deceleration.

into the line. The beam time was the first RFQ test and thus it is too early to speak about the emittance, energy distribution and overall decelerated to 6 keV/u ion beam transmission at the exit.

2.1.4 Cooler Trap and beam line to experiments

The ions after deceleration from 4 MeV/u down to 6 keV/u have a huge energy distribution and thus cooling of the beam is required to decrease the ions phase space distribution. For that purpose the beam is injected into the Cooler Trap where the ions are trapped with magnetic and electric fields. Immediately after confinement electron cooling [Zwi06] and afterwards resistive cooling [Mae08, Vog05] are applied. The Cooler Trap was a topic of two PhD thesises [Mae08, Kos09]. Below a short overview of the device operation is given.

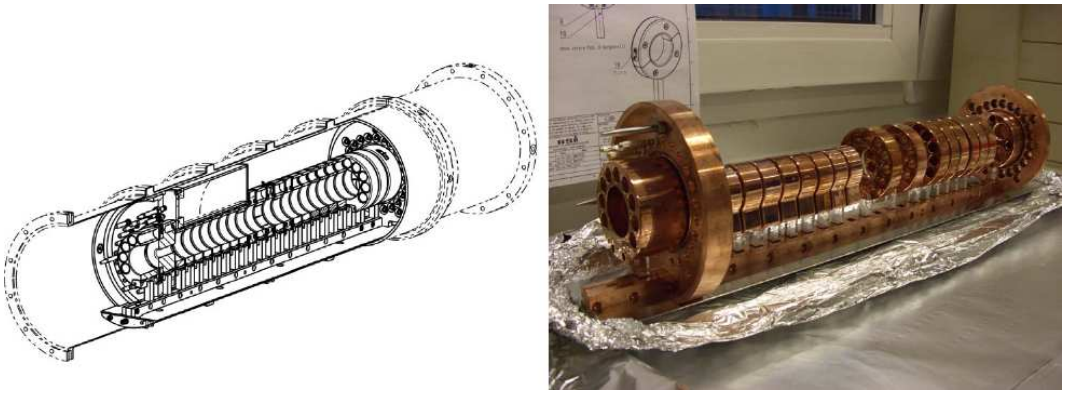

Figure 2.11: Technical drawing and photo of 25 stacked electrodes for the Cooler Trap.

The apparatus essentially is a stack of 25 electrodes (fig. 2.11) inserted into a 6T superconducting magnet. The cooling cycle starts with the creation

of $10^9 \div 10^{10}$ electrons by illumination of a photo-cathode with a laser. The electrons at around 100 eV energy are guided from the cathode towards the trap where they are confined radially in the magnetic field and longitudinally in the electric field. Via synchrotron radiation the electrons are cooled down to the environment temperature of 4K (<1meV energy) within 5 s[1]. After the cooling appropriate potential (few volts) is applied to the middle electrodes to create nests (two or more) where the electrons are located during the ions injection. When the ion bunch from the ESR arrives, potential on the first electrode is lowered to allow for injection. As the ions are inside the Cooler Trap the entrance potential is ramped up and the ions are confined in the trap. Via Coulomb interaction with cold electrons the ions are cooled to 10 eV energy. At this energy electrons and ions are separated to prevent recombination. Charge exchange of the HCI with the residual gas in the Cooler trap is very low due to the pressure $< 10^{-13}$mbar provided by the cryogenic surrounding. During the second stage of the cooling a harmonic potential is created in the center of the trap, in which the ions oscillate and dissipate their energy via image currents induced in resistive circuit [Kos09]. Resistive cooling is limited by thermal (Johnson − Nyquist) noise, thus the electronics is also kept in the cryogenic environment. After the last cooling stage (1÷10 s) the ions are swept from the Cooler Trap towards the vertical beam line.

The vertical beam line is dedicated to transport the HCI to different experimental setups and is under construction in the moment. At first the ions are separated by charge state with a 90° dipole bending magnet. After a couple of diagnostics (FCs and MCP-phosphor screen combinations) and several electrostatic optical elements (quadrupoles and Einzel lenses) the ion beam is sent back (on the first floor) to the horizontal plane with an electrostatic kicker bender.

The variety of the setups on the first floor starts with an EBIT which is the topic of the 6th and 7th chapter. The ions from the EBIT will be delivered via the vertical beam line to the Cooler Trap for commissioning of the trap. Additionally the EBIT will be used as off-line ion source for different experiments.

2.2 HITRAP experiments

2.2.1 g - factor measurements

The HITRAP facility will open an opportunity for the g - factor (g_J) measurements [Klu05] of the bound electron in "simple", single electron systems, like

[1]The exponential decay of the temperature via synchrotron radiation is determined with a time constant $\tau = 3\pi\epsilon_0 \frac{m_e^3 c^3}{e^4 B^2} \approx 0.1s$, where ϵ_0 is the dielectric constant, m_e and e are the electron mass and charge, respectively, c - the speed of light and B is the magnetic field strength.

hydrogen-like uranium. As the theoretical quantum electrodynamics (QED) contribution to the g - factor is increasing with higher Z, nucleus charge, the experiments can provide a test for the QED itself, because the precision of the measured g - factor is very high. The modern setups are able to reach an uncertainty of 10^{-9} for hydrogen-like carbon [Hae00], hydrogen-like oxygen [Ver04] and hydrogen-like calcium [Qui05].

For future measurements a single ion will be captured in a g - factor trap developed by a Mainz-GSI collaboration. The trap consists of stacked electrodes and, as proper static potentials are applied, two harmonic potential minima can be formed dividing the trap into two parts: the precision and analysis sections. In the first section (precision trap) with a very homogeneous magnetic field the cyclotron frequency ω_c is determined from the induced image current. In the second section (analysis trap) the electron's Larmor (spin precession) frequency ω_L is obtained. In this section a quadratic inhomogeneity with a minimum of the magnetic field corresponding to the minimum of the harmonic electrostatic potential is introduced. The Larmor frequency is measured from the rate of spin flip transitions which are induced in the precision trap via microwave excitation. The rate is higher when the microwave frequency is closer to the Larmor frequency. After the precision trap the ion is transported to the analysis trap. The projection of the ion magnetic moment on the z axis (μ_z) is different for electron spin up and spin down. This introduces a difference in force proportional to the product $\mu_z(\partial B/\partial z)$ acting on the ion in the analysis trap. The axial oscillation frequency in the combination of electric and magnetic fields is thus shifted for different spin directions, indicating a spin flip transition. The frequencies are obtained from the Fourier analysis of the induced image current. As soon as the frequencies ω_L and ω_c are known, from equations:

$$\omega_c = \frac{q}{M}B \tag{2.1}$$

$$\omega_L = g_J \frac{e}{2m_e}B \tag{2.2}$$

where M and m_e are the ion and the electron masses, respectively, q is the ion charge and B the magnetic field strength, the g - factor (g_J) of the bound electron can be calculated:

$$g_J = 2\frac{q}{e}\frac{m_e}{M}\frac{\omega_L}{\omega_c}. \tag{2.3}$$

2.2.2 Mass measurements

Another kind of experiment will be ion mass measurements. The nuclear mass is of high interest, since it provides information on the nuclear structure and Q-values[1] of different processes. High precision mass measurements can also

[1]Difference in mass between the mother and daughter nuclei.

provide knowledge on the total electron binding energies from the difference between the different ion charge states.

Precise mass measurement can be obtained in Penning traps [Bla06] and reach relative uncertainties as low as $\delta M/M \approx 10^{-11}$ [Her06], which means for a heavy ion only few eVs. One of such devices is being built in Heidelbeg and will be later used at the HITRAP facility.

The main idea of the mass measurement is to obtain the frequency of the ion cyclotron motion (eq. 2.1) in the Penning trap, where the ion is confined longitudinally with an electrostatic harmonic potential and radially with a magnetic field. The frequency can be measured directly in the trap, detecting the image current induced by the ion in a special circuit [Bla06] and performing Fourier analysis, or using a time-of-flight technique [Gra80], applied for example at SHIPTRAP at GSI [Blo06]. The TOF method implies the resonant RF excitation of the ion motion in the trap and further extraction into a region with a magnetic field gradient. When the RF excitation matches the cyclotron frequency, the ion obtains a high orbital momentum and thus higher accelerating force in the magnetic field gradient.

From eq. 2.1 one can see that the frequency and thus the precision of the mass measurement are proportional to the charge of the ion, this fact makes HCI the best candidates for precision mass measurements.

2.2.3 Laser spectroscopy

The hyperfine splitting (HFS) of a hydrogen-like ion in the 1s ground state is in the first approximation proportional to $Z^3 g_I$, i.e. nucleus charge and g-factor. The splitting rapidly increases for heavier elements and enters the visible region for Z>60 [Bei00]. As the magnetic dipole transition probability also drastically increases for higher Z (as Z^9), laser spectroscopy becomes possible. For measurements the ions will be sent to the SPECTRAP setup, which is essentially a cryogenic Penning trap with optical access for laser spectroscopy and fluorescence detection. There the ions will be cooled via resistive cooling down to 4K temperature to reduce the Doppler shift and broadening. To obtain the HFS the laser parallel to the magnetic field will excite the transitions in the ion ensemble and the fluorescence signal will be measured in the perpendicular direction. The precise measurement will provide information on the nuclear magnetic moment and can be used to test QED.

Another setup is a g-factor trap, which is also a cryogenic Penning trap, but will imply a laser-microwave double-resonance technique [Qui08]. The technique is mainly a pump-probe method. By optical pumping one of a Zeeman split HFS level will be continuously excited and the fluorescence from the decay will be measured. The ions will be irradiated additionally with a microwave (probe) and, as soon as its frequency will fit the Zeeman splitting, the fluorescence signal from the pumping laser will have a dip in the frequency

dependence. The resonance will give the g_F-factor of the ion. From equation:

$$g_F = g_J \frac{F(F+1) + J(J+1) - I(I+1)}{2F(F+1)} - \frac{m_e}{m_p} g_I \frac{F(F+1) + I(I+1) - J(J+1)}{2F(F+1)} \tag{2.4}$$

with additional knowledge of the nuclear g-factor g_I one can easily obtain the electron g-factor g_J. Thus the double-resonance technique is an alternative method for measuring the electron g-factor with high precision (around 10^{-9} [Qui08]).

In addition to the mentioned experiments, studies of the interaction of slow HCI with solid surfaces will be performed. On insulating surfaces a "Trampoline" effect is expected to be observed, when the upcoming ion charges up the insulator via electron capture and is reflected back from the positively charged surface by the Coulomb force. This will show that the neutralization process on the insulator surface cannot be completed due to a lack of electrons provided within a sufficiently short response time. Also time-of-flight secondary ion mass spectrometry will be used for studying irradiation effects in various materials including fragmentation and modification of biological systems and HCI-induced surface reactions.

An experiment of special interest is the study of the interaction of highly charged ions with neutral atoms via multi-electron charge exchange. This type of experiments will be covered in the next two chapters, dedicated to the preparation to the ion - atom collision study.

Additionally we performed experiments on charge breeding in an EBIT. This will be the topic of the 7th chapter.

Chapter 3

Theory of Ion - Atom collisions

3.1 Introduction

The HITRAP project will have the interaction of HCI as projectiles with atoms targets as a field of research with special emphasis on multi-electron processes. The project will provide a unique possibility for the investigation of charge exchange between heavy highly charged ions, like U^{92+}, and atoms at low velocities. This possibility has not been available to experimentalists up to now.

The knowledge of reaction cross sections at low velocity is very important, for example, for the physics of ion sources. The charge exchange of HCI with the surrounding neutral atoms influences drastically the charge state distribution of ions produced by the source (see chapter 5).

In the variety of processes in ion - atom collisions one should have a clear conception of the possible reaction channels, see fig. 3.1. The capture from the neutral atom can be from an outer or inner shell of the target. With electron capture onto the projectile into a more deeply bound state energy is released and can be transferred to the target. This may excite remaining electrons to upper levels. The excitation can even finish in the continuum of the target atom, which is the transfer ionization (TI) process. The TI is essentially different from direct ionization which is also a possible process due to the Coulomb force. Autoionization is a post-collisional process, when relaxation of excited projectile or target states results in electron emission (Auger electrons).

In this chapter basic ideas behind the processes and simple models which allow qualitative as well as quantitative predictions, are treated. Often the full quantum mechanical approach of electron charge exchange is extremely complex due to the multi-particle character of the collision process and far beyond the presented models, thus for highly charged ions and multi-electron exchange the models offer a good tool for estimations and explanations of experiments.

In the formulas of this chapter atomic units (a.u.) are used (see Appendix

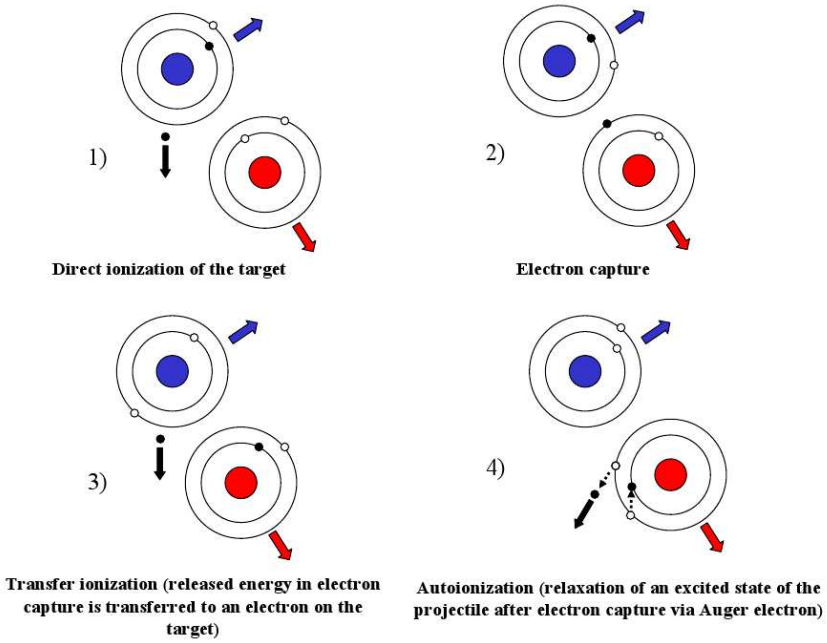

Figure 3.1: Possible processes in ion - atom collisions. The projectile ion is depicted in red, the target atom in blue, black dots represent electrons and empty circles vacancies. Direct ionization (1) is an escape of the electron from the target due to the Coulomb force between the influenced electron and the projectile ion. Electron capture (2) is a charge transfer between the target and the projectile. With electron capture onto the projectile into a more deeply bound state, released energy can be transferred to the target and excite remaining electrons to the continuum, this is the transfer ionization (TI) process (3). Autoionization (4) is a post-collisional process, for example, when one of the two electrons captured onto the projectile relaxes into a more deeply bound state via emission of another electron to the continuum.

A).

3.2 Perturbation theory

For calculations of different cross sections quite often a semiclassical approximation is used assuming a classical trajectory of the projectile ion. To validate this assumption the de Broglie wavelength of the projectile $\lambda \approx \frac{1}{Mv}$ should be less than the typical interaction radius which is around 1 a.u.[1] and thus the assumption is appropriate for energies above 10 eV/u. Another essential con-

[1]To be more precise the interaction radius is close to $Z_B^{\frac{1}{3}}$ corresponding to the maximal electron density of the target (from the Thomas - Fermi model of the atom [Lan89]) where Z_B is the charge of the target nucleus.

dition for treating the ion motion classically is that in quantum the description of the relative projectile-target motion the quantum number of the angular momentum l is very large, i.e. $l >> 1$. The angular momentum $\mu bv = \sqrt{l(l+1)}$, where μ is the reduced mass of the target atom and projectile ion and b the impact parameter. The condition for l is already valid at 10 eV/u as well, if one takes into account that the interaction takes place at impact parameters close to the Bohr radius, $b \approx 1$.

Perturbation theory, i.e. application of the first-order time dependent non-relativistic perturbation, for the semi-classical approximation was developed [Ban85] and successfully used for small q/Z_B^{eff} ratios, where q and Z_B^{eff} are the projectile's ionic charge and the effective target nuclear charge felt by the electron influenced in the collision, respectively. In case of a bare projectile and K-shell capture, Z_A and Z_B should be used, projectile and target nuclear charges. Assuming a classical projectile motion, the probability amplitude for an electron to be captured into the n^{th}-shell (n - the main quantum number) of the projectile ion from, e.g. the K-shell of the target, is given by [Ban85]:

$$a_n(+\infty) = -i \int_{-\infty}^{+\infty} < n|V(t)|K > exp(i\omega_{nK}t)dt, \tag{3.1}$$

here the Coulomb perturbation is

$$V(t) = -\frac{Z_A}{|\mathbf{R}(t) - \mathbf{r}|} = -\frac{Z_A}{2\pi^2} \int \frac{e^{i\mathbf{q}[\mathbf{r}-\mathbf{R}(t)]}}{q^2} d^3q, \tag{3.2}$$

$\mathbf{R}$(t) is the vector from the target nucleus to the projectile, $\mathbf{r}$ is the vector from the target to the influenced electron, ω_{nK} is the energy difference between the final and the initial states, and q is the momentum. The transition amplitude is expressible as

$$a_n(+\infty) = i\frac{Z_A}{2\pi^2} \int < n|e^{i\mathbf{qr}}|K > I(\omega_n K, q)d^3q, \tag{3.3}$$

where $I(\omega_{nK}, q)$ is the orbital Fourier integral

$$I(\omega_{nK}, q) = \int_{-\infty}^{+\infty} e^{i[\omega_{nK}t - \mathbf{qR}(t)]} dt. \tag{3.4}$$

In the case of a straight line trajectory of the ion which is a valid assumption for estimations at high energies, this integral is

$$I_{sl}(\omega_{nK}, q) = 2\pi e^{-iqb} \delta(\omega_{nK} - q_0 v), \tag{3.5}$$

where v is the projectile velocity. The longitudinal momentum transfer q_0 is thus fixed at

$$q_0 = \omega_{nK}/v. \tag{3.6}$$

Substituting 3.5 into 3.3 gives for the amplitude

$$a_n(+\infty) = i\frac{2Z_A}{v} < n|K_0(\xi q_0)e^{iq_0 z}|K >, \tag{3.7}$$

where K_0 is the modified Bessel function and ξ is the distance between the influenced electron and the projectile trajectory along the z axis.

The total capture probability for fixed impact parameter b is the sum over all states:

$$P_K(b) = \sum_n |a_n(+\infty)|^2 \tag{3.8}$$

Taking into account ionization (capture into continuum) one should also integrate in eq. 3.8. Finally, the total cross section is given as:

$$\sigma_K = 2\pi \int P_K(b) b db. \tag{3.9}$$

The capture cross section 3.9, when calculated with hydrogen-like initial and final states using equations 3.8 and 3.7 [Ban85], shows qualitatively similar features with respect to the target ionization, e.g. a rise of the total K-shell capture cross section with increasing projectile velocity v until the velocity is comparable to the electron orbital velocity v_K. Further increase of the kinetic energy of the projectile leads to a decrease of the cross section.

To understand a collision one should always compare the projectile and target electron orbital velocities. When the projectile velocity is larger, then it is a high-velocity collision regime, when v is comparable or less than the target electron velocity, then these are intermediate or low-velocity collision regimes, respectively.

For target ionization, a similar behavior of the cross section was obtained using another perturbative method, the plane-wave Born approximation (PWBA) [Mon82, Lan89, Col68]. This approximation also shows that the cross section of electron capture into the nth - shell of the projectile should follow a n^{-3} dependence at intermediate and high energies [New84].

3.3 Ion - atom interactions at different velocities

The electron capture cross section from the K - shell of the target atom (eq. 3.7) strongly depends on the factor $\frac{Z_A}{v} = \frac{Z_A}{v}\frac{v_K}{Z_B}$. Thus the important parameters in collision are the projectile ion Z_A and the target atom Z_B nuclear charges[1], as well as projectile v and target electron v_K orbital velocities. One can choose

[1]For not bare projectile ion, instead of Z_A, ion charge q and in case of different electron shell ionization (not the target's K-shell) the effective charge seen by the influenced target electron Z_B^{eff} should be used, respectively.

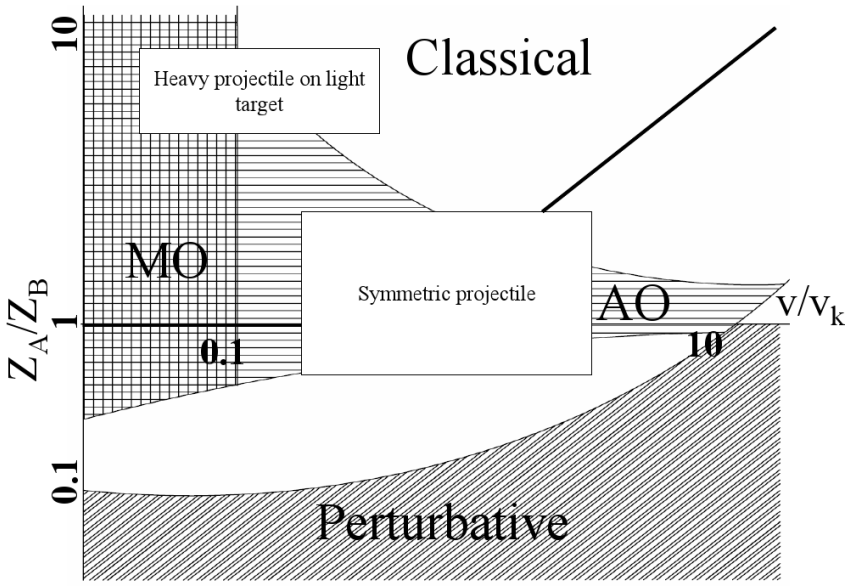

Figure 3.2: The Madison-Merzbacher map for electron capture from the K shell of the target (from ref. [Mad75]). The two axis are ratios of projectile to target charges Z_A/Z_B and projectile to target electron orbital velocities v/v_K. Above the thick solid line electron motion about the projectile can be treated classically, and below perturbative treatments are appropriate. In the central region neither perturbative nor classical models work particularly well and the process is best described in terms of eigenfunction expansion (molecular (MO) or atomic (AO) orbitals).

these values to mark regions of different theoretical approaches. The most common picture is the Madison-Merzbacher map (for the K shell capture) [Mad75], see figure 3.2. The two axis are ratios of projectile to target charge and projectile to target electron orbital velocities. Above the thick, black, solid line electron motion about the projectile can be treated classically, and below perturbative treatments is appropriate. To treat the electron motion classically it is necessary that the Bohr parameter Z_A/v for the electron - ion interaction should be larger than unity [Lan89, Ban85], or in terms of the parameters used for the Madison-Merzbacher map $Z_A/Z_B > v/v_K$. On the other hand, in the classical treatment capture can only happen into a more deeply bound state on the projectile and as we describe the K-electron, this means $Z_A > Z_B$. So the conditions $Z_A/Z_B > v/v_K$ and $Z_A/Z_B > 1$ define the region of classical treatment. In the central region neither perturbative nor classical models work particularly well and the process is best described by the close-coupling methods, in terms of eigenfunction expansion (molecular (MO) or atomic (AO) orbitals).

3.3.1 High velocity

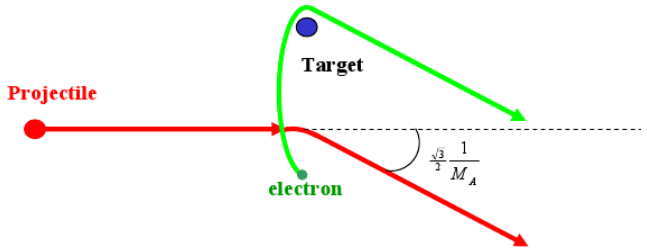

Figure 3.3: Electron capture at high velocities (Thomas mechanism) happens via double scattering of the electron first from the projectile and then from the target nucleus to obtain enough momentum.

For high projectile velocity the electron on the target does not have enough kinetic energy to follow the projectile, thus projectile and electron cannot become bound in a single two-body interaction. Therefore the capture process is essentially three-body in nature. In classical calculations of Thomas [Tho27] the electron gains enough energy due to a double scattering. The electron is scattered at first from the projectile and then from the target as shown in fig. 3.3. In Thomas treatment the target - ion interaction is neglected so only electron - target and electron - projectile interactions are taken into account. This model predicted a so-called 'Thomas peak', when the projectile is scattered only off the electron at an angle $\frac{\sqrt{3}}{2}\frac{m_e}{M_A} = \frac{\sqrt{3}}{2}\frac{1}{M_A}$ [Ban85]. After the first classical treatment, which showed qualitatively the physics of ion - atom collisions, further quantum mechanical calculations were performed using perturbative methods, which were successfully applied in this collision regime [Sha79, Bri80, Spr78] and show a v^{-11} dependence of the capture cross section on the projectile velocity.

3.3.2 Intermediate velocity

For lower projectile velocities the ion - atom interaction cannot be treated by perturbative methods anymore and molecular treatment is preferable. At intermediate velocities the collision is still not slow enough to employ an expansion in a few molecular orbits, and here the best way is to use a linear combination of atomic orbits centered on each of the nuclei [Ban85].

The kinematics of the intermediate velocity collision is not of primary influence anymore on the distortion of the electron orbit which is necessary for the transfer from one nucleus to the other. Most important is the temporal change of the Coulomb field created by both nuclei and the time provided by the collision velocity for this change to take place. Based on that, Bohr and Lindhard (BL) developed a simple model which is represented here from [Ban85, Knu81]. For the electron to be captured from the n^{th} target shell,

the attractive Coulomb force from the projectile ion at the closest approach should be larger than the binding force from the target. The force equilibrium condition gives a distance at which the capture happens, using the Bohr model:

$$\frac{v_n^2}{a_n} = \frac{q}{R_{rel}^2}, \tag{3.10}$$

here R_{rel} is the internuclear distance itself at which the electron is released, $v_n = Z_B/n$ and $a_n = n^2/Z_B$ are Bohr velocity and orbit, respectively[1]. Equation 3.10 gives $R_{rel} = \sqrt{qa_n/v_n^2}$ from which the geometric cross section can be found:

$$\sigma = \pi q \frac{a_n}{v_n^2}. \tag{3.11}$$

This capture cross section is independent of the collision velocity. On the other hand, it is considered in the model that capture can happen only, if in the projectile frame the electron potential energy is larger than its kinetic energy

$$\frac{q}{R_{cap}} > \frac{1}{2}v^2. \tag{3.12}$$

So the electron will be captured at distances less than R_{cap}, derived as:

$$R_{cap} = 2\frac{q}{v^2} \tag{3.13}$$

At small velocities, R_{rel} determines the cross section. As the velocity of the collision increases, R_{cap} becomes smaller than R_{rel} and now determines the geometric cross section weighted by the probability that the collision duration is long enough to take place. This probability in the model is the ratio $\frac{R_{cap}}{v}\frac{v_n}{a_n}$, i.e. collision time to electron orbital time. Finally the cross section is:

$$\sigma = \pi R_{cap}^2 \frac{R_{cap}}{v}\frac{v_n}{a_n} = 8\pi \frac{v_n}{a_n}\frac{q^3}{v^7}. \tag{3.14}$$

Change from R_{rel} to R_{cap} shows a sudden decrease of the cross section as a function of projectile energy which was independent of the energy. The model proved to be good for a description in the low and intermediate velocity regions. On fig. 3.4 one can see cross sections calculated using the BL model for collisions of different ions on hydrogen in depedence on the projectile kinetic energy from [Knu81]. A good correspondence between different experiments and the described model was found.

For ionization cross sections in the intermediate velocity collision regime one can use Rutherford's formula:

$$d\sigma = 2\pi \frac{q^2}{\mu v^2}\frac{d\epsilon}{\epsilon^2}, \tag{3.15}$$

[1]One can use $n = 1$ and instead of the target nuclear charge Z_B - effective charge Z_B^{eff} felt by the influenced electron.

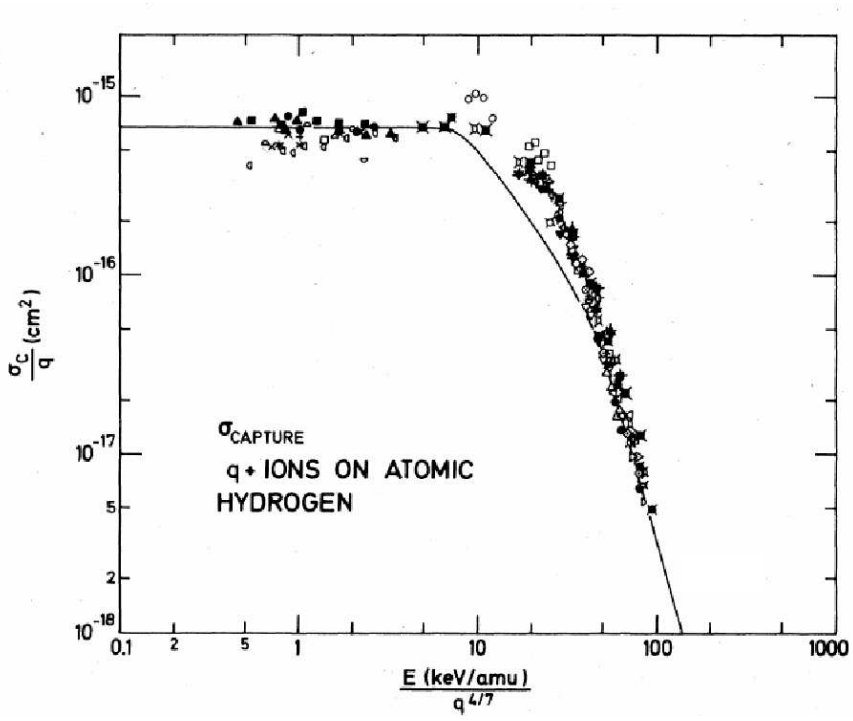

Figure 3.4: The capture cross sections for various ions colliding with atomic hydrogen in comparison with the BL model calculations (solid line), from ref. [Knu81]. Here $amu \equiv u$.

which describes the cross section as a function of energy loss ϵ of the projectile scattered on the target, μ is the reduced mass of the colliding particles and ϵ can take values from zero up to $\epsilon_{max} = 2\mu^2 v/m_t$, with the m_t mass of the target. Choosing a bound electron as a target ($m_t = 1$) with the assumption that neither the electron nor the projectile interact with the target nucleus, i.e. in a free electron approximation, one can get ionization cross sections by integrating equation 3.15 from the ionization energy I necessary to release the influenced electron up to the maximum energy loss. The result is as follows:

$$\sigma = 4\pi \frac{q^2}{v^2}\left(\frac{1}{2I} - \frac{1}{4v^2}\right). \tag{3.16}$$

This cross section has a maximum at $v = \sqrt{I}$. On fig. 3.5 one can see ionization cross sections for different projectile charge states colliding on Mg-target for the proposed experiment at HITRAP.

3.3.3 Low velocity

In case of low projectile velocity one can already apply the Bohr - Lindhard model to get the capture cross section or use similar but not identical classical

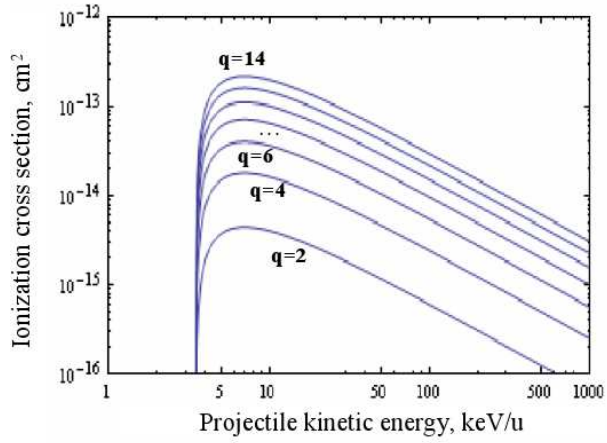

Figure 3.5: Cross sections for outer shell single-electron ionization in collisions of projectiles of charges 2+ to 14+ with Mg atoms in dependence on the projectile energy. The cross sections were calculated using Rutherford's formula 3.16.

over barrier model which is the topic of the next subsection. For the low velocity regime an expansion in a few molecular orbits can be employed. In the simplest case a two level system can be used, i.e. electron on the target and electron on the projectile. In the collision the ion - atom interaction force at a large distance between the target and the projectile is slightly attractive due to the polarization of the target. As the projectile approaches closer, the repulsion between the nuclei starts when the overlap of electron clouds occurs. For ion - ion interaction the repulsive force acts at all distances between the interacting heavy particles. One can see the potential curves of the ion - ion and ion - atom interactions in fig. 3.6.

They have a cross-over point at R_C which is the distance where the electron capture takes place. As the wave function of the system in the vicinity of the cross-over point can be taken as a superposition of two molecular states (electron on the target and on the projectile) [Lan89], the energetic terms are expressed as: $U_{1,2} = (H_{11} + H_{22})/2 \pm 1/2\sqrt{(H_{11} - H_{22})^2 + \Delta^2}$ where $\Delta = 2H_{12} = 2V_{12}$, $H_{11,22} =< \Psi_1|H_0 + V|\Psi_2 >$. Here H_{ij} are Hamiltonian matrix elements, V and H_0 are the perturbation, which causes the transition and the "non-perturbed" part of the Hamiltonian, respectively.

In the Landau - Zener (LZ) model of electron capture, which deals with a potential curve crossing in ion - atom interaction, two parameters are used: 1. $H_{11} - H_{22} = \lambda(R - R_C)$, where R is the internuclear distance, and 2. $\Delta = const.$ According to the model [Lan89, Kno06] an electron transition from one state

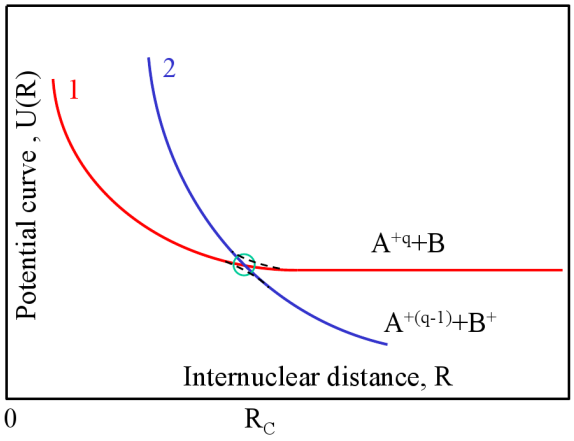

Figure 3.6: Schematic diagram of the potential curves for the electron capture reaction $A^{q+} + B \rightarrow A^{(q-1)+} + B^{+}$

to another, which happens at the distance of cross-over[1], is defined as:

$$P(b) = exp[-\pi \frac{(\Delta)^2}{2v_R(b)(F_2 - F_1)}], \tag{3.17}$$

where $F_2 - F_1$ is the difference in slopes of two potential curves, i.e. $\frac{d}{dR}(U_1 - U_2)|_{R=R_C}$, $v_{R_C}(b)$ is the relative (radial) ion - atom velocity which depends on the impact parameter b. At the distance R_C: $v_{R_C} = v_0((1 - U_1(R_C)/E)(1 - b^2/R_C^2))^{1/2}$, where v_0 and E are projectile initial velocity and kinetic energy, respectively. Assuming a pure Coulomb curve for the outgoing channel and a constant curve for the incoming channel (fig. 3.6) one can approximate $F_2 - F_1 \approx \frac{q-1}{R_C^2}$, with q the projectile charge. The coupling element H_{12} calculated for ion - hydrogen collision experiments [Ols76] was found to be:

$$H_{12} = 9.13/\sqrt{q} exp[-1.324 \alpha R_C/\sqrt{q}], \tag{3.18}$$

where $\alpha = \sqrt{2I_1}$ is an introduced parameter to extend the H_{12} value to any target different from hydrogen, with I_1 the first ionization potential of the target. Since the projectile ion passes the cross-over point twice in the collision, the total probability of electron capture (p) is a sum of $1 \rightarrow 2 \rightarrow 2$ and $1 \rightarrow 1 \rightarrow 2$ scenarios (1, 2 depict the electron levels and arrows transitions between them), thus: $p = 2P(P-1)$. The cross section can be calculated using formulas 3.9 and 3.17. For highly charged projectiles of course the capture is essentially a multi-channel process, so the number of curve crossings is higher and more scenarios should be included [Sal76]. In equation 3.17 probability

[1]To be correct cross-over is a pseudo-cross-over due to the splitting of the levels.

should be then denoted by indices n and l and the Taulbjerg factor [Tau86]

$$f_{nl} = \frac{(-1)^{n+l-1}(2l+1)^{1/2}\Gamma(n)}{(\Gamma(n+l+1)\Gamma(n-l))^{1/2}} \tag{3.19}$$

is included in the coupling matrix element 3.18, where n and l are quantum numbers of the state into which the electron is captured.

For some special potential curves beside the LZ model two other models were developed [Kar06], the Demkov and Nikitin models. The first one in comparison to LZ is essentially a three - parameter model with $H_{11} - H_{22} = const$ and $\Delta = Be^{-\lambda R}$. The Demkov model was developed [Ols72] primarily for collisions of singly charged ions with atoms and found good agreement with experimental data on alkali-ion - alkali-atom collision systems [Per71]. In the Demkov model the electron is captured not at the cross-over point (which does not happen at all), but at the distance where the coupling matrix element, responsible for the transition, is comparable with the spacing between the energy. The Nikitin model is a combination of Landa-Zener and Demkov models with parameters for the potential curves $H_{11} - H_{22} = \epsilon - Bcos\Theta e^{-\lambda R}$ and $\Delta = Bsin\Theta e^{-\lambda R}$, an example of application of this model is described in [Nik89].

3.4 Classical over-barrier model

The classical over-barrier-model (CBM) is not a real classical treatment of the collision, which deals with classical Hamiltonian of the system, but is a description of the ion - atom interaction using simple ideas. It is a model which can predict cross sections for single as well as for multiple electron capture. Since multi-electron treatment of the collision is a real challenge for theoretical calculations, especially for highly charged ions, this self-consistent model (without parameters to enter from experiment) is a valuable tool to understand the qualitative as well as quantitative physical picture of the collision. As the capture cross sections appeared to be independent of the projectile energy in the low-velocity collision regime (see fig. 3.4), this can approve application of static models like CBM. Here it is presented shortly in the form given in [Nie86]. For a detailed description I refer to [Kno06, Bla07].

While even the capture of a single electron by the projectile can happen from different electron levels of the target, an array j of 0 and 1 is introduced distinguishing a scenario of electron capture with "0" showing that the electron is remained on the target and "1" that it is captured by the projectile. For example, j={0,1,1,0,0,0} means that the first (the most loosely bound) electron is left on the target and the next two electrons are captured in the collision with the projectile of charge 6+.

With projectile ion approaching, which is assumed in the model to have a straight line trajectory, electrons of the target start one by one to move into

the potential well created by both nuclei. The motion around both nuclei for the i^{th} electron of the target happens at distance R_i, when the initial electron level I_i, Stark-shifted in the Coulomb potential of the ion, is above the top of the potential barrier separating the target electron from the projectile. As the distance between the nuclei decreases, the next distance R_{i+1} is reached and so on. On the "way out" the projectile passes the same points in reverse order. The geometrical capture cross section of the i - th electron is then determined through the ring shaped area: $\pi(R_i^2 - R_{i+1}^2)$ weighted with a probability factor W taken as a ratio of degeneracy of quantum state on the projectile, into which the capture happens, to the total number of available states (degeneracies of the states on the projectile and on the target). Degeneracy is assumed to be proportional to the square of the main quantum number, in hydrogenic approximation. To get the final cross section for the j - th scenario one combines all the geometrical cross sections with weighting factors of capture W and recapture $1 - W$ back to the target. The final Stark-shifted electron energy on the "way out" is different from the Stark-shifted levels on the "way in" due to the charge redistribution in the ion - atom system. The difference between the initial electron binding energies on the target and the final energies on the projectile and target gives the Q - value of the process (see next chapter).

Also the model introduces possible Q - values in the collision, dependent on the velocity regime, a so-called reaction window. It is based on the uncertainty principle and shows the energy range of projectile states into which the capture is possible (see for example fig. 3.7). Of course the reaction window has a physical meaning only if there are real available electron levels.

string j	Q-value [eV]	σ [cm^2]
single capture		
{1,0,0,0...0}	6.32	$1.26 \cdot 10^{-13}$
{0,1,0,0...0}	35.97	$7.86 \cdot 10^{-17}$
{0,0,1,0...0}	44.17	$6.92 \cdot 10^{-18}$
double capture		
{1,1,0,0...0}	40.34	$9.54 \cdot 10^{-16}$
{1,0,1,0...0}	48.54	$8.40 \cdot 10^{-17}$
{0,1,1,0...0}	69.36	$9.25 \cdot 10^{-17}$

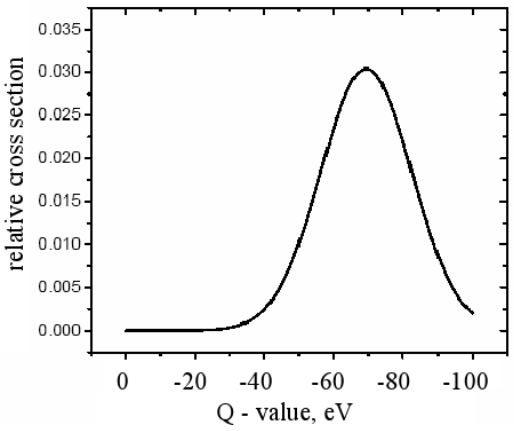

Figure 3.7: Calculated cross sections for $A^{10+} + Na \rightarrow A^{(10-i)+} + Na^{i+}$ reactions using the CBM model and a reaction window for j={0,1,1,0..0} scenario.

For the case of single-electron capture one can use a simple formula from the model to determine the one-electron capture cross section:

$$\sigma_{q,q-1} = \pi(\frac{2\sqrt{q}+1}{I_1})^2, \tag{3.20}$$

where I_1 is the initial binding energy of the uppermost electron on the target. This simple formula can be applied, for example, to estimate the vacuum pressure necessary to have small losses of the highly charged ion beam in the low energy part of the HITRAP facility [Hei06]. Applying the full power of the method one can calculate cross sections for different scenarios. On fig. 3.7 the capture cross sections are given for interaction of highly charged ions with the alkali atom .

Table 3.1: Calculated cross sections for $A^{12+} + Mg \rightarrow A^{(12-i)+} + Mg^{i+}$ (left part of the table) and $A^{12+} + Rb \rightarrow A^{(12-i)+} + Rb^{i+}$ (right part of the table) reactions using CBM model for different scenarios j.

string j	Q-value [eV]	$\sigma[cm^2]$	string j	Q-value [eV]	$\sigma[cm^2]$
single electron capture					
{1,0,0,0,0...0}	10.60	$3.1 \cdot 10^{-14}$	{1,0,0,0,0...0}	5.79	$2.2 \cdot 10^{-13}$
{0,1,0,0,0...0}	14.86	$2.0 \cdot 10^{-15}$	{0,1,0,0,0...0}	24.29	$1.5 \cdot 10^{-16}$
{0,0,1,0,0...0}	52.40	$3.3 \cdot 10^{-18}$	{0,0,1,0,0...0}	28.56	$1.2 \cdot 10^{-17}$
{0,0,0,1,0...0}	61.59	$3.3 \cdot 10^{-19}$	{0,0,0,1,0...0}	32.43	$1.5 \cdot 10^{-18}$
double electron capture					
{1,1,0,0,0...0}	22.58	$3.4 \cdot 10^{-14}$	{1,1,0,0,0...0}	28.51	$2.5 \cdot 10^{-15}$
{1,0,1,0,0...0}	60.14	$5.5 \cdot 10^{-17}$	{1,0,1,0,0...0}	32.77	$2.0 \cdot 10^{-16}$
{1,0,0,1,0...0}	69.31	$5.7 \cdot 10^{-18}$	{1,0,0,1,0...0}	36.64	$2.6 \cdot 10^{-17}$
{0,1,1,0,0...0}	63.35	$6.1 \cdot 10^{-17}$	{0,1,1,0,0...0}	46.61	$2.2 \cdot 10^{-16}$
triple electron capture					
{1,1,1,0,0...0}	68.96	$4.5 \cdot 10^{-16}$	{1,1,1,0,0...0}	49.67	$1.6 \cdot 10^{-15}$
{1,1,0,1,0...0}	78.13	$4.7 \cdot 10^{-17}$	{1,1,0,1,0...0}	53.54	$2.1 \cdot 10^{-16}$
{1,0,1,1,0...0}	106.05	$4.9 \cdot 10^{-17}$	{1,0,1,1,0...0}	56.75	$2.3 \cdot 10^{-16}$
{0,1,1,1,0...0}	108.36	$5.3 \cdot 10^{-17}$	{0,1,1,1,0...0}	66.68	$2.4 \cdot 10^{-16}$

One can see a common behavior of the capture cross section in this case, i.e. a steep decrease going from the first to the second electron capture scenarios, also a big difference between single and multiple electron capture cross sections. All these dependences are easily explained with a big difference in ionization energies of the first and the second electron and thus much smaller distance of the projectile - target approach necessary for the second electron to be captured. For the future experiments there are also some results included for Rb and Mg targets, tab. 3.1. The modern techniques are able to distinguish different scenarios of the interaction and thus get not only total single, double etc. capture cross sections through the charge analyses, but the differential contributions as well. One should mention that in comparison to an alkali atom, which has a single valance electron, the Mg target, which belongs to the 2^{nd} group of the periodic table, has two valence electrons and according to the

model the double-electron capture has even higher probability than the single one. Going further from the 2^{nd} group of the periodic table will show that the double, triple... (according to the group of the target) outer - shell electron capture cross sections are at least of the same order as single-electron capture. Thus the model approves that the HCI - atom interaction has multiple electron charge exchange as dominant processes.

3.5 Statistical interpretation of transfer ionization

As it was mentioned for the interaction of Mg with highly charged ions, the double-electron capture cross section is nearly the same as the single one. But as the valence electrons capture will be into high-n Rydberg states of the projectile ion (according to the CBM model), it is most probable that one of the electrons will be emitted leading to the relaxation of another, a so-called autoionization which is a post-collisional process.

If the collision is slow enough a capture into the ground projectile ion state can happen leading to the release of energy sufficient for additional ionization of the target, a so-called transfer ionization. In this section a statistical interpretation of the TI named "statistical model" is shortly described. It was developed in the 1950ties to calculate multiple-ionization probabilities for target ions produced in slow single- or multi-electron capture [Rus58, Rus63]. The short description will mostly follow the model representation given in [Mue83]. This model in principle is also suitable for future HITRAP collision experiments and can give a qualitative picture of charge exchange.

In the collision process $A^{q+} + B \rightarrow A^{(q-k)+} + B^{i+} + (i-k)e$, $(i-k)$ free electrons escape from the target due to the energy release, which happens with capture of k electrons. This energy release can have a maximum value of

$$\Delta E = \sum_{j=q-k}^{q-1} I_A^{j+} - \sum_{j=0}^{k-1} I_B^{j+}, \tag{3.21}$$

where I_A^{j+} and I_B^{j+} are ionization energies of the projectile and target ions respectively. The energy release is assumed in the model to be distributed in infinitely small units among the remaining $N-k$ outer shell electrons of the target (where N is the number of the outer shell electrons). The $n = i-k$ electrons are "evaporated" from the target if each of them obtains more energy than the average ionization value $< I_B >$.

$$< I_B >= \frac{1}{n} \sum_{j=0}^{n-1} I_B^{(j+k)+} \tag{3.22}$$

This step function is approximated by a smooth curve to "obtain a physically more meaningful shape and allow further computation" [Mue83]. The proba-

bility that n electrons gain enough energy to overcome the $< I_B >$ and leave the target, is given by:

$$P_n(N, \Delta E) = \binom{N}{n} \sum_{j=0}^{l} (-1)^j \binom{N-n}{j} (1 - \frac{n+j}{\Delta E / < I_B >})^{N-1} \tag{3.23}$$

with $l = Int[\Delta E / < I_B > -n]$, where Int indicates the integer part of the value inside the square brackets, $\binom{i}{j}$ is the binomial coefficient. Via equation 3.23 one can get different fractions of target ion charge states. On fig. 3.8 there are calculated target charge state distributions (from eq. 3.23) for $Ar^{q+} + Rb \rightarrow Ar^{(q-1)+} + Rb^{(1+n)+} + ne$ collisions as an example, for the proposed experiment at HITRAP. The vertical lines indicate the positions of the maximal released energies for different projectile (Ar) charge states from formula 3.21. Crossings of the calculated curves with vertical lines predict the fractions of (1+n)+ target ions in the experiment. As it is seen all dependences have thresholds. While the energy release is below the ionization energy of the second target electron, only capture without TI exists. As the released energy reaches the ionization energy it becomes more and more probable that the second electron will be "evaporated" as well, then with reaching the ionization energy of the third electron another channel for energy release is opened and so on. The recent experiments on multiple electron charge exchange [Ma99, Cai03] were qualitatively well described by the statistical model, but with a deviation in absolute values, probably because the capture into the ground state of the projectile is not the best assumption. To include capture with "real" energy release one can use a combination of the classical-over-barrier and the statistical models with the Q-value (ΔE) taken from the CBM.

In conclusion to this chapter I would like to remind that though the CBM and statistical models are definitely not the best for various cross section calculations, they are still useful tools for different estimations in slow HCI - atom collisions. For very high charge states of the projectile and high nuclear charge of the target these models are quite reasonable and representative.

Of course, one should mention classical trajectory Monte Carlo [Ols77, Sal77, Hor94] and basis generator [Kno06, Lue96, Kro99] methods, nicely described in the referenced papers. These methodes are also extensively used for single and multiple electron charge exchange.

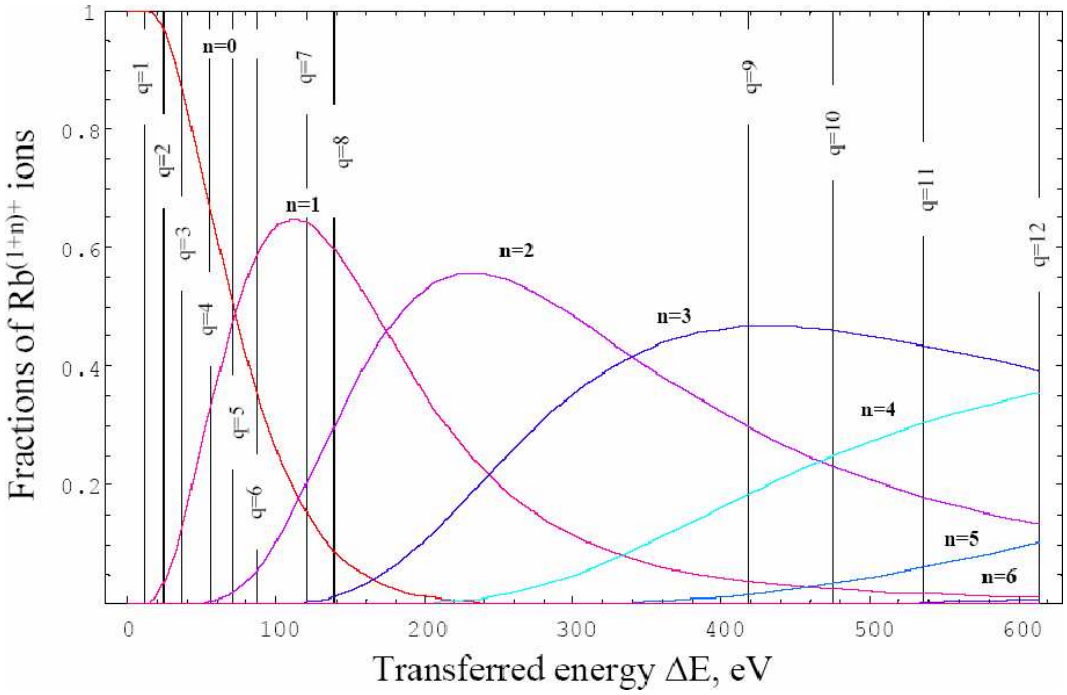

Figure 3.8: Calculated, using the statistical model, fractions of Rb ions in $Ar^{q+} + Rb \rightarrow Ar^{(q-1)+} + Rb^{(1+n)+} + ne$ collisions in dependence on the energy transferred via electron capture. Crossings with a vertical line predict the fractions for experiment, when the Rb valence electron capture happens into the ground state of the projectile ion of charge state q.

Chapter 4

Ion - Atom collision experiment

4.1 Ion - atom collision kinematics

In this chapter a description of ion - atom interaction experiments is given with special emphasis on a magneto-optical trap (MOT) setup with its possibilities and advantages. To investigate ion - atom collisions one should start with the energy and momentum conservation principles to describe the kinematics of the reaction products (in this chapter atomic units are used). The charge exchange reaction is $A^{q+}+B \rightarrow A^{(q-s)+}+B^{(r+s)+}+re$, where s is the number of electrons captured by the projectile and r is the number of electrons emitted from the target into the continuum. In the MOT experiments the target atoms are cooled to extremely low temperatures in the μK range and for some setups even in the nK range. In comparison with the room temperature atoms (not talking about the projectile ions) the target atoms are assumed to be initially at rest[1], thus the projectile momentum is the initial momentum of the total system and its change is distributed between the collision products. The conservation principle for the longitudinal momentum is written as:

$$P_{proj}^{i\parallel} = P_{proj}^{f\parallel} + P_{rec}^{\parallel} + \sum_{l=0}^{r} P_{e,l}^{\parallel} \tag{4.1}$$

with $P_{proj}, P_{rec}, P_{e,l}$ projectile, recoil ion (target) and electron momenta, respectively, indices i and f denote initial and final value (before and after the collision). Energy conservation in the non-relativistic regime of collision leads to the equation:

$$\frac{m_{proj}v_{proj}^{i2}}{2} - \frac{m_{proj}v_{proj}^{f2}}{2} - \frac{sm_e v_{proj}^{f2}}{2} = B_{target}^{r+s} - B_{proj}^{s} + \sum_{l=0}^{r} E_{e,l} \tag{4.2}$$

where m_{proj} is the mass of the projectile ion A^{q+}, v_{proj} is the projectile velocity, $E_{e,l}$ are electron kinetic energies, B_{target}^{r+s} and B_{proj}^{s} are the total binding energy

[1]For other experiments (like with a gas jet) at least two velocity components of the target atom are assumed to be negligibly small.

of $s + r$ electrons removed from the target and the binding energy of s electrons captured in the collision onto the projectile, respectively. Here these are absolute values, so for more deeply bound electrons the corresponding binding energies B are bigger. It is necessary to mention that the only assumption which was made to get eq. 4.2 is the smallness of projectile velocity change (in other words small scattering angle of the projectile). Also it should be mentioned that the binding energy B^s_{proj} is in general not the ground state energy but the one right after the collision, thus it can relax into the ground state of the projectile through photon or electron emission. The change of the projectile kinetic energy and momentum is:

$$\Delta E_{proj} = \frac{\Delta m_{proj} v^{i2}_{proj}}{2} + m_{proj} v^{i}_{proj} \Delta v_{proj} \tag{4.3}$$

$$\Delta P_{proj} = m_{proj} \Delta v_{proj} + \Delta m_{proj} v^{i}_{proj} \tag{4.4}$$

here the electron mass is assumed to be much smaller than the atom mass ($m_e << m_{proj}$) and the change of the projectile velocity is small, i.e. $\Delta v_{proj} << v_{proj}$. The change of the projectile mass is due to the s captured electrons and thus $\Delta m = m_e s$. From equations 4.2 and 4.3 one gets the Q-value of the reaction[1]

$$-\Delta E_{proj} = B^{r+s}_{target} - B^{s}_{proj} + \sum_{l=0}^{r} E_{e,l} = Q, \tag{4.5}$$

which is directly linked to the deceleration or acceleration of the projectile ion. For the recoil target ion one can get the recoil momentum from equations (4.1, 4.2, 4.3, 4.4), which is:

$$P^{\parallel}_{rec} = \frac{B^{r+s}_{target} - B^{s}_{proj}}{v_{proj}} - \frac{s m_e v_{proj}}{2} + \sum_{l=1}^{r} \left(\frac{E_{e,l}}{v_{proj}} - P^{\parallel}_{e,l} \right). \tag{4.6}$$

As mentioned, only longitudinal projections of the momenta are described in the above equations. For the transverse momentum one should use a conservation principle in the form $P^{f\perp}_{proj} + P^{\perp}_{rec} + \sum_{l=0}^{r} P^{\perp}_{e,l} = 0$. The transverse momentum for fixed impact parameter can be estimated for example from the classical-over-barrier model (CBM) by integrating the Coulomb repulsion force in the form $(q \cdot i)/R^2$ over time, here q and i are the charge states of the projectile and the target, respectively. The integration is performed over the projectile path under the assumption of constant projectile velocity and linear trajectory. The path is divided into several intervals each $[R_i\sqrt{1-(b/R_i)^2} - R_{i+1}\sqrt{1-(b/R_{i+1})^2}]$ units long and correspondent to the R_i (see chapter 3), which is the position of the projectile during the i^{th} electron capture. Along each of these intervals, the target's charge is equal to the index i from the model (i electrons are shared between the target and the

[1] In literature the Q-value is usually given as $Q = B^{r+s}_{target} - B^{s}_{proj}$.

projectile). For details I refer to ref. [Bla07] where calculations of transverse momentum distribution were done for collisions of Ar^{12+} and U^{90+} ions with rubidium atoms proposed for future HITRAP experiments. Coming back to the equations above one should mention that for pure electron capture with no electrons emitted into the continuum, the Q-value is simply the sum of the total binding energies and equation 4.6 transforms into:

$$P_{rec}^{\parallel} = \frac{Q}{v_{proj}} - \frac{sm_e v_{proj}}{2} = -\Delta P_{proj}^{\parallel}. \tag{4.7}$$

Thus the longitudinal momentum of the recoil ion as well as the change of the projectile momentum depend only on the Q-value, the projectile velocity and the number of transferred electrons. This is the case in the small velocity collision regime, when the capture dominates the direct ionization .

4.2 Experimental methods

One can find out different methods suitable for electron capture investigation considering equation 4.7. For a full picture of the collision one can study the momentum and charge state of the recoil ion, the energy gain and charge state of the projectile or X-rays and photons emission to gain information on the energy states of the electrons captured on the projectile.

The charge transfer during the HCI - atom interaction in general takes place into an excited state of the projectile. Thus during or after the collision[1] photons and X-rays are emitted indicating that the electrons were captured into particular projectile state. Relaxation of the excited state via radiation can be a step-like proccess with the total difference between the excited and ground state equal to the sum of the emitted photon energies. Obtaining all the spectral lines in the collision is an issue for photon emission spectroscopy (PES). Unfortunately, the total emission spectrum is not usually enough to get the Q-value of the collision, because of the often Auger electrons emitted in TI or autoionization processes. A big advantage of the PES is that it can be used in coincidence technique parallel to other methods. This will give differential cross sections for some special cases of electron capture and for example can distinguish different j scenarios for classical-over-barrier model.

Another method of investigation is translation energy spectroscopy (TES) which investigates the kinetic energy distribution of the projectile in a selected charge state after the collision. As shown above the projectile kinetic energy changes with electron capture. Kinetic energy can be gained if the capture

[1] Normally the collision time (of the ions, for example, from an ion source) is of the order of a fs, this means that it can be less or more than the excited state relaxation time which can be from several ns to a few as dependent on the charge state of the HCI colliding on the target. For the recombination one can get the relaxation time from uncertainty principle $\tau = 1/\Gamma$, where τ is a lifetime and Γ is an electron level width, which increases with increase of the projectile charge state [Kos71].

happens into an electronic state of the projectile more deeply bound than the initial state on the target or when the capture is into a slightly less bound state with the condition $Q < \frac{sv_{proj}^2}{2}$, other cases lead to kinetic energy loss. Experimentally projectile gain spectra can be obtained with electrostatic deflectors, like spherical spectrometer [Lak92] built by the author. As the electrostatic rigidity is proportional to the kinetic energy of the ion, a potential on the deflector will cause energy dependent angles of deflection. The same influence on the ion trajectories is from the dipole magnet because magnetic regidity is proportional to the momentum of the ion. Thus using position sensitive detector or changing the magnetic field of the dipole or the potential on the deflector can provide energy gain spectra. Additional possibility is to use TOF technique.

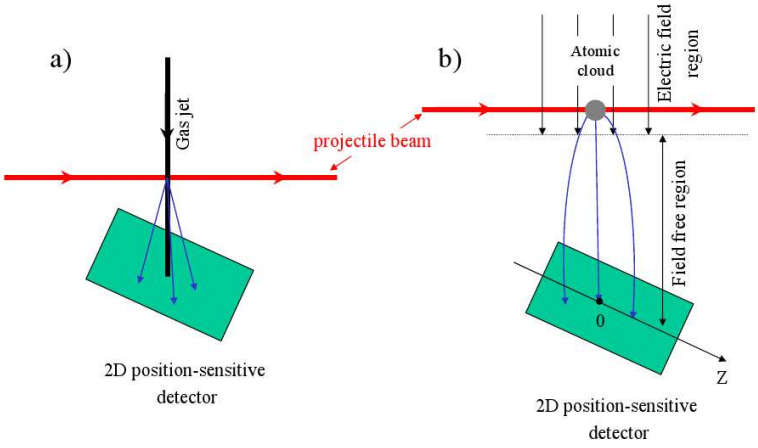

Figure 4.1: Geometries for recoil ion momentum investigation using (a) gas jet and (b) MOT cloud.

The recoil ion momentum study is an issue for the recoil - ion momentum spectroscopy (RIMS)(see for example [Ull97]). It is a novel technique which allows to get target ion momentum distribution with high resolution. For this purpose the position of the target should be initially known and small kinetic energy (temperature before the collision) should be achieved. As an example a gas jet (see e.g. [Sch97]) can be used (fig. 4.1,a). From a reservoir a relatively pressurized gas flows through a small nozzle into high vacuum chamber, the gas jet which is formed has a small diameter and small transversal temperature (around 0.1 mK). The flow moves towards a position sensitive ion detector. Crossing the projectile ion beam the electron charge exchange happens and

recoil ions produce a 2D pattern on the detector. Another possibility is to use magneto - optical trap (MOT) (see next section) to get small cold atomic cloud. The basic idea in this case (fig. 4.1,b) is to apply an external force that extracts the recoil ions perpendicular to the projectile beam direction towards the 2D position sensitive detector. Knowing precisely the initial (zero) position of the target atom in the detector's plane one can get the momentum transferred to the target ion. The recoil ion will hit the detector at a distance Z (along the beam axis)$= \frac{\Delta P_{rect}^{\parallel} t}{M_{rec}}$, where t is the time of flight towards the detector dependent on the extraction force. As an extraction force usually a homogeneous electric field is applied to exclude non-linearities.

One of such RIMS with resistive electrodes from Heidelberg is shown on fig. 4.2, left for which a simulation using SIMION 7.0 was done in order to estimate the resolution. The studied RIMS will be suitable for future collision experiments of HCI with neutral Rb atoms in the MOT proposed for the HI-TRAP project. On fig. 4.2, right one can see the trajectories of Rb^{2+} ions with the maximum transverse momentum transferred to the recoils by 10 keV/u projectiles in the collision $Ar^{12+} + Rb \rightarrow Ar^{10+} + Rb^{2+}$. All ions with up to the maximum 60 a.u. of momentum, calculated in [Bla07], will hit the 2D detector when 300 V bias voltage is applied to the electrodes. The extraction voltage can be increased up to 1 kV to increase the acceptance of the RIMS for heavier highly charged projectiles which transfer higher momentum.

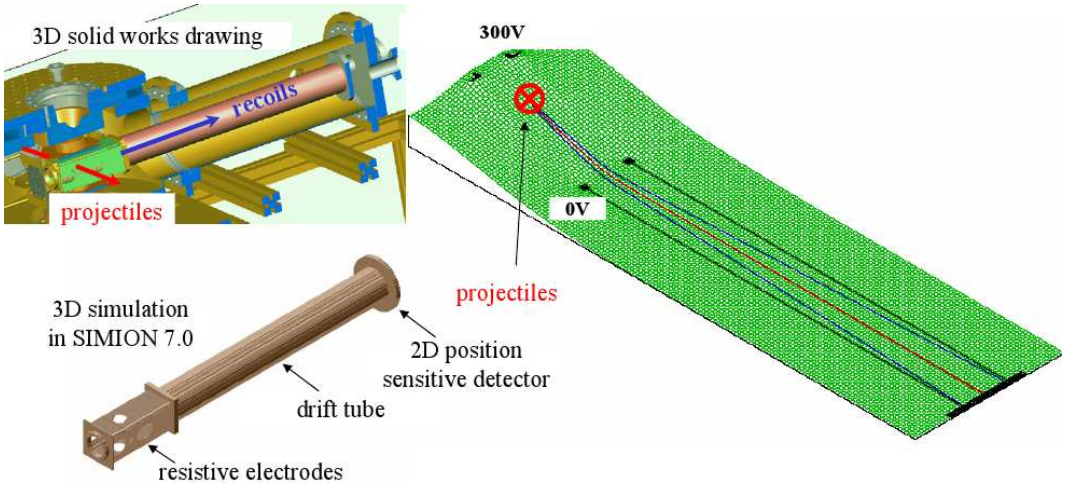

Figure 4.2: Heidelberg RIMS and it's simulation using SIMION 7.0, left. The trajectories of Rb^{2+} ions on the potential surface with 60 a.u. maximum transferred transverse momentum (blue lines) in the collision $Ar^{12+} + Rb \rightarrow Ar^{10+} + Rb^{2+}$ when the projectile ion has 10 keV/u kinetic energy, right.

Of course more information on the reaction products after the collision will cover better different charge exchange processes. Modern devices can include projectile analyzer in combination with a special recoil ion momentum

spectrometer (called "reaction microscope") [Ull97]. In this spectrometer extracting electric field acts not only on the recoils but also on the electrons emitted in the collision which are extracted in the opposite (to the ions) direction towards another position sensitive detector. Reaction microscope can be also equipped with a photon or an X-ray detector(s) expanding further investigation possibilities [GSI-webpage, deJ04].

4.3 MOTRIMS setup at KVI

As it was mentioned the HITRAP ion - atom collision experiments will deal with heavy highly charged projectiles and Rb - MOT target or a gas jet target, thus meaning mostly a multiple electron charge exchange investigations. The experiment with Ar^{12+} from the off-line ion source as a projectile colliding on a Mg jet target will be concentrated mainly on a double electron charge exchange. Single electron capture and ionization were performed already by us at KVI with light ${}^3He^{2+}$ projectile ions (alpha-particles) from an ECR ion source interacting with a sodium atomic cloud in the MOT. The recoil ions were analyzed with a RIM spectrometer. This combination of the MOT - target and RIMS is known as the MOTRIMS - technique. The main purpose of the study was to obtain ionization cross sections in dependence on the projectile ion velocity and to get acquainted with MOTRIMS setup possibilities for upcoming experiments at HITRAP. In this section a short description of the KVI setup is made, for detailed overview see [Kno06, Has06].

The ions produced in the ECR ion source (see chapter 5) were separated after extraction via a 110° bending magnet and delivered towards the MOT through a beam line consisting of several quadrupole triplets. Right before the reaction chamber the ions passed through four diaphragms to form parallel and well-defined continuous beam. After the reaction chamber the projectile ions were collected on a FC to check the stability of the beam from the source ($\approx$ 10 nA ion beam). As it was mentioned the ions used for experiment were isotopes of helium (${}^3He$) initially injected into the ionization chamber of the ion source as a gas from a bottle. The potential of the ionization chamber could be set up to 26 kV (though we went only up to 21 kV because of the sparks in the source). As a target neutral sodium atoms were used, produced via evaporation from the oven. To get more atoms into the MOT a laser beam, red-detuned from the resonance transition frequency (see below) was directed towards the oven. Due to the Doppler shift hotter atoms had transition frequencies closer to the laser frequency and thus absorbed the light more rapidly and thus bigger momentum [1]. Decelerated in such a way atoms were easier to catch in the

[1] The light absorbed by the atom kicks it backwards. Afterwards the excitation is relaxed via re-emission of the photon in a random direction thus after many cycles of absorption - de-excitation the average momentum transferred to the atom is only in the light propagation direction.

MOT.

4.3.1 MOT

The first principles of magneto - optical trapping appeared in the early 70th and offered a unique possibility to produce very cold neutral atomic cloud [Phi98, Dal75]. The resulting progress of further development was a creation of the Bose - Einstein condensate (in 1995, by Eric Cornell and Carl Wieman at the University of Colorado at Boulder NIST-JILA lab).

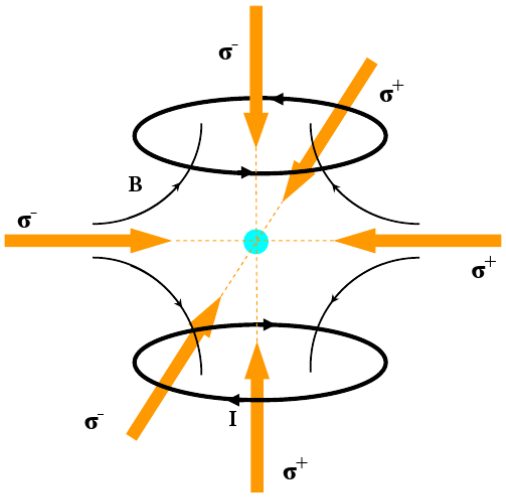

Figure 4.3: Magneto-optical trap (MOT) is created with three perpendicular pairs of counter propagating circularly polarized laser beams, intersecting in the zero magnetic field point provided by anti-Helmholtz coils.

The MOT at KVI is created (fig. 4.3) in the middle between two anti-Helmholz coils. Currents in these coils are counter propagating thus providing a zero magnetic field in the center and increasing in all directions. Atoms which are away from the zero B - field point are influence by the gradient of magnetic field (≈30 Ga/cm). Three perpendicular pairs of counter propogating circularly polarized laser beams are intersecting in the zero field point. The laser beams are red-detuned from the "main transition frequency" thus the sodium atoms moving with higher velocity against the laser beam have the Doppler shifted transition energy closer to the laser photon energy. That means that the atoms moving in any of the directions from the zero point region are effectively cooled. As they cool down their less Doppler shifted transition frequency is above the laser frequency and in the absence of a magnetic field they can simply drift out of the intersection region. Here the magnetic field gradient comes into a play to confine the atoms. The Zeeman shifted transition energy

start to be again closer to the resonance outside of the zero point thus cold ions again are pushed back towards the centre of the trap. The nucleus of the sodium atom has a spin of $I = \frac{3}{2}$ thus the ground $3s^2S_{1/2}$ and excited $3s^2P_{3/2}$ states are hyperfine split into 2J+1, i.e 2 and 4 components respectively. "The main transition frequency" was chosen to be of the difference between $F_{gnd} = 2$ and $F_{exc} = 3$ states (F is a full orbital momentum of the atom) and was correspondent to 589 nm in wavelength. Additionally another ("repumping") frequency resonant to the $F_{gnd} = 1 \rightarrow F_{exc} = 2$ transition was used to bring the atom in the $F_{gnd} = 1$ into the cooling cycle. This state can be occupied initially or due to the relaxation from the $F_{exc} = 2$ into which the atoms can be excited accidentally from the $F_{gnd} = 2$ state by the cooling laser, due to the non-zero line width of the transition, Doppler and Zeeman shifts. The light beam was provided by a dye laser pumped by a solid state 532nm CW laser. The additional "repumping" frequency was obtained from the +1 sideband of the electro - optical modulator (EOM) through which the laser beam passed before entering the optical fibre. After the fibre the beam passed through two acousto - optical modulators (AOM). The +1 order (deflected and frequency shifted light) of the first AOM was used to cool the atoms and the 0th order (not deflected light) passed through the second AOM, 0th order of which was used for the oven atoms deceleration. For the measurement, to have all atoms in the cloud in the ground state, the first AOM was switched off and the second was on to get rid of the laser light (the MOT cloud in the absence of the cooling beams expanded only slightly (few μs) [Kno06]). The first order of the first AOM was splitted into three laser beams of equal intensities during the cooling cycle by a couple of beam splitters. Afterwards the three beams passed through quarter waveplates to obtain the necessary circular polarization. Finally already orthogonal beams by "retro - reflecting" provided six MOT laser beams. The resulting MOT cloud usually is around a few 10^6 cold (200-300 μK) Na atoms in a volume of 1-5 mm^3 [Kno06]. Also not to disturbe during the experiment the recoil ions trajectories the magnetic field is also switched off.

4.3.2 RIMS

The recoil ion spectrometer used in the experiment one can see on fig. 4.4. The voltages applied to the spectrometer's 4 extraction electrodes were simulated (in SIMION 7.0) and set to obtain better spatial and temporal resolution [Has06]. The free field drift length of 41 cm follows the extraction part and ends up with a 2D position sensitive detector. The detector itself is a combination of two MCPs and a delay line. MCPs are used as an amplifier producing numerous electrons when a recoil ion hits the detector. The electrons from MCP hit a wrapped wire on each end of which there is a time-to-digital (TDC) converter. The time difference between the signals on both ends gives a position on the detector in one direction, for another direction another wire

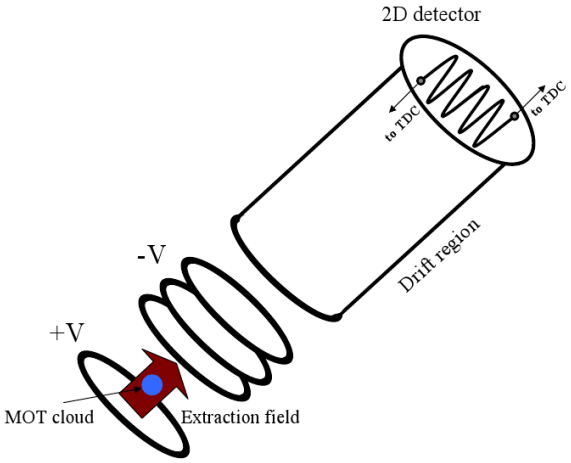

Figure 4.4: The Recoil Ion Momentum Spectrometer (RIMS) at KVI used in the ion - atom collision experiments.

(with another couple of time-to-digital converters) is wrapped perpendicularly to the first one. Such a system gives resolution of 0.1 mm which with a chosen voltage on the extraction electrodes provided a resolution of around 0.1 atomic units for the recoil ion momentum. In addition one of the four signals from a time-to-digital converter can be used as a time-of-flight information. If the ion beam is not continuous but short-pulsed, then different recoil charge species hit the detector at different time after the collision. This information can be used to get ratios of different charge states created during the collision or to study momentum distribution for a certain charge state of recoil ions in coincidence with the projectile pulse, thus the RIMS technique is in principle well suitable for the multiple charge exchange investigation. In our experiment the continuous ion beam was used and more than a single electron ionization of the Na atom was simply neglected (due to the very low intensities of other charge species).

4.3.3 Experimental results and discussion

The interaction of the He^{2+} ion with matter is of high interest for atomic and astrophysics, additionally one can apply knowledge of different cross sections to bio- or material research as the α-particle radiation is one of the general forms of radioactivity. Sodium atom being an alkaline atom in its turn is a quasi-single electron system for study. Previous research [Kno05] was performed to investigate the dependence of the single-electron capture and ionization cross

sections on the projectile velocity. To go to higher velocity regime in this work the ^3He isotope was used. As the valence electron binding energy in the sodium atom is equal to 5.14 eV, this means that the projectile kinetic energy should be 9.5 keV/u to have the same projectile ion and target electron orbital velocities. As mentioned in the previous section, these velocities should be compared to understand the ionization cross section behaviour. So the investigated velocity region was 9 - 14 keV/u, thus equal and a bit above the valence electron orbital velocity. With an intensity of the ion beam of $\approx$ 10

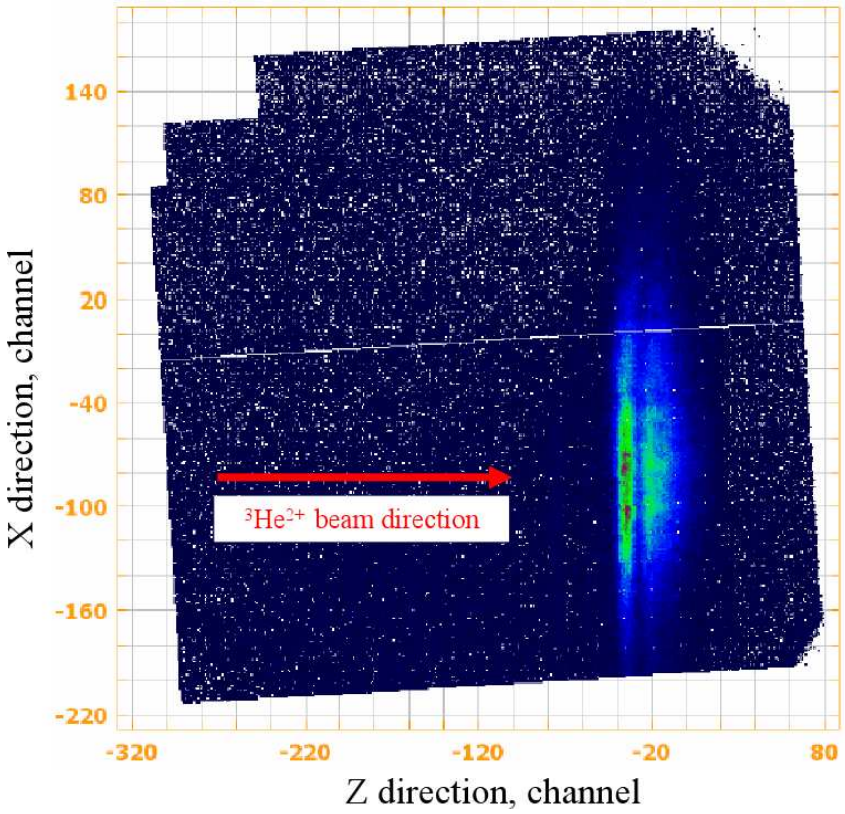

Figure 4.5: 2D picture on the RIMS detector of Na^{1+} recoil ions created in collisions of He^{2+} ions on the MOT target. The scale of the figure is 10 ch/mm.

nA and a number of atoms in the MOT cloud of $\approx 10^6$, the count rate of recoil ions on the 2D detector was around 200 events per second. Thus one hour of acquisition time was enough to have a good statistics. Events were written in a list-file read by a COBOLD software which created a 2D picture from the detector (see fig. 4.5, as an example, for the 9 keV/u projectile ion beam). The same software was used to handle and analyze the data. For instance, for our purposes this program was used to get the longitudinal (parallel to the ion beam) recoil ion spatial distribution on the 2D detector projecting the signal onto the Z - axis. Thus knowing the projectile kinetic energy and taking into account the proportionality between the recoil ion momentum and the position

on the detector one can get the Q - value distribution from eq. 4.7 (with s=1, corresponding to single-electron ionization). To get the Q - value in absolute [eV] not reference energy units one need to know exactly a reference point in the recoil ion spectrum. As a reference point a peak corresponding to the capture into the n=3 electron shell of the sodium atom was used. This channel is well-known to be the most probable one at low energies as can be obtained, for example, from the CBM model, which shows that the maximum of the reaction window (see fig. 4.6) of the investigated collision regime is very close to the Q - value (-0.91 eV) of the n=3 capture process. This peak is separated enough to be well resolved and thus serves nicely for the calibration.

To obtain absolute cross sections for the different capture channels and ionization one can use a simple formula:

$$\sigma = \frac{R}{JN_{MOT}}, \tag{4.8}$$

where R is the count rate, J the ion beam density, and N_{MOT} the number of the atoms in the MOT overlapping with the ion beam. As the stability of all the parameters is difficult to control over time and to determine the number N_{MOT} is a real challenge itself, the known total single-electron capture cross section was used to obtain partial capture and total ionization (capture into continuum) cross sections. The total electron capture cross section was extensively studied experimentally and theoretically [DuB86, Sch92, Sch95, Jai96] and thus is known with high precision. A list of the used cross sections (taken from [Kno06]) is given in the table 4.1.

After a Q - value plot is built, assuming a Gaussian shape of each peak[1] corresponding to a capture into a certain electron shell, one can fit the data with Gaussians, the central positions of which are well known from literature[2](see also table. 4.1). The sum of all capture channels (Gaussians) will give us a value proportional to the total capture cross section (σ_{tot}^{cap}). To obtain partial capture cross sections (σ_{n}^{cap}) one can use the relation

$$\sigma_{n}^{cap} = \sigma_{tot}^{cap}\frac{S_{n}^{cap}}{S_{tot}^{cap}}, \tag{4.9}$$

where S_{n}^{cap} and S_{tot}^{cap} are the signals under the n^{th} channel curve and the sum under all capture channels, respectively. For the ionization cross section one subtracts the signal of the total capture cross section from the total measured

[1] If one assumes a straight line trajectory of the projectile ion, the longitudinal momentum transfer should be fixed (eq. 3.6) and related to the Q-value of the process. The Coulomb repulsion acts mostly in perpendicular direction thus the longitudinal momentum components of the recoil ions should be statistically distributed around the fixed Q-values, motivating the usage of the Gaussian fit.

[2] The position is equal to: $5.14 - \frac{4 \cdot 27.2}{n^2}[eV]$, difference between sodium valence electron binding energy and the hydrogen-like helium atom levels.

signal (S_{tot}) using the formula:

$$\sigma^{ion} = \sigma_{tot}^{cap} \frac{S_{tot} - S_{tot}^{cap}}{S_{tot}^{cap}}. \tag{4.10}$$

Table 4.1: The Q - values for capture into different projectile states and reference total capture cross sections for different projectile ion energies used for calculations (eqs. 4.9 and 4.10).

capture channel	Q - value (eV)	projectile ion energy (keV/u)	σ_{total}^{cap} $\times 10^{-16} cm^2$
n=3	-0.91	9	107
n=4	1.74	10.6	88
n=5	2.96	12	75
n=6	3.63	13.3	63
n=7	4.03	14	57
Ionization	>5.14		

As the fitting process with independent Gaussians becomes difficult for higher and higher n - states, due to the big number of fitting parameters, the number of free fitting parameters was substantially reduced by taking into account the n^{-3} dependence of the capture cross sections (as mentioned in chapter 3) to fit further the data. Considering the fixed central positions of the peaks and the slightly different widths[1] the fitting process is reduced to a fitting of almost only five amplitudes of the first capture levels, then other $n \geq 8$ capture channels were added with amplitudes $(7^3/n^3)S_n^{cap}$. A result of such a fitting is shown in fig. 4.6. Then using formulas 4.9 and 4.10 one can obtain the correspondent capture cross sections, see fig. 4.7, which are listed in table 4.2.

Error bars for the cross sections extracted from the statistical analysis are below $10^{-16} cm^2$, which is true for the capture into the $n = 3$ - shell due to the nicely resolved peak. For other capture channels and ionization the statistical analysis tends to underestimate the error bars and the real uncertainties should be higher due to several reasons: unresolved mixture of signals for capture into $n > 3$ shells, fitting of the measured signal relied on the n^{-3} dependence, only partial fitting of the experimental curve with a "free" tail of ionization, still rather big number of parameters.

As the collision regime was around and above the electron orbital velocity the close coupling methods are the best to apply for theoretical calculations in

[1]The width of a Gaussian is determined by the natural width of the level on the projectile into which the capture occurs and by the setup resolution. The natural line width is slightly increasing for higher projectile levels, but is negligibly small in comparison with the instrumental resolution (around 1.5 eV).

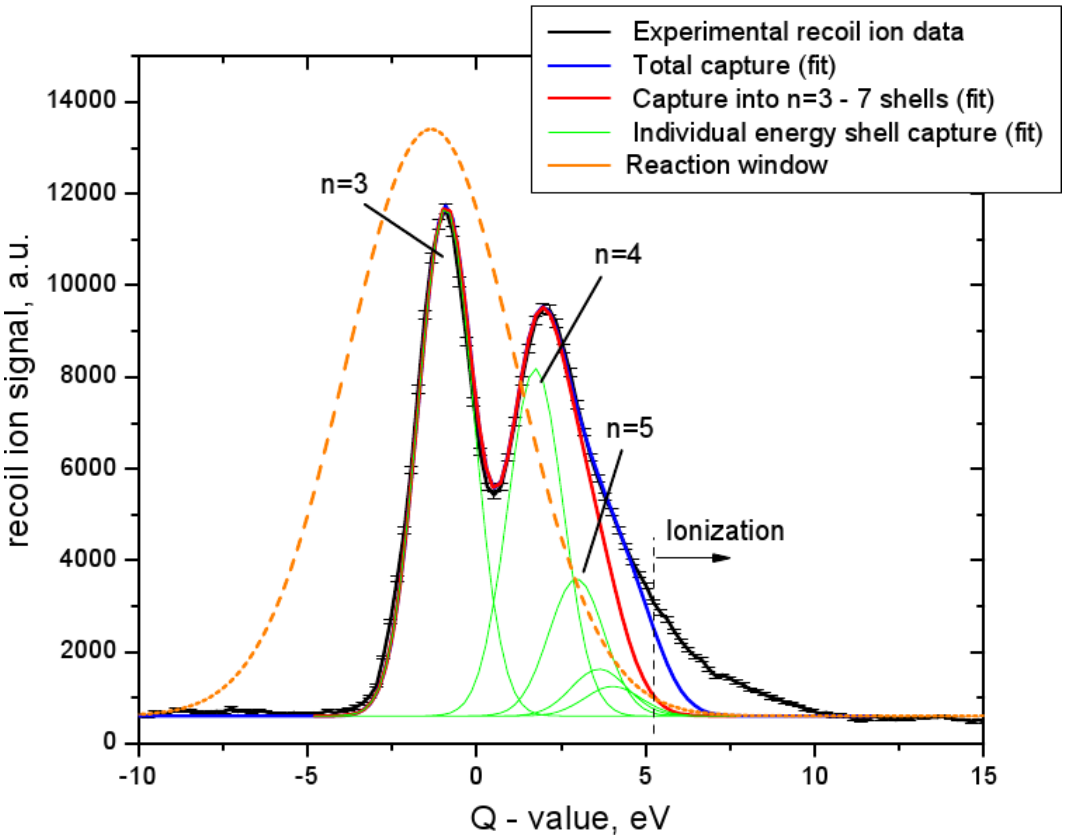

Figure 4.6: Q - value spectrum of the Na^{1+} recoil ions created in 13.5 keV/u $^3He^{2+}$ collisions on MOT target (Na) with a fit to obtain the differential cross sections for electron capture into a certain electronic state with quantum number n. The Q-value plot was obtained projecting the 2D signal from the RIMS detector (fig. 4.5) onto the Z - axis and then using eq. 4.7 for conversion. Reaction window from the CBM model is also included for the single-electron capture process.

this region for the determination of the capture cross sections 3.2. The main idea of the close coupling methods is to expand the electronic wavefunction on a finite basis set of states. Then the time-dependent Schrödinger equation is solved for the wave function, resulting in a set of coupled equations for the coefficients in the expansion, which determine the probability of electron capture during the collision into different states. As a basis usually molecular (MO) or atomic (AO) orbitals are chosen, but also other types can be applied, like Sturmian pseudo-states [Win82]. In fig. 4.7 one can see a result of two-center 74-state Sturmian-pseudostate expansion (SAO74) approach from [Jai96] which shows an adequate dependence for capture into n=3, 4 shells.

The dependence of the ionization cross section on the fig. 4.8 is far from the simple free-electron approximation (chapter 3). According to the SAO74 calculations [Jai96], the ionization cross section has a maximum around 21 keV/u of the projectile ion kinetic energy, correspondent to the $v_p \approx 2.1\sqrt{I}$

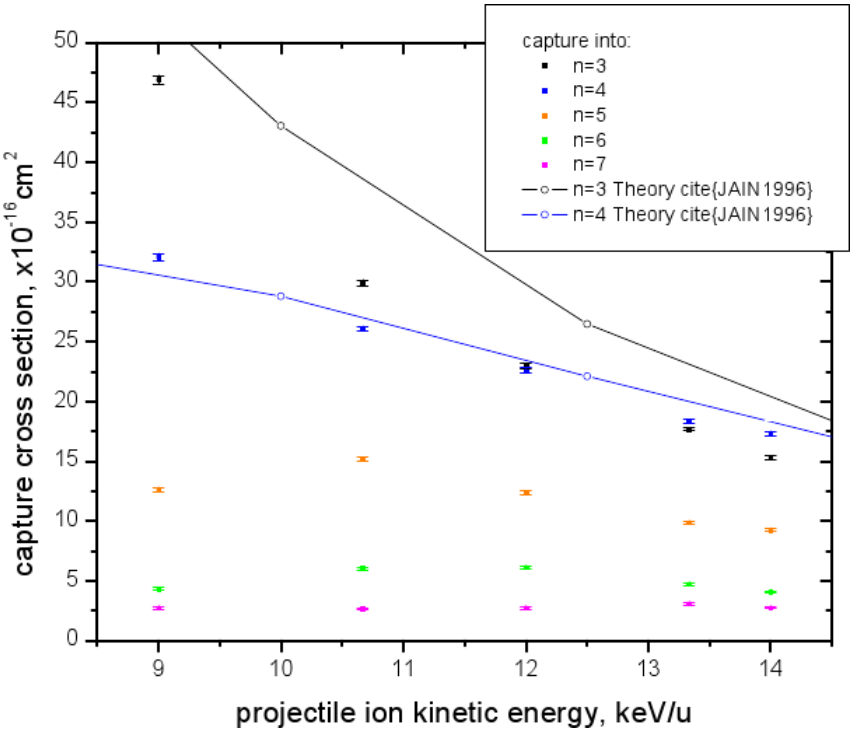

Figure 4.7: The resulting capture cross sections of the Na valence electron into the $n = 3, 4, 5, 6, 7$ bound states of the He^{2+} projectile ion. Also calculated values (from [Jai96]) for capture into n=3,4 projectile electron shells are included.

in atomic units, where I is the ionization potential of sodium atom, and thus twice higher than the value predicted by the free electron model. The measured cross sections nicely reproduce the previously obtained result with ^4He and show further increase of the ionization cross section, following the calculated curve. Only at 14 keV/u the cross section slightly decreases. That can be an artificial result after the fitting and thus additional measurements with higher resolution are required.

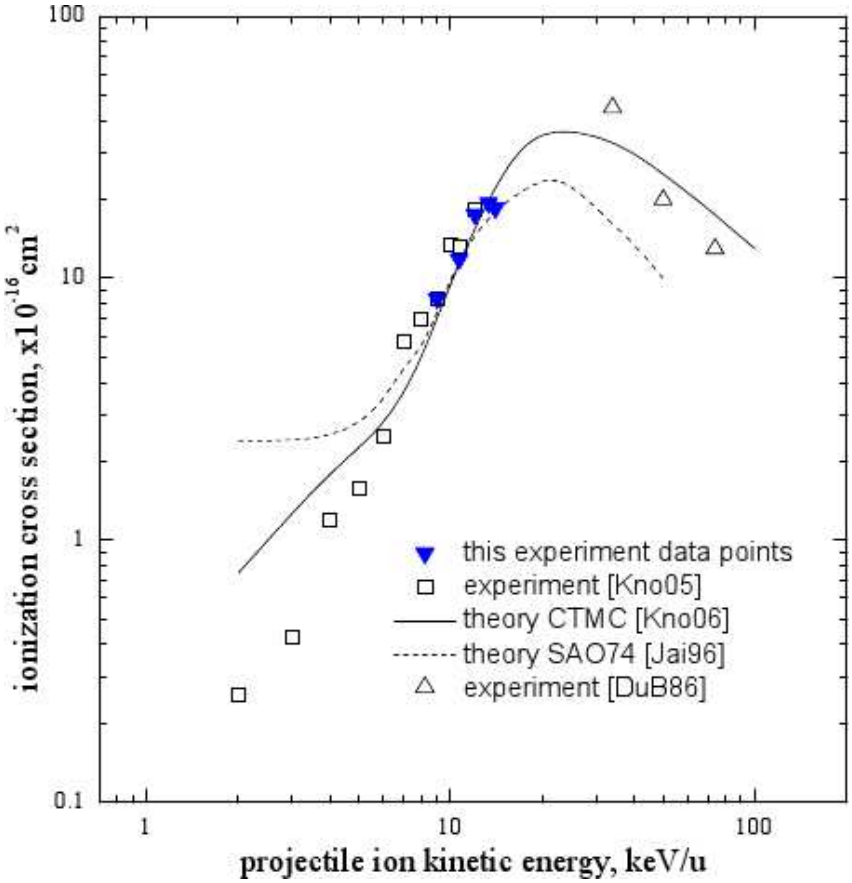

Figure 4.8: The resulting cross sections for ionization in the reaction $He^{2+} + Na \rightarrow He^{+} + Na^{+}$ with the previously measured experimental values and theoretical predictions from the CTMC and SAO74 calculations.

Table 4.2: Obtained cross sections for different projectile ion energies and different capture channels in the reaction $He^{2+} + Na \rightarrow He^{+} + Na^{+}$.

energy (keV/u)	$\sigma_{n=3}$ $10^{-16}cm^2$	$\sigma_{n=4}$ $10^{-16}cm^2$	$\sigma_{n=5}$ $10^{-16}cm^2$	$\sigma_{n=6}$ $10^{-16}cm^2$	$\sigma_{n=7}$ $10^{-16}cm^2$	$\sigma_{ionization}$ $10^{-16}cm^2$
9	46.9	32.1	12.7	4.3	2.7	8.4
10.6	29.9	26.1	15.2	6.0	2.7	11.9
12	23.0	22.6	12.4	6.1	2.7	17.6
13.3	17.7	18.4	9.8	4.7	3.1	19.4
14	15.3	17.3	9.3	4.1	2.7	18.6

Chapter 5

Ion sources

Collision studies of light and medium mass HCI and atoms at low and intermediate velocity regimes don't require huge accelerator facilities. For these experiments an appropriate ion source is enough (as the ECR ion source in KVI experiment). Single and multiple electron charge exchange between HCI and neutral atoms find a practical application in investigation of the plasma in the ion sources themselves. For example the knowledge on electron capture can offer an opportunity to manipulate the charge states of ions produced by the source. In this chapter the principles and basic processes in two types of ion sources, i.e. EBIT/S and ECRIS, are described.

In this and following chapters, if not specified, SI units are used as default units .

5.1 EBIS/T

5.1.1 Introduction

The electron beam ion sources were first proposed in 1967 [Don67] and have being used extensively since that time over 40 years. The sources found a lot of fundamental and applied areas of research, though the field of EBIS investigation itself is far from closed. Modern devices vary greatly from really powerful and expensive, like the EBIS in Brookhaven National Laboratory [Bee99] capable to produce several 10^9 Au^{35+} or U^{45+} per pulse, to very compact and rather cheap like Dresden EBIS-A [Ovs07]. A scheme of an EBIS is represented on a fig. 5.1. So it consists of an electron gun, a drift tube structure and a collector. The middle electrode of the drift tube section, called ionization chamber, is surrounded with a solenoid creating a strong magnetic field inside. Electrons starting from the cathode to which a negativ potential ($U_{cathode}$) is applied are accelerated in the region between the gun and the drift tube structure which is under positive potential (U_{ion}), thus the electrons kinetic energy in the middle drift tube is equal to: $(|U_{cathode}| + |U_{ion}|)e$. As the electrons enter the strong magnetic field region they are focused radially via the Lorentz force and create

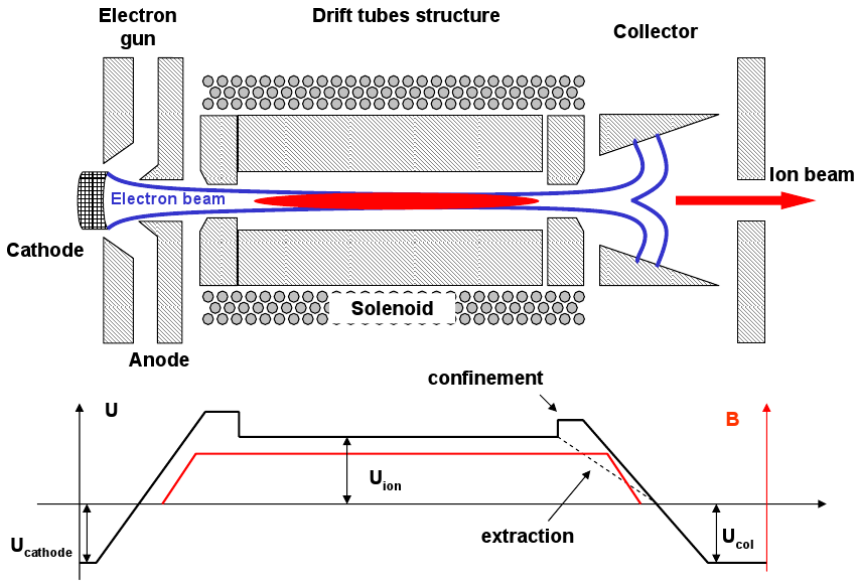

Figure 5.1: A sketch of the EBIS design with electric and magnetic field profiles.

a high density electron string in the ionization chamber. After passing the drift tubes, electrons enter the collector region where they are repelled on the walls with a negative voltage to prevent their influx further into a beam line. The overall potential and magnetic field profiles are schematically shown on fig. 5.1. The electron string in the ionization chamber strips atoms of a gas in the middle drift tube via electron impact ionization and additionally creates a radial potential well for the positively charged ions. Thus in the drift tubes section the ions are confined radially with electric and magnetic fields. Longitudinal confinement is provided with slightly higher potentials on the side electrodes in comparison to the middle one. Trapped ions in the source obtain sucessively higher charge states in collisions with electrons. After a certain confinement time τ_{cnf} the potential on the barrier drift tube is dropped and ions are extracted into a beam line with energies $U_{ion} \cdot q$, where q is a charge state.

The HCI in the source capture electrons from the surrounding gas atoms, as well as from the electron string, thus the EBIS is also a source of X-rays. As the appearance of the X-rays is always a good indication of a high charge state ion production, it is always very helpful to have an access with an appropriate detector to the ionization region. With a solenoid, mainly used for EBISes one can measure X-rays only looking on the exit of the source. That fact makes observation somtimes impossible for realization and additionally creates a huge background coming from the electrons Bremsstrahlung. Modernization of the EBISes brought designers to the EBIT devices, where instead of a solenoid, magnetic field in the ionization chamber is created by split coils or a pair of permanent magnets. This modification allows an easy access to the trap region

perpendicularly to the axis through a Be-window and direct observation of the X-rays from the production chamber. Except of the mentioned feature EBITs and EBISes are absolutely identical in terms of construction.

5.1.2 Ion creation

The ion production in the source occurs due to electron impact ionization which has the biggest cross section for removing a single electron from the atom(ion). Due to this fact the ionization is usually assumed to be a step like process with transition probability of the ion from charge state q to charge state $q+1$:

$$P_{q,q+1} = \sigma_q j \tau_{cnf}, \tag{5.1}$$

where σ_q is a cross section of the process, j - electron number flux density and τ_{cnf} - confinement time. If j is constant and the number of atoms is fixed in the trap then all of them will be ionized to 1+ charge state during $\tau_{cnf} = 1/(\sigma_0 j)$ time. To get all the ions in higher than $(q-1)+$ state the neccessary confinement time should be:

$$\tau_{cnf} = \frac{1}{j} \sum_{i=0}^{i=q-1} \sigma_i^{-1}. \tag{5.2}$$

To get the charge state distribution at any moment of confinement, a system of differential equations needs to be solved:

$$\frac{dn_i(t)}{dt} = (1-\delta_{0i}) j \sigma_{i-1} n_{i-1} - (1-\delta_{qi}) j \sigma_i n_i, i = 0, 1...q \tag{5.3}$$

where δ_{ij} is the Kronecker delta symbol, n_i is the number of ions in $i+$ charge state and n_0 is a number of neutral atoms in the beginning. The equation is based on the balance approach [Kos83] which assumes that the change of the number of ions in $i+$ state is increasing because of the further ionization of $(i-1)+$ ions and decreasing due to the ionization of the $i+$ charge state to $(i+1)+$. The system of equations has an analytical solution:

$$n_i(t) = \frac{n_0(0)}{\sigma_i} \sum_{k=0}^{i} \sigma_k e^{-j\sigma_k t} \prod_{c=0}^{i}{}' \frac{\sigma_c}{\sigma_c - \sigma_k}, \tag{5.4}$$

where the prime on the product sign excludes the term $c = k$. For the cross section σ_i one can use already the Rutherford formula 3.16 from the 3rd chapter, where instead of the ion $q+$ one should use the electron charge $1-$. Usually for the charge evaluation a semiempirical Lotz formula is used [Lot68]:

$$\sigma_i = 4.5 \cdot 10^{-14} \sum_k \xi_k \frac{ln\epsilon_k}{\epsilon_k I_{i,k}^2}, \tag{5.5}$$

here $I_{i,k}$ is the ionization energy of the k^{th} electron subshell of the ion in eV units, $\epsilon_k = E_e/I_{i,k}$, with E_e an electron kinetic energy (eV units) and ξ_k is the number of equivalent electrons in the k^{th} subshell. Resulting cross sections are in cm^2.

5.1.3 Ion charge exchange

The formula 5.4 is not true for the normal EBIS operation with gas injection, because of the continuous influx of the neutral atoms into the electron string. To describe the ion charge states evolution even more precisely, one should also include into the system of equations 5.3 different charge exchange mechanisms with the environment, which slow down the production of HCI. Except of the single electron capture from neutral atoms, for which the cross section can be calculated for example via formula 3.20 coming from the classical-over-barrier model, ions lose there charge states because of the radiative recombination(RR). RR is the process by which an ion binds an electron from the electron beam. The radiative recombination is quite unlikely for lowly and multiply charged ions[1]. For HCI, especially when the electron bombarding energy is close to the energy of the electron shell closure lowering HCI production rate, RR can influence dramatically. Modern programs like CBSIM [Bec07] take into account all mentioned processes. On fig. 5.2 one can compare results for the charge breeding of oxigen with and without gaseous surrounding calculated with CBSIM.

It can be seen that for the gaseous environment the charge states evolution stops at some moment and further increasing of the confinement time won't influence the charge distribution. Charge abundances are constant when the trap is full and plasma in the chamber is in the equilibrium. The number of ions in a certain charge state produced by the EBIT per pulse, when the trap is full, one can get from abundances and knowing the capacity of the trap. The total number of positive charges is assumed to be equal to the number of bombarding electrons in the trap region, so called charge compensation limit, equal to:

$$Q[C] = \frac{5.33 \cdot 10^{-10} I[A] l[cm]}{\sqrt{E_e[keV]}}, \tag{5.6}$$

here I is the electron current, l - trap length and E_e - electron energy, corresponding units are in square brackets. As the barrier voltage is raised, the trap is closed and filled with ions, which change continuously there charges climbing to the highest charge state at the equilibrium.

[1]For radiative recombination with bare ions, Bethe and Salpeter (1957) gave the following analytical formula to calculate capture cross section into the hydrogenic final state n: $\sigma_n[cm^2] = 2.1 \cdot 10^{-22} \frac{Z^4 Ry^2}{nE_e(n^2E_e + Z^2Ry)}$, where E_e is the electron energy, Ry is the Rydberg energy and Z is the ion charge state, which in the case of not bare species can be replaced with an effective value [And91].

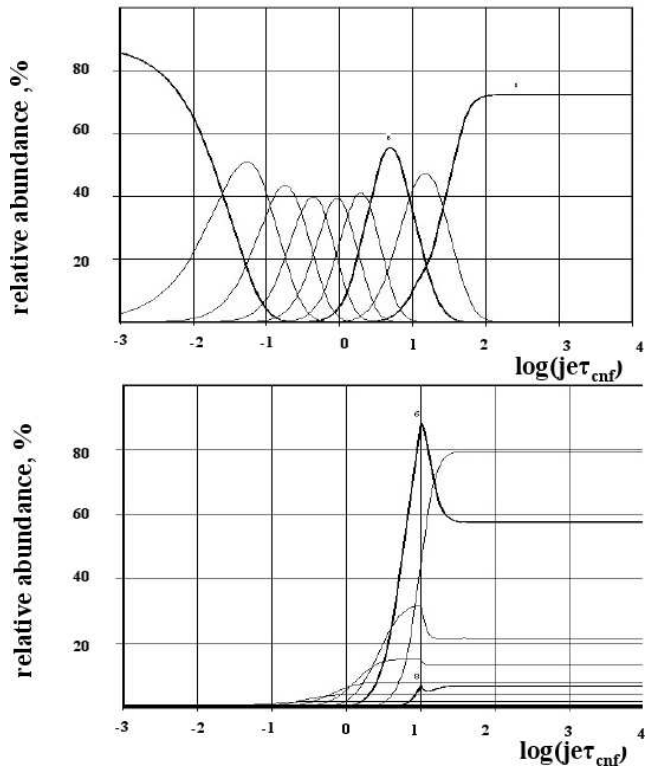

Figure 5.2: CBSIM simulation of oxygen charge state abundances $vs\ je\tau_{cnf}$ parameter, where j is an electron number density, e - electron charge and τ_{cnf} - confinement time. Top, simulation with a fixed number of atoms in the trap and bottom, simulation with a continuous influx of the neutral gas.

Programs calculating numerically the charge evolution take into account the electron impact ionization and electron capture which is treated usually as a single electron process[1], though for heavy HCI a multiple electron charge exchange dominates at low energy. Still the lack of experimental data in this collision regime and the difficult theoretical treatment can not provide enough information on the cross sections. To suppress the electron capture, high vacuum in the source should be achieved which unfortunately also slows down the filling of the trap.

5.1.4 Electron beam

Looking on the formula 5.1 one immediately see that the probability of getting higher charge states increases with higher electron number current density:

$$j = \frac{1}{e[C]} \frac{I[A]}{\pi R_0^2[m]}, \tag{5.7}$$

[1]For CBSIM the single electron capture cross sections are taken from [Mue77].

with I - electron current and R_0 - radius of the electron beam. Thus intense electron beams are favorable for HCI production, increasing the ionization probability and the trap capacity eq. 5.6. To increase the density the electron beam is usually focused into the magnetic field where a further compression takes place. A certain electron volume charge density n_e can be confined with a minimum magnetic field:

$$B_b = \sqrt{\frac{2n_e m_e}{e\epsilon_0}}, \tag{5.8}$$

where

$$n_e = \frac{2m_e}{e\epsilon_0}\frac{I}{\pi R_0^2 v_e}, \tag{5.9}$$

m_e, e, v_e are the electron mass, charge and velocity, respectively, R_0 - radius of the electron beam and ϵ_0 - the vacuum permittivity. The formula 5.8 is derived from the laminar flow model [Bri45] under an assumption that the current is formed in a magnetically shielded electron gun. One can also treat the problem from the optical model point of view [Her57] when electron starting point on the cathode emits in all directions according to the Maxwellian distribution. The model gives the minimum magnetic field to compress the electron beam to the radius R:

$$B = \sqrt{B_b^2 + \frac{8k_B r_c^2 T m_e}{e^2 R_0^4} + (\frac{r_c^2 B_c}{R_0^2})^2}, \tag{5.10}$$

where r_c the cathode radius, k_B the Boltzmann constant, T the cathode temperature and B_c magnetic field at the cathode. In equation 5.10 the required magnetic field is represented as a square root of three terms, accounting for space charge forces, thermal velocities and magnetic flux at the cathode. So one can see that the best density is achieved when there is no magnetic field at the starting point (cathode).

The electron string creates the potential well inside the ionization chamber which can be calculated from Gauss's law and equals to:

$$V(R) = V_{dt} - 2s^- ln\frac{R_{dt}}{R}, for R \geq R_0 \tag{5.11}$$

$$V(R) = V_{dt} - s^-(2ln\frac{R_{dt}}{R_0} + (1 - \frac{R^2}{R_0^2})), for R < R_0 \tag{5.12}$$

where V_{dt} and R_{dt} are the middle drift tube potential and radius, respectively, and $s^- = I/(4\pi\epsilon_0 v_e)$. The equation 5.12 shows that the ions in the electron beam are confined in the harmonic trap potential[1], i.e. $V(R) \propto R^2$.

[1]The radial electrostatic potential $V(R) = s^- \frac{R^2}{R_0^2}$ counted from the bottom of the potential well, in a presence of a magnetic field B, can be exchanged with an effective potential

$$V_{eff}(R) = V(R) + \frac{eq_i B^2 R^2}{8m_i} \tag{5.13}$$

, where q_i and m_i are the confined ion's charge and mass, respectively [Pen91].

5.1.5 Ion temperature

As the neutral atoms are ionized in the potential given by equation 5.12 the singly charged ions initial average energy ($\bar{U_1}$) can be calculated under an assumption of homogenious destribution of atoms in the trap with zero initial kinetic energies via the general formula:

$$\bar{U_1} = \frac{\int_0^{R_0} eV(R)n_0(R)2\pi RdR}{\int_0^{R_0} n_0(R)2\pi RdR}, \tag{5.14}$$

here $n_0(R)$ is the atom density. Substituting $V(R) = s^- R^2/R_0^2$ and $n_0(R)$-const, one can obtain average energy for +1 charge state: $\bar{U_1} = s^- e/2$. For each of the two ortoganal directions perpendicular to the optical axis there are two degrees of freedom (due to the motion in the harmonic potential), for the optical axis direction there is only one degree, thus 5 degrees of freedom in total. Sharing the average energy value in ion - ion collisions among all available degrees of freedom will give the ion cloud temperature from the equation: $k_B T_1/2 = s^- e/10$, T_i will indicate the temperature of a certain charge q_i [Cur03]. Cloud of singly charged ions is now appeared to be Boltzmann distributed in the potential well. For different charge states of ions q_i in the trap the Boltzmann relation is:

$$n_i(R)dR = N_i 2\pi R e^{-\frac{q_i V(R)}{k_B T_i}} dR, \tag{5.15}$$

here N_i is a total number of ions. "Freezing" singly charged ions at there positions distributed via Boltzmann relation and ionizing them further will give an increase of energy, substituting n_1 instead of n_0 into the equation 5.14, for doubly charged ions. Increase of the energy and thus of the temperature, when calculated, is less than the $k_B T_1$ while the charge in the equation 5.15 is increased twice, thus shifting the ion density distribution to the axis. Using the same approach for higher and higher charge states one can see that the temperature is also increasing and the spacial distribution is closer and closer to the bottom of the potential well (see fig. 5.3).

The described picture would be complete, if there was only a single charge state involved. In reality different ion charge species exchange there energy via Coulomb collisions. Interaction of ion q_i with ion q_j has a characteristic time $\tau_{i,j} \propto m_j q_i^{-2} q_j^{-2}$ [Cur03, Spi56], were m_j is a mass of the j^{th} ion. From the dependence one can see that the higher charge states are coupled stronger and obtain nearly similar temperature.

Except of the ion - ion collisions there is a Coulomb interaction of ions with electrons which heat up the plasma in the trap. The heating called after Landau and Spitzer has a rate $dT_i/dt \propto q_i^2 j/m_i$, where j is as usually the number electron current density.

Hot HCI are well confined in the trap and exchange there energy with other less charged ions transferring them there momenta. Singly and lowly

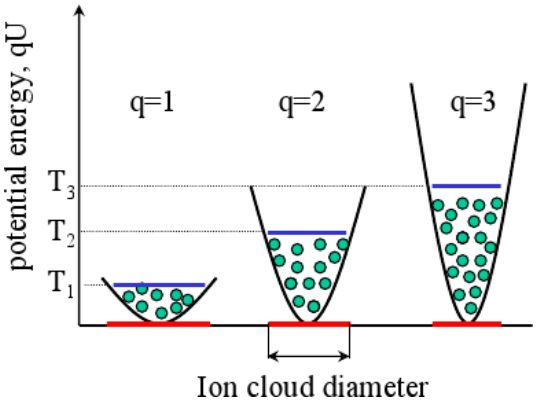

Figure 5.3: Different ion species in the trap. Higher charge states are better confined, but also have a higher temperature.

charged species with higher momenta can not be confined further in the trap and escape from it cooling the remaining ions. This evaporative cooling can be stimulated introducing a light gas into the trap [Kin01, Pen91a].

Escape of different ion species from the trap should be also included into the equations 5.3. So one can see that the plasma behaviour in the trap appeared to be quite complicated and difficult to describe.

5.2 ECRIS

Another ion source that produces high charge states is the Electron Cyclotron Resonance Ion Source (ECRIS). The ECRIS is used in GSI accelerator facility to produce multiply charged ions to be injected into the UNILAC (see chapter 2). As described in chapter 4, the ion - atom collision experiment at KVI was also performed with ions produced in an ECRIS. In this section a short overview of the main ECRIS operation principles is given.

Design of an ECR ion source should provide following features: appropriate magnetic field strength and structure, adequate microwave frequency and power, good vacuum and suitable extraction system. The ion source construction and plasma in the ionization chamber are depicted on fig. 5.4.

The magnetic field in the chamber is formed by two solenoids longitudinally and by a hexapole magnet radially so that the surfaces of the constant field strength are nearly ellipsoidal with a field increasing from the centre. On fig. 5.4, left, one can see a profile of such a B-field minimum structure along the axis.

The ion creation starts with injection of a gas and radiation of a microwave into the ionization chamber. There are always some free electrons in the chamber moving with a cyclotron frequency ω_c around magnetic field lines. When

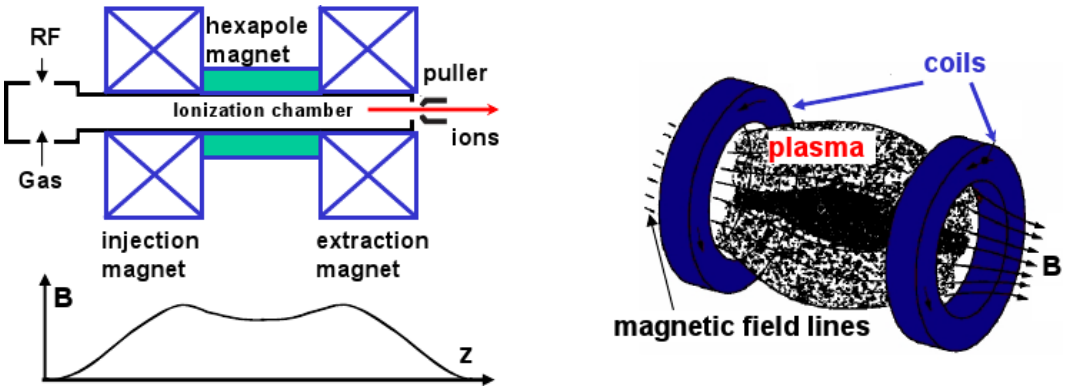

Figure 5.4: ECRIS design, left. Plasma in the source, right. Magnetic field confine electrons in the plasma chamber and the ions are trapped by the electron space charge potential.

the fed microwave is in resonance[1] with ω_c the electrons are accelerated to high energy absorbing RF power. Hot electrons in the ionization chamber with high orbital momenta feel the gradient of the magnetic field and are reflected back towards the center. The magnetic mirror is not ideal and there is a narrow escape channel along the axis for relatively hot electrons with small orbital momentum.

Hot electron impact ionization of the atoms feed additional electrons into the plasma. Removed electrons absorb the RF power and participate further in the ionization process. The ions are not so strongly influenced by the magnetic field and are confined by the electron space charge potential. The behavior of the ion cloud in the ECRIS has the same features as in the EBIT/S devices, i.e. step like ionization, electron heating, charge exchange with the environment and ion-ion Coulomb collisions. Produced ions leave the ionization chamber which is kept under a high positive voltage through the electron escape channel and are extracted continuously towards the grounded or put onto a negative voltage puller electrode. In case of the KVI ion source, as it was mentioned, the maximum ion energy was 42 keV for alpha particles, correspondent to the 21 kV potential of the ionization chamber. Higher energies were not achieved due to the frequent discharges causing instabilities of the plasma in the chamber.

As the ECR ion sources are not the main topic of this thesis, I refer for further details to [Tar05, Cur03]. Interesting information on investigations dedicated to improve the ECRIS performance can be found elsewhere, e.g. integration of the electron gun into the source [Run98], gas mixing [Tar04] or using an afterglow mode of operation [Mel94].

[1]The resonant microwave frequency used in KVI ECRIS is 14 GHz correspondent to the magnetic field of 0.5 T.

5.3 Singly charged ion sources

During this work two types of singly charged ion sources were used, briefly described below.

The first ion source was a sputter ion gun from KVI suitable for use with most gases. The source operation is based on the electron impact ionization. The intense electron beam from a filament is accelerated towards an electrode under a high positive potential and ionize the atoms, ions are accelerated into the opposite to electrons direction and extracted into the beam line.

The second type was a surface ion source from the HeatWave Labs, Inc. integrated into the specially designed "ion gun" fig. 5.5, left. The heating fila-

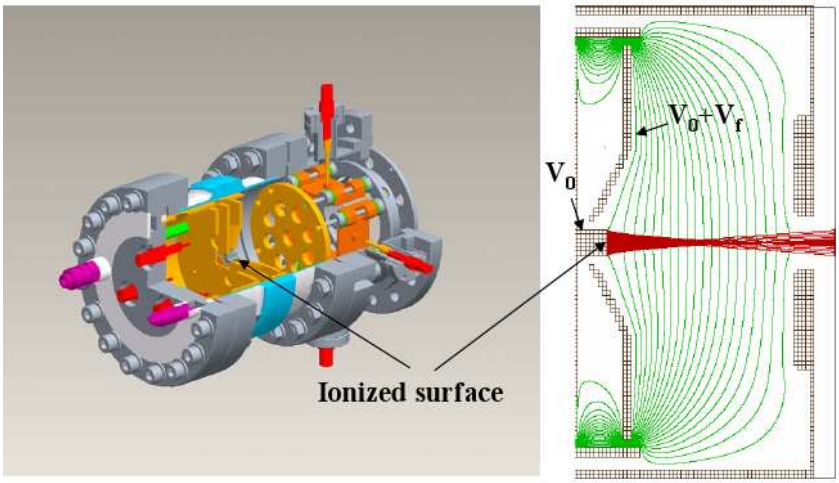

Figure 5.5: Ion gun with inserted ion source from HeatWave Labs, Inc. 3D design, left and SIMION 7.0 simulation, right. Green lines in the simulation are equipotential lines.

ment increase the temperature of the source body above $1000°C$ and evaporate singly charged ions and neutrals from the surface [1]. Ions are repelled with a positive potential applied to the body V_0 and extracted into the beam line, anode of the gun is usually under a higher potential $V_0 + V_f$ providing better focusing of the beam fig. 5.5, right. Different ion sources can be installed into the gun producing various singly charged elements, i.e. alkaline metals: Cs, K, ^6Li, ^7Li, Na, Rb and alkaline earths: Ba, Be, Ca, Mg, Sr.

[1]Ratio of ions in the total production rate can be obtained from the Langmuir-Saha formula:

$$\frac{n_+}{n_+ + n_0} = (1 + \frac{\omega_0}{\omega_+} exp(\frac{I - \varphi}{kT}))^{-1}, \tag{5.16}$$

where n_+ and n_0 are the numbers of ions and neutrals, respectively, produced per second, φ and I are the work function for the surface and the first (uppermost) electron ionization potential, respectively, ω_+ and ω_0 are the weighting factors, $\omega = 2S + 1$, where $S = \sum_i s_i$ the total electron spin of the ion or atom.

Chapter 6

EBIS/T setups and experiments

6.1 MAXEBIS setup and experiments

The MAXEBIS setup at GSI fig. 6.1 comprises a singly charged ion source, a multi-passage-spectrometer (MPS), a TOF spectrometer, several diagnostics (FCs and YAG scintillator screen) and the EBIS device itself [Kes06].

The MAXEBIS, built in Frankfurt University [by R. Becker], was installed at GSI for charge breeding experiments. It was designed for high electron currents up to 3 A, but was normally operated by us with 100 mA electron beam. The high current electron gun, based on a 2 mm IrCe cathode, was driven to an emission current density of about $95 A/cm^2$. The longitudinal position of the cathode with respect to the magnetic field could be varied with a manipulator. Hence the radial compression of the electron beam by the magnetic field gradient could be adjusted (see formula 5.10). The magnetic field was provided by a superconducting 5T solenoid surrounding the 80 cm long ionization chamber. The inner design of the MAXEBIS included several ion optical elements after the ionization chamber for better extraction of the ion beam.

The TOF spectrometer was designed for beam energies $\leq 2keV/q$. Such a limit was set by a resistor chain of the electrostatic mirror, which reflected the upcoming ion beam towards a channeltron. The voltage applied to the detector was 3 kV, thus the channeltron worked in the saturated regime, i.e. the signal was proportional to the number of ions, but not to the number of there charges. The spectrometer had a special chopper at the entrance to cut a short fraction of the ion pulse for the time-of-flight measurements.

The MPS essentially is a water cooled dipole electro-magnet, providing magnetic field up to 1.2 T. A vacuum chamber between the poles of the magnet has 4 arms, for beam entrance or exit. Each arm of the MPS is equipped with an Einzel lens which can be set on up to 10 kV potential. The MPS was used as a switchyard or an A/q analyser. The resolution of the 90° bending magnet is estimated to be better than 0.025 in rigidity, that's enough for example to separate Kr^{20+} and Kr^{21+} charge states. Switching off the current in the

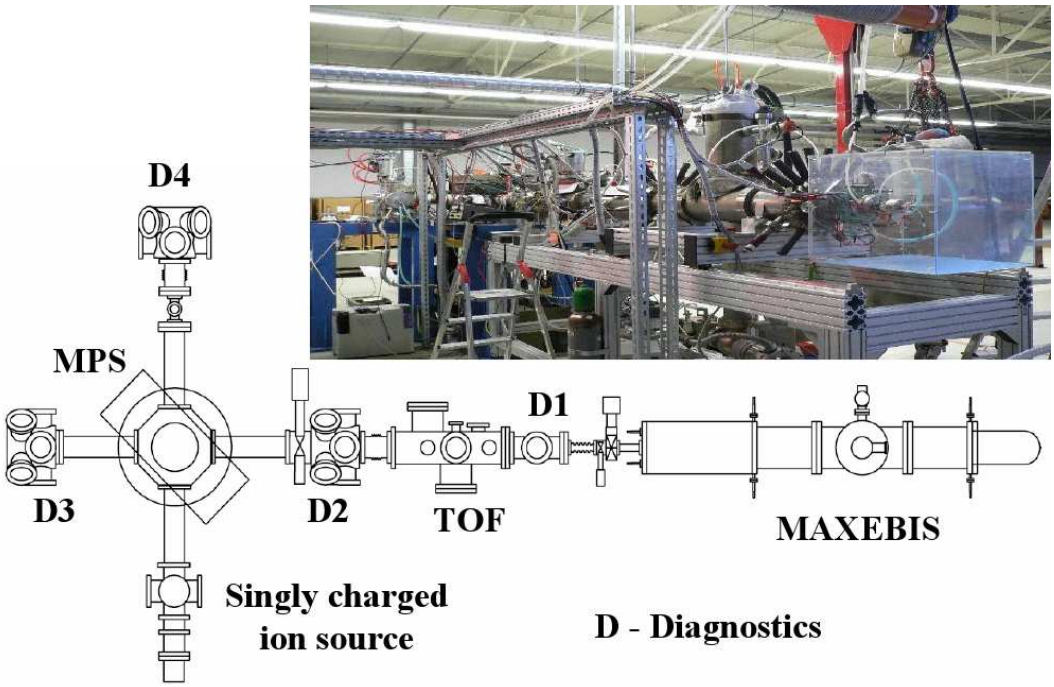

Figure 6.1: MAXEBIS setup at GSI, AutoCad drawing and photo. On the Autocad drawing one can see main parts of the beam line, i.e. MPS - multipassage spectrometer, TOF spectrometer, several diagnostics with Faraday Cups. In the D4 additionally a YAG scintillator screen and a camera were installed to allow beam profile measurements.

coils allowed to shoot the beam straight through the MPS towards another diagnostics.

The diagnostics were mainly the Faraday Cups except of the D4, where a YAG scintillator screen and a camera were installed for beam profile measurements.

Extensive simulations of the ion beam dynamics were performed using SIMION 7.0 [Dah00]. On fig. 6.2 one can see the whole setup with several zoomed instances: the MAXEBIS extraction system, MPS and singly charged ion source. Red lines indicate the trajectories of O^{5+} ions started from the ionization chamber under 4.5 kV towards the scintillator in D4. The simulated transmission of the beam line was around 50%, though in reallity was never better than 10% because of the TOF part between the MAXEBIS and the MPS. Simulations were done to improve the transport of the ion beam from the EBIS towards the MPS and from the singly charged ion source towards the MAXEBIS for injection, discussed in the 7th chapter. Simulation of the Einzel lens in the MPS arm also provided information on the focal lengths used for emittance measurements of the beam (see below).

The ions started there motion inside the ionization chamber in 5T magnetic

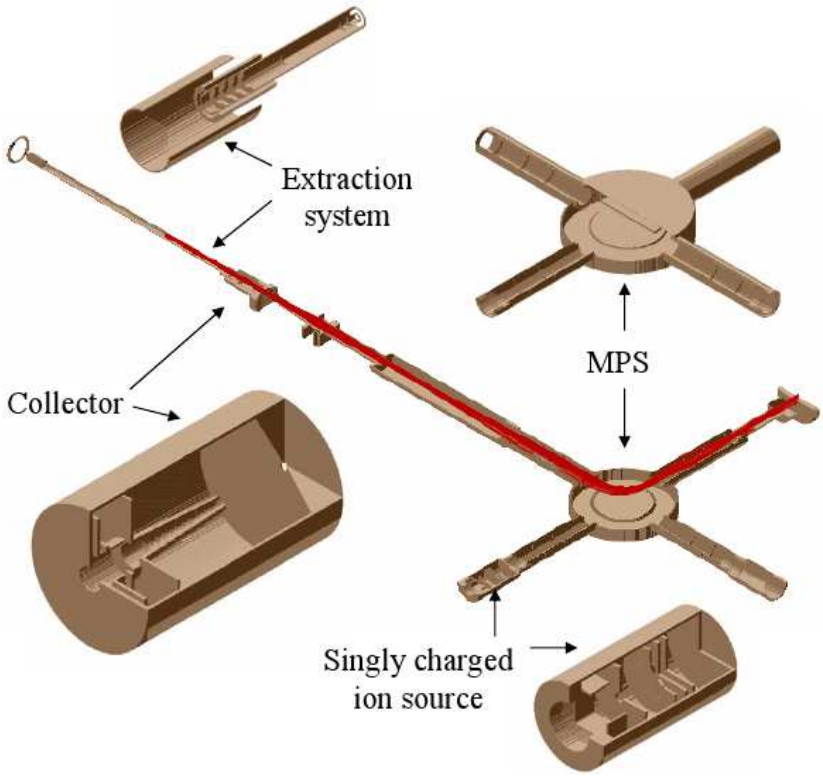

Figure 6.2: Simulation of the MAXEBIS setup, using SIMION 7.0. One can see the extraction part of MAXEBIS, MPS and singly charged ion source from separate instances. Red lines are the trajectories of O^{5+} ions starting from the ionization chamber and hitting the YAG scintillator screen after the MPS.

field. As they were extracted there motion was in the gradient of magnetic field, which influenced there trajectories. For better magnetic shielding of the collector another solenoid was initially designed in the collector region, which was also used as a focusing element. Magnetic field from both the superconducting magnet and collector coils was included into the simulation via SIMION's user programming. External file provided information on the radial and longitudinal components of the field at different positions. As the ion was moving, its position was read and corresponding magnetic field was applied from the file. The field distribution along the axis was calculated at first using a well-known formula for solenoids and later on with a more advanced tool - INTMAG [Bec99] simulation code, which is able to include iron shielding. Knowing the field along the axis one can calculate the radial magnetic field (see Appendix B). Both calculated and simulated magnetic field distributions are depicted on fig. 6.3.

Due to high costs of MAXEBIS run, conducted experiments were dedicated mostly to charge breeding of externally injected singly charged ions, covered in the 7th chapter. Nevertheless some basic characteristics of the ion beam

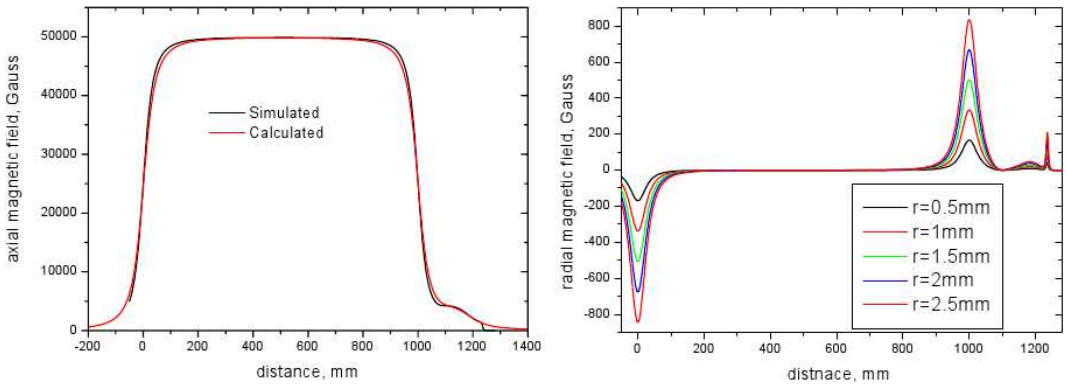

Figure 6.3: Calculated and simulated (using INTMAG) magnetic field distribution along the axis, left and extracted from the simulation radial components, right. The zero position corresponds to the beginning of the MAXEBIS superconducting magnet.

extracted from the source with and without injected inside Ar gas were also measured.

The emittance of the MAXEBIS O^{5+} ion beam (only residual gas in the ionization chamber) was measured after the MPS selection. The ions started at 4.5 kV potential of the ionization chamber and moved towards the YAG scintillator screen (see the simulation, fig. 6.2). Under different potentials applied to the MPS Einzel lens in front of the screen, the beam image radius was changed. Knowing the focal length of the lens under applied voltage and the radius of the beam one can estimate the emittance, using multi-gradient method (Appendix C). The focal lengths were obtained from simulations and the beam radii were measured from the beam spot image on the scintillator screen, see fig. 6.4, left. The beam image had huge aberrations which were also approved by simulations fig. 6.4, right.

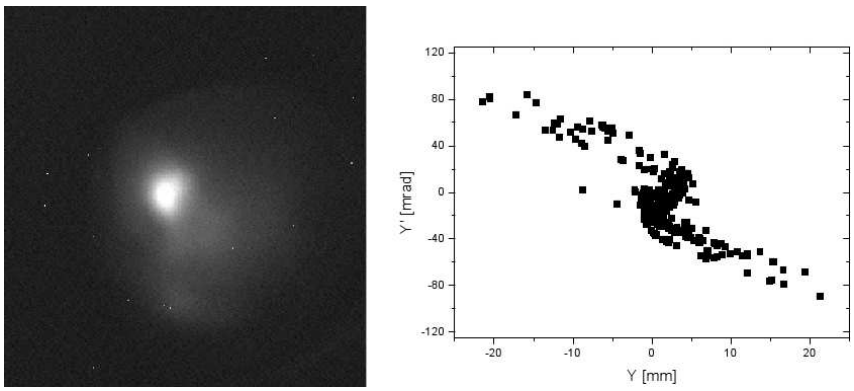

Figure 6.4: The O^{5+} beam spot on the scintillator screen, left and example of the final emittance ellipse (see Appendix C) at the same position from simulations, right.

The emittance was measured to be $250 \pm 100 mm \cdot mrad$. Partially the big value comes from aberrations, but another reason is a large energy distribution of ions inside the trap. In the EBIS devices with high magnetic field escape of ions from the trap happens mostly longitudinally over the potential barrier. During the emittance measurements the extraction drift tube voltage was set 100 V above the middle drift tube potential, meaning that the O^{5+} ions could escape only if they had more than 500 eV kinetic energy. Thus the hot ions, heated by the 6 keV electron beam, were still confined in the trap and increased the beam size and emittance.

During one of the MAXEBIS runs the charge breeding of injected Ar gas was performed. Unfortunately due to a relatively high background gas pressure and thus a big fraction of residual gas ion species in the TOF spectra the analysis was very difficult to perform (see fig. 6.5). One should only mention that the number of Ar highly charged ion species was increasing with increasing of the confinement time while the lower charge states were vanishing. After

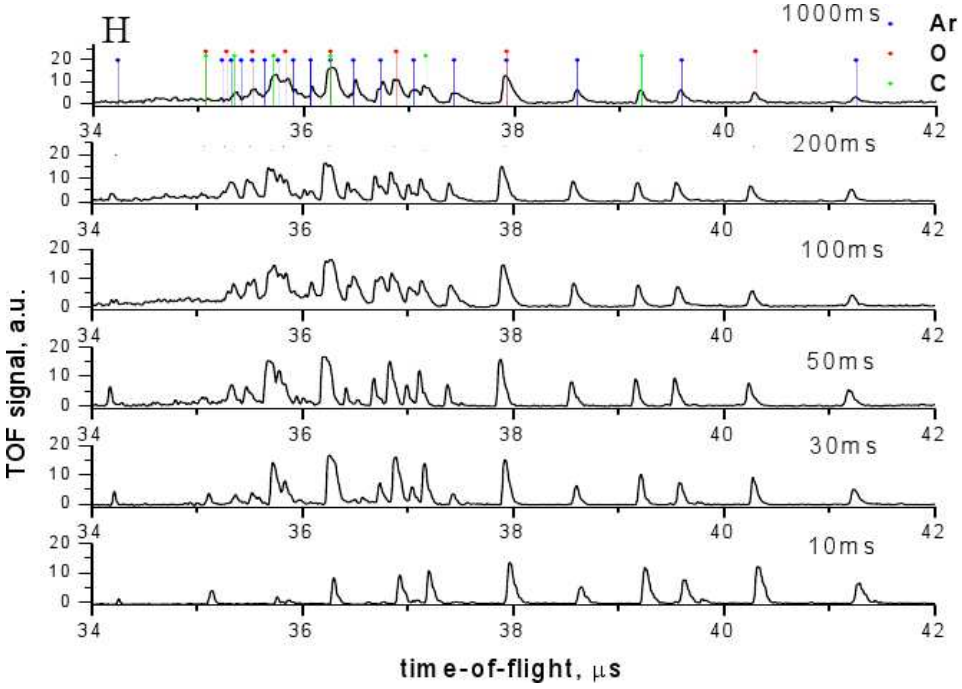

Figure 6.5: The TOF spectra with injected Ar gas, dependence on the confinement time. Ion kinetic energies: 1.5 keV/q, electron beam energy 3.2 keV.

500 ms of confinement, the spectra did not really change anymore, indicating the equilibrium of the ion plasma in the chamber. As the chopper of the TOF spectrometer cut only a small fraction of the beam, the total picture of the charge breeding process was unclear.

Another measurement on the confinement time was made with the total extraction pulse from the EBIS (see fig. 6.6) under the same conditions. The

picture to the left shows a typical pulse shape seen on the oscilloscope. The pulse had a width of approximately 100 μs and a high peak in the beginning. The peak appeared due to the ions located in the vicinity of the extraction electrode and thus immediately extracted as a short bunch after lowering the barrier potential. The remained ions in 80 cm long ionization chamber were rather slowly extracted drifting in the 5 T magnetic field towards the exit, thus creating an elongated structure. On fig. 6.6, right the dependence of the peak current on confinement time is also plotted, showing that the trap capacity was reached after approximately 200 ms.

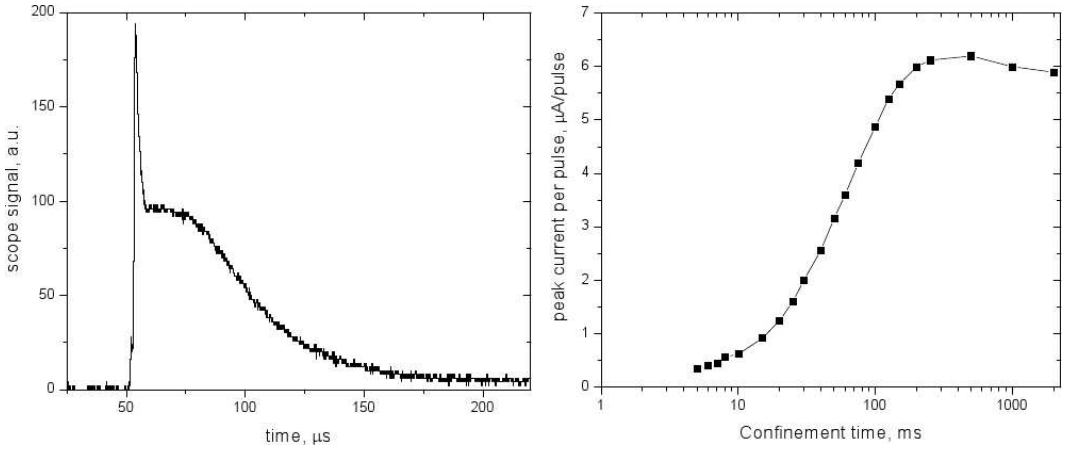

Figure 6.6: Extraction pulse from the MAXEBIS, left and its peak current dependence on confinement time, right. Ion kinetic energy 1.5 keV/q, electron beam energy 3.2 keV.

The experiments with MAXEBIS were performed only few times, but provided a good knowledge on the basic processes in the source. Due to the rather intense influx of the residual gas into the ionization chamber from the collector region, and due to the high running costs of the setup, it was decided to go to another test ion source. Provided with a good experience we started the next step.

6.2 SPARC EBIT setup and experiments

6.2.1 SPARC EBIT setup

The SPARC EBIT setup at GSI (fig. 6.7) had already mentioned parts, i.e. MPS and TOF spectrometer. In addition, several ion optical elements were included to improve the beam transport. The profile measurements were performed using the KVI diagnostics, equipped with an MCP - phosphor screen combination, installed after the new EBIT. The KVI diagnostics was the same as in the HITRAP LEBT section, thus in parallel we were able to test it prior

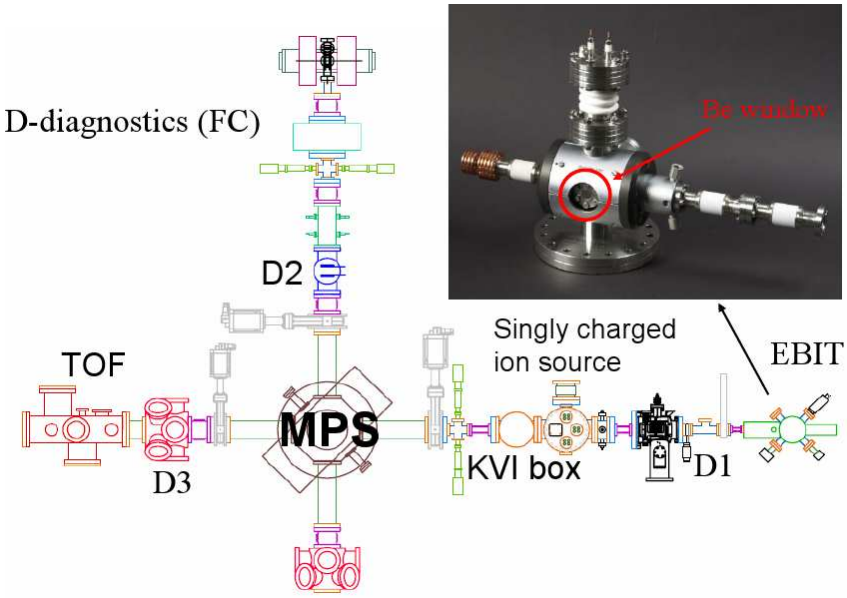

Figure 6.7: SPARC EBIT setup at GSI, AutoCad drawing and photo. In comparison to the MAXEBIS setup additional ion optical elements were included into the beam line with an advanced tool for profile measurements, i.e. KVI diagnostics with MCP-phosphor screen combination. On the photo one can see the ion source itself with a Be window which allowed X-rays measurements of the processes in the ionization region.

to the installation into the HITRAP beam line. The ion source was a Dresden type EBIT [DREEBIT] with an electron gun capable to produce currents up to 50 mA. The electron beam was radially focused in the 1.5 cm long ionization chamber via a couple of room temperature permanent magnets, providing 0.25 T field in the trap region. The electron beam diameter can be estimated using 3 different methods:

a) from the formula 5.10 in the 5th chapter, knowing the magnetic field in the chamber, the cathode temperature and the cathode radius

b) from the formula 5.2 in the 5th chapter, knowing different charge state ionization cross sections (e.g. eq. 5.5), electron current and analyzing the charge states abundances for different confinement times

c) from simulations.

We used the 3^{rd} method and estimated the radius to be $0.1mm$, thus the electron current density was approximately $100A/cm^2$ for 5 keV electron energy and 20 mA current, normally used for the operation. The electron beam under the mentioned conditions provide 25 V deep radial potential well (equations 5.11, 5.12). Due to the low magnetic field in the source the ions are mainly confined via electrostatic potentials.

More advanced ion optical simulations were performed for the setup. The electron space charge potential was included into the SIMION's EBIT instance

to treat the potential profile more realistic. The potential pattern was introduced using C++ programming. On fig. 6.8 one can see potential profiles of the EBIT, note, that there is a "gate way" or a cavity formed by the electron string in the barrier electrode potential. The middle electrode potential is also lowered with the electron space charge.

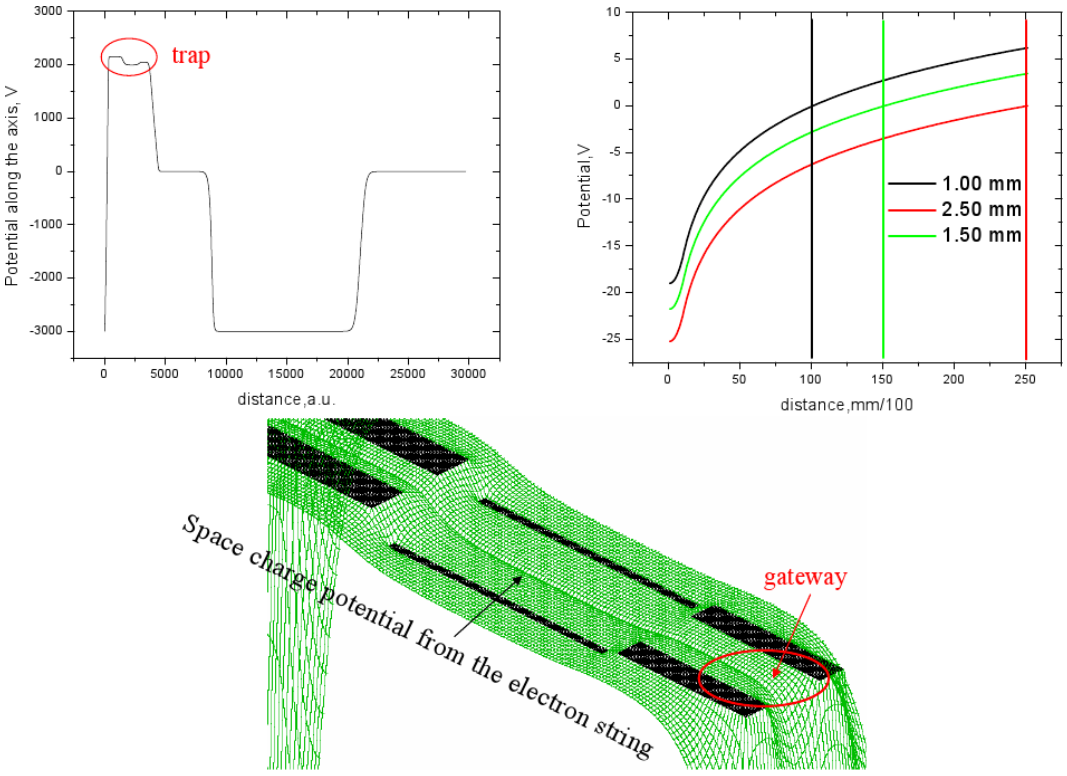

Figure 6.8: Simulations of the SPARC EBIT potentials. Top, left is the potential profile along the EBIT axis with the marked trap region, the negative potential to the left is the cathode potential and to the right, the collector electrode potential. Top, right are the radial potential distributions created with the electron space charge for different drift tube radii. At the bottom is the final 2D potential pattern in the trap.

6.2.2 Emittance measurements

Emittance measurements were made using a multi-gradient method (see Appendix C), the same way as it was done for the beam from the MAXEBIS. The ion beam hit the MCP-phosphor screen combination in KVI diagnostics box, producing a light spot detected with a digital camera. The camera was triggered with a TTL level pulse synchronized to the ion extraction pulse. The light intensity distribution from the image of the spot was projected on x or y axis (see fig. 6.9, left). The spot size was changed applying different potentials

to the Einzel lens in front of the diagnostics. Focal length for the set potential was estimated from simulations (see fig. 6.9, right). Information on the spot radii and focal lengths is enough for emittance calculations.

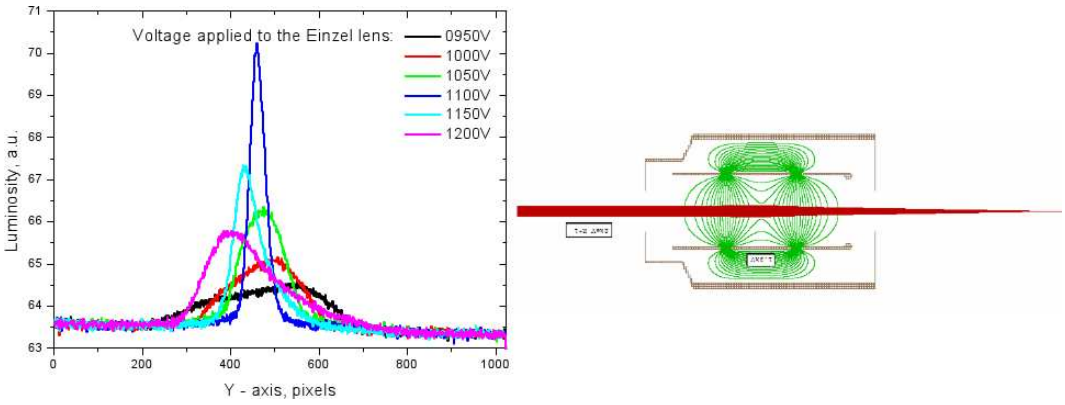

Figure 6.9: Beam profiles of the 2 keV/q Ar beam under different potentials applied to the Einzel lens in front of the diagnostics, left. Simulation of the lens using SIMION 7.0 to obtain the focal legths for the used potentials, right.

Different dependences of the emittance were measured: on the ionization chamber potential, which determines the velocities of the ions, on different charge bred elements and on electron beam currents. The most reliable measurements were done for different currents with fixed potentials. One can see the dependence of the Ar beam[1] emittance on the electron current in fig. 6.10. As the electron beam intensity increases, the emittance increases as well. This

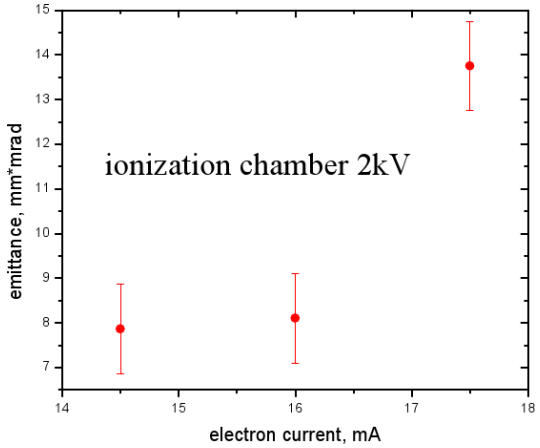

Figure 6.10: Ar 2 keV/q ion beam emittance in dependence on the electron current.

can be caused by two possible reasons. The first is the increase of the electron

[1]Here and further on in this chapter, if not specially mentioned, the ion beam from the ionization chamber are Ar ions. The Ar is provided by gas injection.

beam radius, caused by the higher cathode heating power and thus higher electron temperature. Bigger electron beam diameter means that the ions are created in a larger volume, thus the diameter of the extracted beam also expands. Another reason can be due to the electron heating in case the diameter is kept the same. According to Landau-Spitzer formula the increase of the ions temperature, and thus velocity distribution, is proportional to the electron current density. In principle both reasons can contribute at the same time to the increase of the emittance.

6.2.3 Extraction pulse measurements

To improve the beam quality decreasing the electron current is not applicable, because the charge capacity of the trap should be linearly dependent on it (see eq. 5.6). To approve the linear dependence of the number of charges stored in the trap on the electron current, the extraction pulses were also measured, using FEMTO amplifier, which is also a current to voltage converter. In fig. 6.11, left one can see a dependence of the extraction pulse on the electron current for 50 ms of confinement, when the trap is not completele filled and charge evolution is on-going. For smaller currents one can see that different charge states are resolved better due to a smaller energy distribution of the ions in a shallower trap. Increasing the current increase the depth of the potential well and heating of the ion cloud making energy distribution broader and charge states less resolved. The production of HCI is also increased after 50 ms of confinement for more intense electron beams, seen as an increase of the pulse on the shorter time-of-flight side of the spectrum. As the charge evolution is strongly dependent on the current density, but not on the current itself one can conclude that the density increases with the current as well.

The comparison of the charges per pulse measured after 500 ms of confinement, which is even longer than the time necessary to saturate the trap capacity, with the calculated values via the formula 5.6 can be seen on fig. 6.11, right. At low electron beam currents the potential well is quite shallow and can not efficiently capture the ions, while at higher currents the electron density increases, probably increasing simultaneously temperature and loss rates. In between these two critical regimes, it seems that one can obtain number of ion charges closer to the compensation limit.

Note that every charge state contributing to the total pulse from the trap has an asymmetrical shape of its own pulse, with a peak and a tail towards longer time-of-flight. Such a structure was also seen in simulations. The fastest part, as for the MAXEBIS, is found to come from the trap region close to the extraction barrier electrode and the tail is due to the ions away from the exit, slowly drifting towards the extraction electrode. The simulated ion pulse from the EBIT one can see on the insertion in fig. 6.11, left.

Pulse investigation can provide a nice information on the charge breeding process. In fig. 6.12, left, a change of the extraction pulse in dependence on the

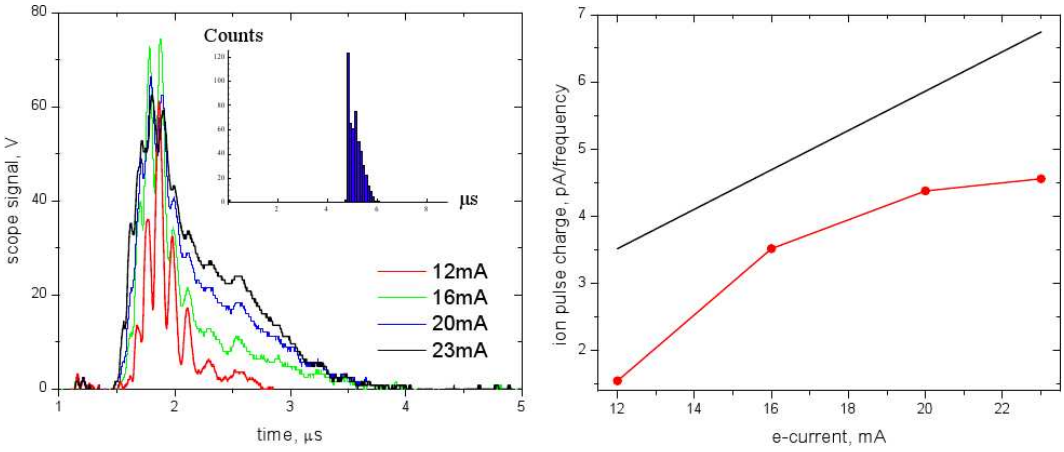

Figure 6.11: Ar 4.8 keV/q ion beam extraction pulses for 50 ms of confinement and different electron currents, left. The dependence of the total extracted ion charge (red line) per pulse after 500 ms of confinement and the trap capacity from eq. 5.6 (black line), right.

confinement time can be seen. Higher charge states have shorter time-of-flight. There is an increase of the high energy part of the pulse related to the HCI for longer confinement times and a decrease of the low energy part, related to the lowly and multiply charged species. The amplitude and the area of the pulse, proportional to the number of the charges in the trap, are increasing with increasing of the confinement time, but reach a saturation point after approximately 0.5 s. This corresponds to the point when reaching the trap capacity. Note that the trap is very quickly filled within 20 ms (fig. 6.12, right) with lowly charged residual gas and Ar ions ions and after that slowly increase the number of Ar charges during 500ms when the full capacity is finally reached. This slow filling happens due to the higher charge states of Ar which are better confined in the trap. One can compare the rate of electron space charge compensation for the room temperature EBIT and for the cryogenic MAXEBIS, where within 25 ms only a quarter of the capacity is reached (fig. 6.6).

6.2.4 Charge state spectra

Increase of the charge state in the EBIT for longer confinement can be more clearly seen with magnetic scans or TOF spectra. One example of a magnet scan is shown in fig. 6.13. Here the charge state evolution starts with a mixture of the residual gas and lowly charged Ar ions, which increase their charge states and become better confined in the trap. When the trap is already partially filled with ions, the electron space charge, providing the potential well, is screened and high temperature ions can escape radially, as the magnetic field is small (not in case of the MAXEBIS setup). Ar is heavier than the most

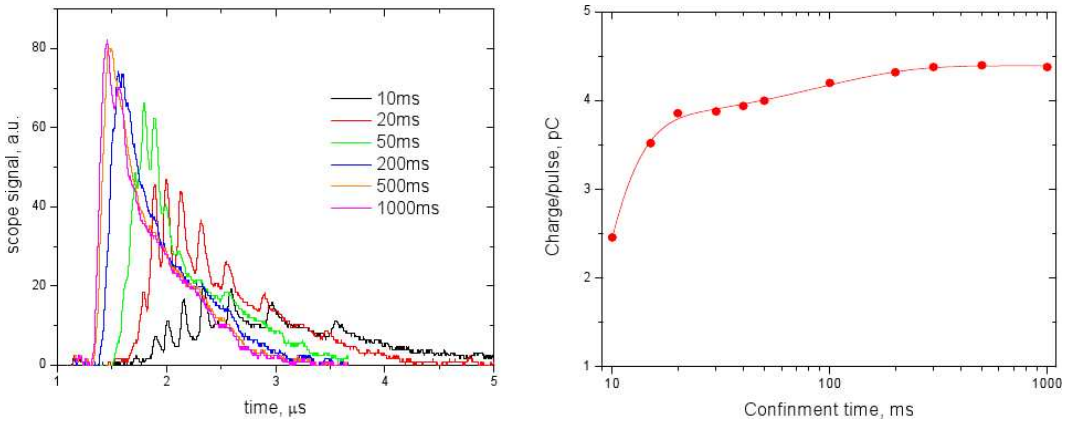

Figure 6.12: *Ar* 4.8 *keV/q* ion beam extraction pulses for different confinement times, left. With decrease of confinement time also decreases the high energy part of the pulse correspondent to the HCI and increases the slower part, related to the lowly and multiply charged species. The total charge per pulse in dependence on the confinement time, right. The trap is quickly filled within 20 ms with low charges, but the charge capacity is reached after approximately 500 ms

abundant elements in the atmosphere and forces out the light residual gas ions from the trap via ion - ion collisions. The residual gas ions completely disappear from the spectra for longer confinement. Further increase of the charge breeding time strips further the electron shells of the ions remained in the trap. As the electron charge is nearly completely screened after 0.5 s by highly and multiply charged Ar-ions, the trap does not accept a lot of singly charged ions anymore, which could be stripped further and multiply charged states sequentially disappear from the spectra. After the 1000 ms the equilibrium starts, so the abundance of different charge species does not change anylonger. Due to the compensation, the processes of the ionization, electron capture from the surrounding neutral gas as well as from the electron beam and the ion escape from the trap cancel out. The ion temperature is kept constant due to the compensation of the electron heating with ion Coulomb cooling. The *Ar* and residual gas singly charged ions are still produced in the electron beam, though not a lot of them are captured, Coulomb collisions of HCI in the trap with these ions decrease the ion plasma temperature. Those ions which are captured pass the whole ionization process to higher species with big losses on there way and contribute to the less highly charged part of the spectrum.librium starts, so the abundance of different charge species does not change anylonger. Due to the compensation, the processes of the ionization, electron capture from the surrounding neutral gas as well as from the electron beam and the ion escape from the trap cancel out. The ion temperature is kept constant due to the compensation of the electron heating with ion Coulomb cooling. The *Ar* and residual gas singly charged ions are still produced in the electron beam, though not a lot of them are captured, Coulomb collisions of

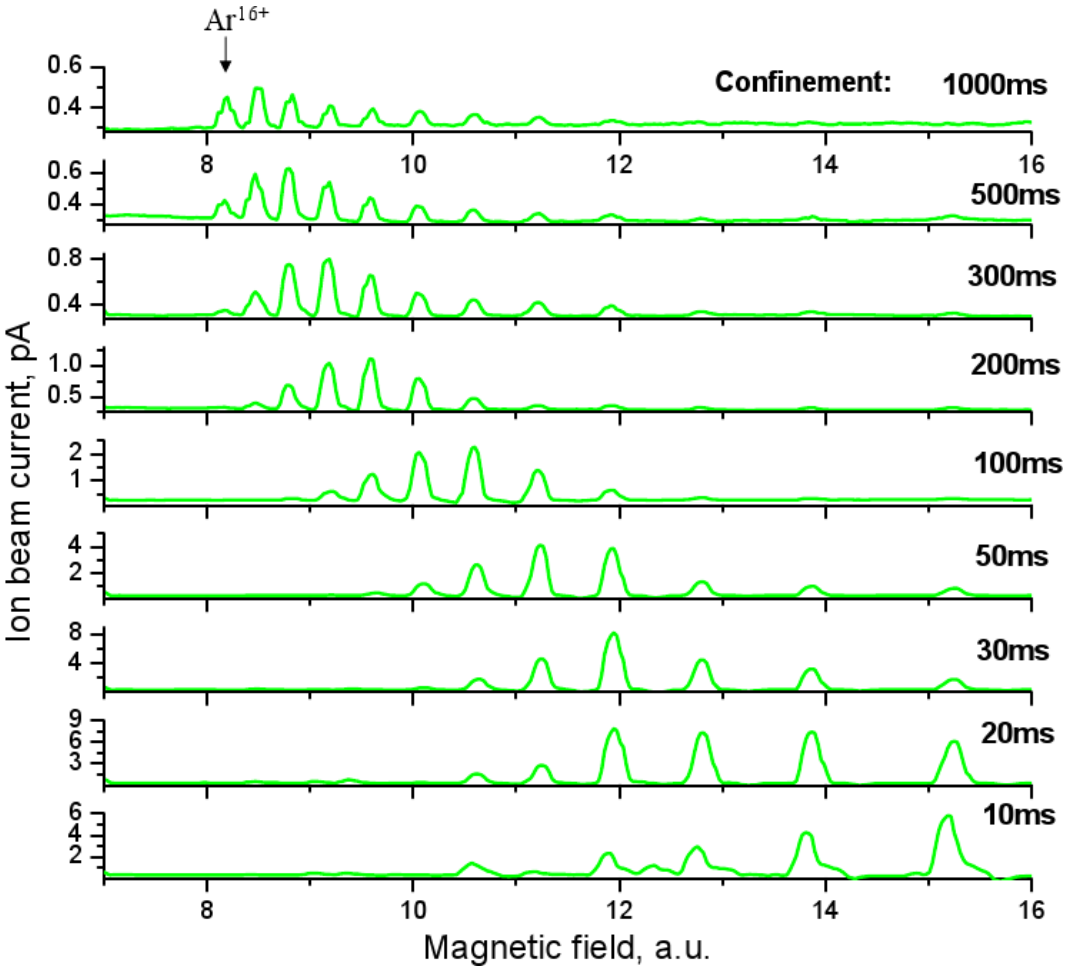

Figure 6.13: *Ar* 4.8 keV/q ion beam magnetic scans for different confinement times. The abundance of higher charge states increases with increasing of the confinement time.

HCI in the trap with these ions decrease the ion plasma temperature. Those ions which are captured pass the whole ionization process to higher species with big losses on there way and contribute to the less highly charged part of the spectrum.

The equilibrium and stop of the charge evolution can be seen from time-of-flight spectra on fig. 6.14 for long confinement times.

As it was shown the electron beam compensation is followed by the equilibrium of the plasma. The faster filling of the trap can be provided with a higher gas pressure in the ionization chamber, though at the same moment the equilibrium also starts earlier, meaning a shift in abundances towards the multiply charged ions, due to the more intense rates of the electron capture and influx of low charge species. To increase the production of higher ion charge states one should play with the mentioned processes of ionization, elec-

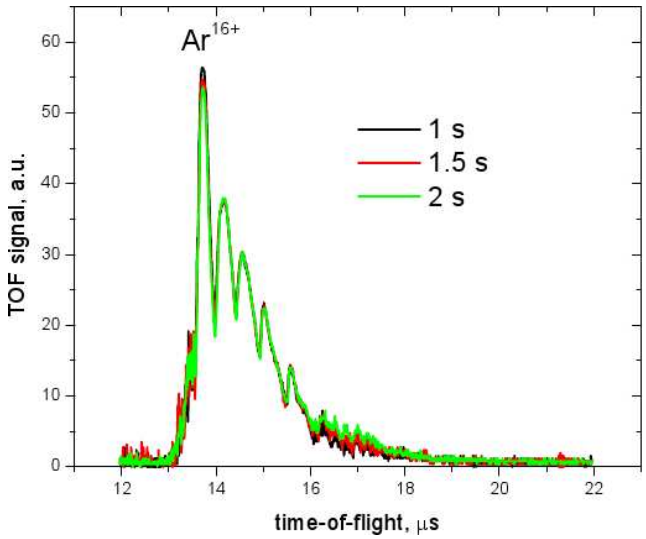

Figure 6.14: *Ar* 2 keV/q ion beam TOF spectra for long confinement times. The equilibrium of the plasma is already reached and the charge evolution does not happen anymore.

tron capture and ion escape. To obtain the maximum ionization the electron beam energy should be adjusted to the maximal cross section. Another way to increase the ionization probability is to use higher electron density, which unfortunately also increase the heating rate, biggest for the HCI, leading to the ion losses from the trap. Also higher density increases the rate of radiative recombination. Very necessary in production of highly charged ions is to decrease the pressure in the chamber as low as possible[1], though it increases the time required to fill in the trap and thus lower repetition rate of the extracted pulse.

In fig. 6.15 one can see the charge evolution for different confinemet times and pressures. Even within a short confinement time the production of higher ion charge states is already more efficient for lower gas pressure, though the number of charges in the trap is higher for the higher pressure due to the more rapid filling. After a long charge breeding of the ions in the trap, distribution of the charge species is still broad for high pressure, while for the low pressure the total charge is concentrated mainly in two highly charged states. The light fraction of Ar^{17+} also appeared in the spectra but was not enhanced due to the low production rate. The achieved charge evolution at low pressure was close to the ideal case of pulsed injection, when the amount of ions in a higher charge state is pumped via the electron impact ionization of the lower charge states.

On fig. 6.16 one can see a comparison of the experimentally obtained rela-

[1]Here one should be careful, because too low pressure will lead to the decrease of the ion Coulomb cooling in the trap.

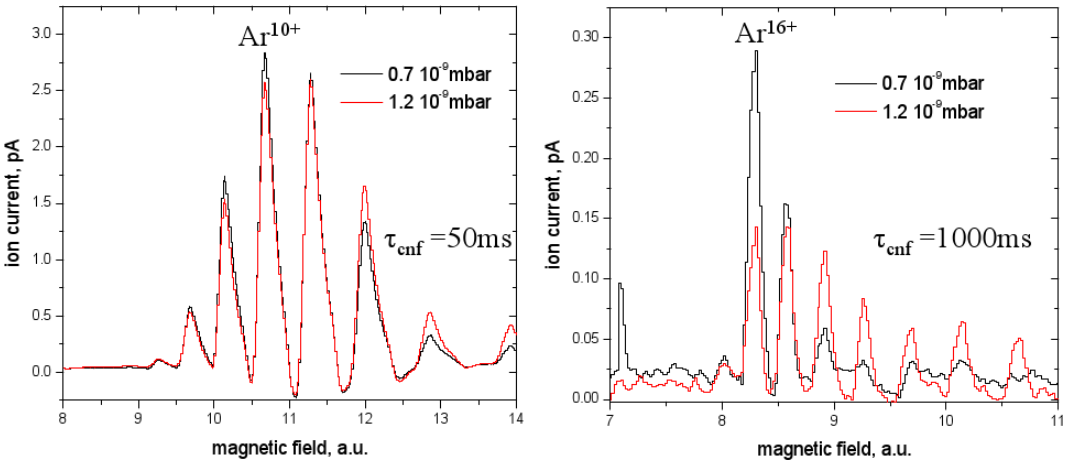

Figure 6.15: Ar 4.8 keV/q ion beam magnetic scans for confinement times: 50 ms, left and 1000 ms, right, in dependence on the Ar gas pressure in the EBIT. Electron beam energy is 7.4 keV.

tive numbers of different ion species and simulated abundances, using CBSIM code. In the program the influx of neutral Ar atoms was disregarded meaning a pulsed injection of atoms into the trap. Though quantitatively the dependences are a bit different, qualitative picture is pretty close. So the ion charge state distribution manipulation is possible and one can obtain the maximum amount of charges in a certain charge state, here Ar^{16+}!

Everything described above except of the dependence on the electron current was mostly dedicated to the efficient production of highly charged ions. Improvement of the beam quality can be also possible. The emittance of the beam, as it was already mentioned, is determined by the ion temperature in the trap and the beam size.

The ion beam size can be made smaller, decreasing the electron string radius which is possible by increasing the magnetic field. Magnetic field also increase the effective potential felt by the ions, thus increasing the maximal energy at which the ion is still confined, leading to the increase of the ion cloud temperature. Smaller electron string radius also means higher density and heating of the ions in the trap.

Decrease of the ion temperature in the source can be done limiting the highest energy in the source. The high energy can be cut off by lowering the potential well depth. The radial potential can be decreased only decreasing the electron linear density according to the formula 5.12. As the number of ion charges in the trap is dependent on the electron linear density, this parameter should not be touched to have an intense beam. Still there is one degree of freedom left for potential manipulation, i.e. in longitudinal direction, varying the barrier trapping potential. In fig. 6.17 one can see the time-of-flight spectra of the charge bred Ar ions for different volages applied to the extraction barrier

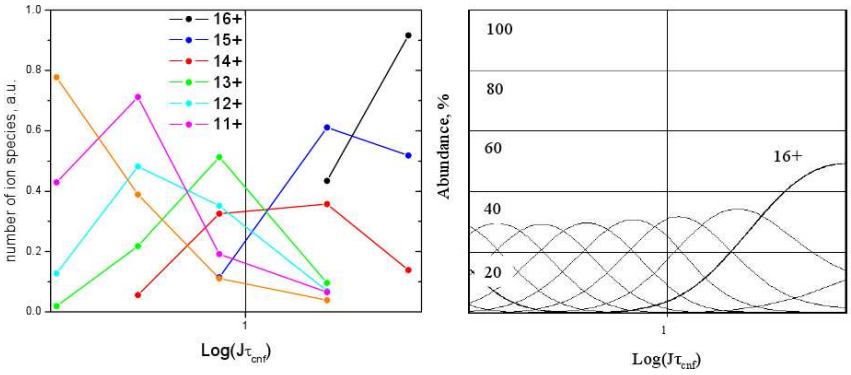

Figure 6.16: Dependence of the *Ar* ion charge states abundance on the confinement time at low pressure, left and simulation using CBSIM code, right. The parameters included into the simulation were the same as in the experiment, the only difference was that the influx of the neutral gas in the CBSIM was switched off, meaning a pulsed injection.

electrode.

The lines of different charge states become more narrow with decreasing of the barrier potential due to the lower energy cut off, and thus lower temperature of ions in the trap. Unfortunately lower voltage also limits the effective trapping volume, hence decreasing the number of ions. Still the highly charged species which have better confinement are in relatively big amount kept inside the trap. So the ion beam emittance can be also manipulated by varying few parameters!

6.2.5 X-ray spectra

In addition to this chapter I would like to mention that the X-rays spectroscopy also provides a good information on the charge breeding process in the trap, though in our case of rather low resolution X-ray spectrometer the data was not that extensively used and we were mostly interested in the extracted ions investigated with the TOF spectrometer and magnetic separator. Still the information obtained from the X-ray spectra is also reliable and representative. As an example one can see a dependence of X-ray spectra on *Ar* pressure in the chamber in fig. 6.18, left for long confinement time. In this case the production of HCI is rather high. Increase of the *Ar* gas pressure decreases highly charged ions production, seen as a decrease of K_α and K_β line intensities. The production rate for higher pressures is lower mostly because of the higher electron capture rate already at multiply charged states. On the insertion of the same plot one can see the part of the spectra (with different scale) above the Bremsstrahlung background. In this part, radiative recombination (RR) lines can be seen for the capture into the K and L shells. To have this lines in the spectra the ions should be stripped down to the correspondent electron

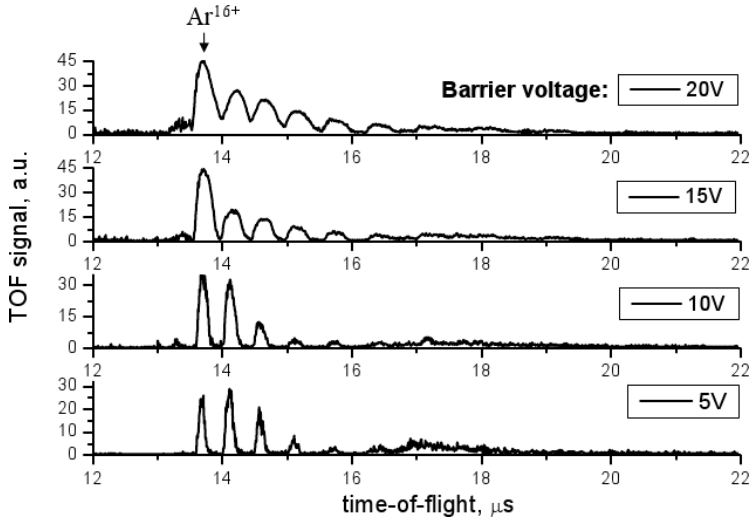

Figure 6.17: *Ar* 2 *keV/q* ion beam TOF spectra with different potentials applied to the barrier electrode. One can see thinning of the spectral lines which comes from a narrower velocity distribution.

shell, otherwise in case of a vacancy appearence it is immediately filled with an electron from an upper shell, but not from the electron beam. The RR lines shift to higher energies with decrease of the number of electrons in a chosen shell, into which the capture occurs. For the small pressure (red line) one can see this shift both for $n = 1$ and $n = 2$ lines. Also for smaller pressure an increase of the radiative recombination into the K shell can be seen, meaninig higher production rate of Ar^{17+} and Ar^{18+} ions.

In fig. 6.18, right, the X-ray spectra are plotted for two different, relatively short confinement times. On the insertion one can see that the RR lines related to the HCI are almost absent for the short confinement. The K_β line for 100 ms of charge breeding also dissappears from the X-ray spectrum. This happens because of the following reason. In case of a vacancy creation in the K-shell it can be filled with an electron from the 3p subshell with higher probability if the 2p subshell is empty. The lack of the 2p electrons means that there should be a production of the Ar^{14+} in the trap, which is nearly absent for 100ms of confinement even at lower pressure (see fig. 6.13), that leads to the absence of the K_β line in the spectrum. The Ar^{14+} created in a significant amount during 500 ms fill in the 3p subshell via the electron capture from surrounding neutral atoms. Relaxation of the 1s3p excited states leads to the K_β line in the spectrum for 500 ms of confinement. So X-ray spectroscopy is a nice tool to investigate the charge breeding in the trap. For very long confinement times it can be a fast indication of a certain process.

In this chapter different aspects of the charge states abundance evolution were discussed. This knowledge can improve the HCI production efficiency as well as the beam quality. Our experimental results show that the emittance

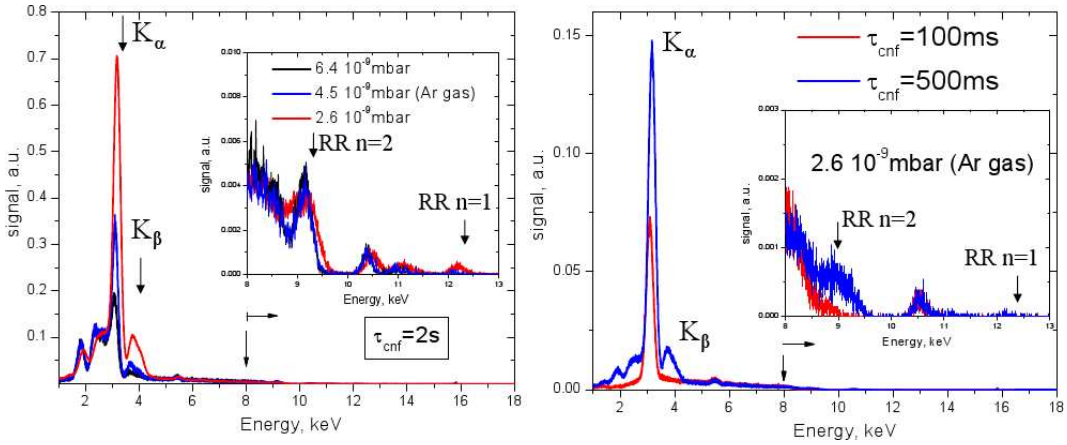

Figure 6.18: *Ar* ions X-ray spectra for 2 s of confinement time, 8 keV electron beam in dependence on *Ar* gas pressure in the ionization chamber, left. X-rays for 100 ms and 500 ms of confinement at fixed pressure, right.

of the beam and charge state manipulations are really possible in the EBIT varying different parameters. Still in this chapter only the charge breeding of the *Ar* gas was covered, knowledge about which can be applied to other gaseous materials. The next chapter is dedicated to the charge breeding of externally injected singly charged ions.

Chapter 7

Charge Breeding of externally injected singly charged ions

7.1 Motivation

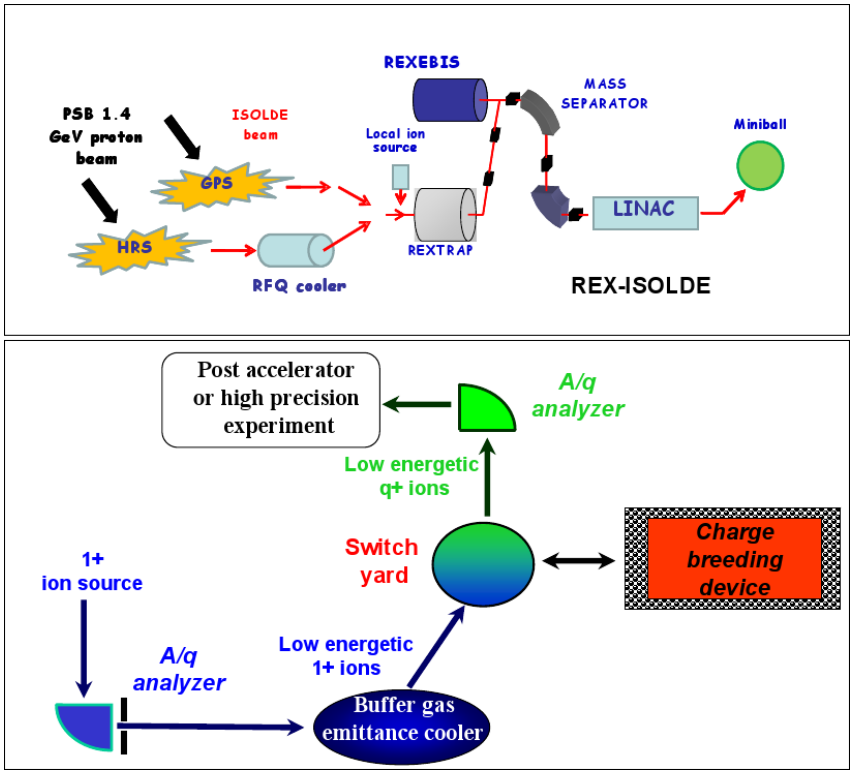

Figure 7.1: REX-ISOLDE facility, top, and EURISOL project, bottom. The schematic view of the future EURISOL facility is more general and comprises main elements of the beam line for post-acceleration and precision experiments with highly charged ions of rare isotopes. The ions are at first mass selected, then prepared and injected into a charge breeder, extracted and charge selected afterwards.

The EBIS/T and ECRIS devices, as it was mentioned, are typically used to produce highly charged ions of all gaseous materials injected into the trap region, where atoms are stripped of electrons via the electron impact ionization. The construction also allows to install evaporative sources of different materials in the vicinity of the ionization chamber to inject various (mostly metallic) elements into the trap region. Still the number of materials produced in highly charged states by the sources is rather limited.

The demand of HCI of stable and especially exotic isotopes has driven the development of charge breeding methods. Existing facilities such as REX-ISOLDE/CERN (fig. 7.1, top) or ISAC/TRIUMF are already using a charge state booster. Planned facilities such as SPIRAL II, MATS, EURISOL (fig. 7.1, bottom) and CARIBU will include charge breeding devices in future. Therefore, exploration and optimization of existing charge breeders is necessary and was supported by the I3-EURONS project.

The radioactive isotopes at ISOLDE are produced in thick high-temperature targets via spallation, fission or fragmentation reactions, when a high energy (1.4 GeV) proton beam from the Proton-Synchrotron Booster (PSB) impinge on a target. The big variety of isotopes are extracted from the bulk of the target towards different experiments. In the facility the extracted ions of isotopes are singly charged. To increase the charge state of a chosen isotope after A/q separator the ions are prepared at first in a cooler and injected into the charge breeder, in case of the REX-ISOLDE - REX-EBIS. Different charge states from the charge breeder are extracted, separated and sent further into the beam line.

For example for future CARIBU project [Sav08] a gas catcher will be used to stop fission recoils from a Californium source and to extract them as a low-energy beam. In this case the isotopes from the gas catcher will be also of singly charged ions. ECR-1 ion source will be used for the CARIBU project as a charge breeder.

Highly charged ions of different rare isotopes are of special interest for atomic physics precision experiments at low energy, like laser spectroscopy or mass measurements. Low A/q of HCI also allows efficient post-acceleration of the radioactive ion beams in an IH-structure and RFQ for nuclear physics experiments at the Coulomb barrier.

As the EBIS/T devices seem to be very efficient for capture of externally injected singly charged ions to produce HCI, there application for the charge breeding is the most promising. The singly charged ions can be injected into a source continuously or in a pulsed regime (see below). In case the ions are bunched before the injection, both injection schemes should not lead to big losses. Investigation of the EBIS/T devices possibilities is covered in this chapter.

The production of rare isotopes is not very intense in comparison to stable beam generation. Thus to keep the number of HCI more or less close to the number of injected ions, the singly charged species should be efficiently

captured in the charge breeder and ionized to a narrow charge-state distribution with the most abundant the required charge state. The extracted highly charged ion beam should have small emittance to prevent losses in the beam line. Ion charge state distribution manipulation in the source and improvement of the extracted beam quality were discussed in the previous chapter. Here we will concentrate mainly on the capture of singly charged species and overlap between the ion beam and the electron beam.

In our experiments the charge breeders used are the MAXEBIS and the SPARC EBIT. Singly charged ions were produced with the also mentioned in the 5th chapter sputter ion gun and surface ion source.

7.2 Basics of charge breeding

There are two main possibilities for external injection of singly charged species into the EBIS/T device, schematically shown on fig. 7.2. Singly charged ions

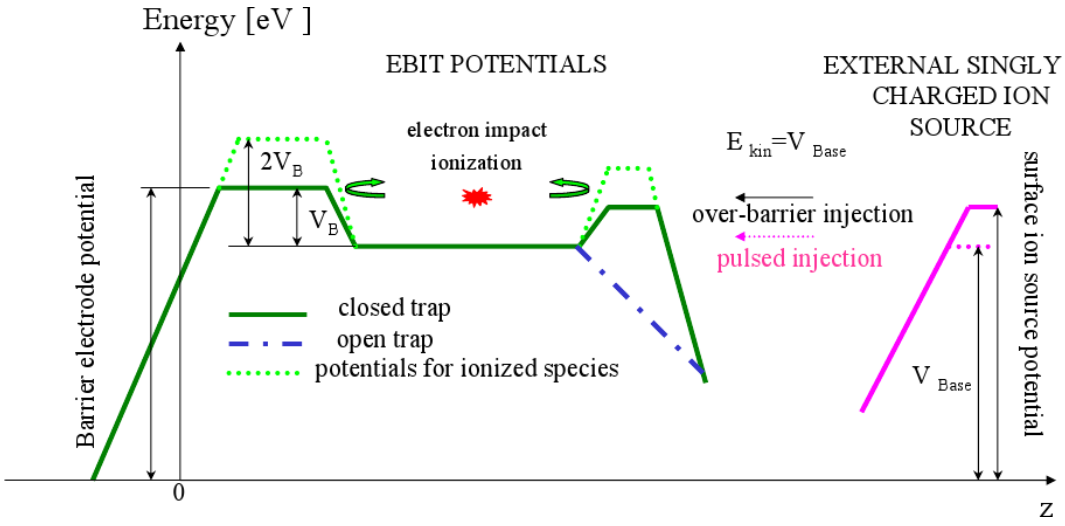

Figure 7.2: Scheme of the potentials for external singly charged ions injection into the EBIS/T for charge breeding.

are usually extracted from a source biased to a potential V_{Base} which determines there kinetic energy on the way to the EBIT/S device. To be captured in the charge breeder the energy should be above the ionization chamber potential allowing two possibilities: below the extraction barrier potential, distinguishing a pulsed injection into the device, or above, corresponding to the over-barrier injection. The barrier electrode close to the cathode (the first drift tube) should have the potential always above the singly charged ion energy to reflect the beam backwards. This prevents the ions from leaving the trap towards the cathode. In case of the pulsed injection the extraction barrier voltage is dropped during the time necessary for the ions to drift from the

extraction electrode to the first drift tube and backwards, then the potential is increased and the ions are confined longitudinally within the electrostatic potential well created by the barrier electrode potentials, and radially in the magnetic field and electron space charge potential [Kes08b].

The ions created via the electron impact ionization of gas atoms are born and confined inside the electron string initially and thus increase further there charge state. In the case of external injection the ions can be confined but not charge bred, moving around the electron beam, thus the key role of charge breeding is to provide the overlap between the ion and electron beams. In case of the over-barrier injection the better overlap is even more critical, because the extraction barrier potential is kept high and constant during the injection. The ions for this charge breeding scheme can be trapped only if they change there charge at least to 2+ state, then the extraction barrier V_B becomes twice higher (see fig. 7.2) and the ions are trapped. If the charge state is not changed during the drift time inside the ionization chamber, then the ions just leave the trap region the same way as they entered. Increase of the charge state increases the potential barrier also in radial direction and the ions become better confined and there motion becomes closer to the bottom of the potential well and thus better overlap with the electron beam is provided.

One can conclude that for the efficient charge breeding the emittance of the injected ion beam should be less or comparable to the emittance of the ions from the source itself (see [Wen02] for estimations), also a strong magnetic field is favorable[1], which can provide radial focusing and longer drift time. To increase the time the ions are contained in the ionization region for the over-barrier injection the length of the trap should be also sufficiently long, which depends on the ion velocity in the trap, electron current density and as mentioned the overlap between the two beams. The over-barrier injection despite of the more strict requirements set on the beam quality has a big advantage that the trapped ions can be continuously accumulated in the ionization region during much longer time in comparison to the pulsed injection. In this chapter only over-barrier (called accu-mode) injection is considered, which is the anticipated injection scheme of the MSU ReA3 charge state breeder [Sch08].

7.3 Advanced charge breeding in MAXEBIS

The MAXEBIS was an essential tool of the charge breeding collaboration [Kes08a]. This device had several advantages. As it was mentioned in the setup description, there was a possibility to change the electron beam radius changing the position of the cathode in the magnetic field gradient using manipulators. So a bigger radius of the electron beam could be achieved in a strong magnetic field providing automatically a good overlap between the injected ion beam

[1]Though, one should not forget, that strong magnetic field focuses better the electron beam as well.

and electron string. The residual gas ions produced relatively plentifully in the source could serve as a Coulomb target, collisions with which in case of the heavier incident species, could decelerate and cool the injected beam.

With the MAXEBIS the injection over the barrier of singly charged Ar - ions from the sputter gun, has been tried. To perform these experiments, the setup shown on fig. 6.1 was used and the TOF mirror high voltage was ramped up and down with a Behlke high voltage switch driven by a TTL level pulse synchronized with an extraction pulse from the EBIS. So during extraction from the source the mirror of the spectrometer reflected the highly charged ions from the EBIS towards the channeltron and singly charged species from the sputter gun backwards not allowing there injection into the MAXEBIS. During our successful experiment the potential of the ionization region was adjusted to 1.5 kV, the extraction barrier potential to 1.8 kV, the first drift tube potential to 2 kV and the potential of the sputter ion gun was 1.8 kV. A beam current of 100 pA of singly charged Ar-ions, which delivered 100 nA primary beam intensity, could be measured on the repeller in the collector while the electron beam was switched off. Taking into account the aperture of the repeller and the area of the electrode itself seen by the ion beam and assuming focusing of the beam and homogenious distribution of the particles one can estimate that nearly the same amount of ions entered the MAXEBIS device.

The corresponding TOF spectra with and without Ar^+ injection are shown in fig. 7.3. With Ar^+ injection several peaks showed up with maximum abun-

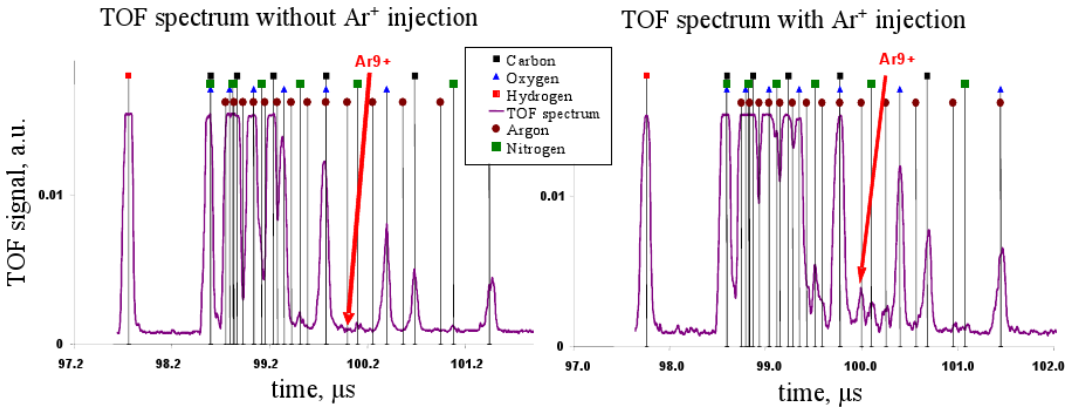

Figure 7.3: TOF spectra of the ions extracted from the MAXEBIS with and without external Ar^+ injection (confinement time 25 ms).

dance of the Ar^{9+} species. The electron beam current was 30 mA, the beam energy 3 keV and the trap length 0.8 m, thus the charge capacity of the electron beam was $\approx 4.6 \cdot 10^9$ charges and the measured electron beam neutralization after 25 ms was 25% (see fig. 6.6). $1.6 \cdot 10^7$ Ar^+ ions entered the electron beam in 25 ms. Injection and breeding efficiency can be estimated from the relative abundance of Ar peaks in the TOF spectra on which residual gas ion peaks are

not cut by the scope resolution. The amount of Ar-ion charges as compared to the amount of residual gas ions, derived from the spectra, is around 12%. Assuming an average charge state of 10+, $1.4 \cdot 10^7$ Ar^+ ions were captured and charge bred, meaning 86% of the injected singly charged species, 20% of them were bred to the 9+ charge state. So capture and charge breeding were very effecient. One can conclude, that the ideas, to use a small amount of the residual gas ions as a Coulomb target for externally injected Ar^+ beam and to use relatively big diameter of the electron beam to improve the charge breeding efficiency, were approved. Typically for such big ion sources with a superconducting magnet the efficiency of the charge breeding is around few percents.

Main uncertainties of our experiment come from the estimation of the Ar^+ current entering the electron beam at the repeller electrode and hence a larger amount of Ar ions could be injected into the ionization chamber. Unfortunately the uncertainties and bad resolution of the time-of-flight spectra can spoil the obtained value for the efficiency. Also a bad transmission of the beam line decreased drastically the overal setup capability for the delivery of highly charged ions.

7.4 Charge breeding in the room temperature EBITs

In the electron beam ion sources with a strong magnetic field the capture of externally injected ions in accu-mode is not a big deal and one should mostly take care of the overlap between the electron and ion beams for further ionization. In the ion sources with relatively weak permanent magnets like the SPARC EBIT the capture and overlap are going hand in hand, because the weak magnetic field can not capture the singly charged ion species. The ions become confined in such a source with electrostatic fields. This can happen only if they change their charge state.

The small size of the EBIT means a short drift length of the ions inside the trap. For the discussed over-barrier injection, the time necessary to make a round trip in the ionization region is around a μs, dependent on the difference between the potentials of the ionization chamber and singly charged ion source, which determines ion velocity in the trap.

The ionization time necessary to obtain the 2+ charge state in the electron beam is dependent on the ionization potential of the second electron, on the electron beam energy and density, but still normally is below $1\mu s$. Nevertheless on the scale of the total drift time inside the trap the ion beam must be within the electron beam for a considerable period.

First attempts for the charge breeding with the SPARC EBIT was performed with a setup in a separate experimental hall and depicted on fig. 6.7. Unfortunately the experiment did not give us a satisfactory result. The ab-

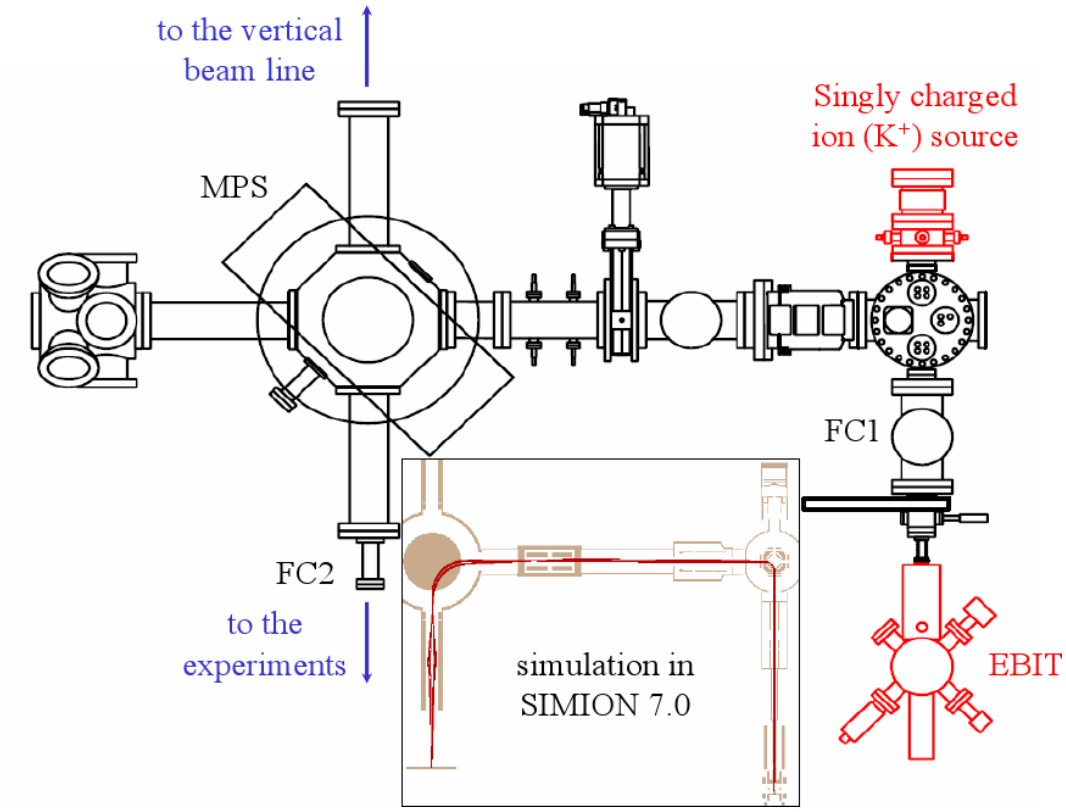

Figure 7.4: A new setup installed on the HITRAP platform. The singly charged ion source produced K^+ ions which were injected into the EBIT and after charge breeding extracted towards the MPS. On the insertion one can see a SIMION 7.0 simulation of the beam line with the trajectories of Ar^{10+} ions (red lines) extracted from the SPARC EBIT.

sence of a proper alignment did require a lot of steerers used to transport the beam to the source. This most probably led to the off-axis injection of the ion beam.

As the SPARC EBIT is a test ion source for the HITRAP project, the new setup was built on the first floor above the decelerator facility after the vertical beam line, see fig. 7.4. The setup except of the task to deliver HCI from the EBIT for off-line tests, was also designed to perform the charge breeding experiments. The singly charged ion source (this time a surface ion source) is mounted opposite to the EBIT, between the two sources a quadrupole bender is installed to bend the beam from the EBIT towards the MPS for charge state analysis. This is done as usually applying high voltage to the quadrupole electrodes during the extraction from the EBIT with a Behlke high voltage pulsers. Except of the short extraction time the high voltage is not applied, allowing singly charged ions from the surface ion source to enter the EBIT. In front of the EBIT a FC1 for diagnostics and a couple of additional Einzel

lenses were forseen for the better transport.

The whole setup was simulated as usually using SIMION 7.0 to check the beam transport (see the insertion on fig. 7.4). Additional simulations were carried out for the external injection of the singly charged ion beam into the source. In the simulation a user programming was used and the ions obtained a 2+ charge state as soon as they crossed the virtual electron beam. On fig. 7.5 one can see the trajectories of singly charged potassium ions (red lines) and K^{2+} species (blue lines) for different "over"-barrier injection potentials. The most efficient injection happens in the simulation when the ion kinetic

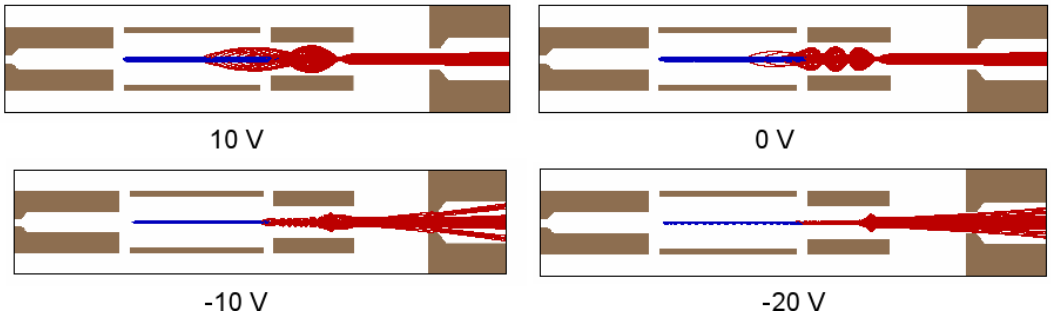

Figure 7.5: Simulation of the injected K^{+} ion beam (red lines) into the EBIT for different starting potentials of the singly charged ions, 10 V above the extraction barrier, equal (0 V) and -10 V and -20 V below the barrier potential. Blue lines correspond to the K^{2+} ion trajectories continuing the motion of singly charged species as soon as they pass through a virtual electron beam. Doubly charged ions are immediately trapped in the ionization chamber.

energies are slightly above the extraction electrode potential. That was one of the main mistakes done by us during the experiments with a previous setup. One should keep in mind that the ionization in the simulation is done during a single time step when the singly charged ion crosses the small volume occupied by the electron beam. That's why the injection slightly above the barrier and capture were the best, still the simulation shows that the overlap with the electron beam is not very good. On the other hand injecting the ions right into the barrier, into a potential cavity (gate way) created by an electron string (see fig. 6.8) the overlapping conditions between the ion and the electron beams are automatically fulfilled.

Also in reality the potential dip at the exit is not screened by the ions like in the trap region due to a continuous escape of the positively charged species and thus at the exit or entrance for the upcoming ions it effectively confines radially the externally injected ion beam. Of course a special preparation of the upcoming ion beam is necessary to have a small emittance[1] which will not allow a reflection of a big fraction of ions from the barrier.

[1]Better emittance one can get via electron or resistive cooling of ions or in case of an intense beam just cutting it passing through diaphragm(s) before injection into the EBIT.

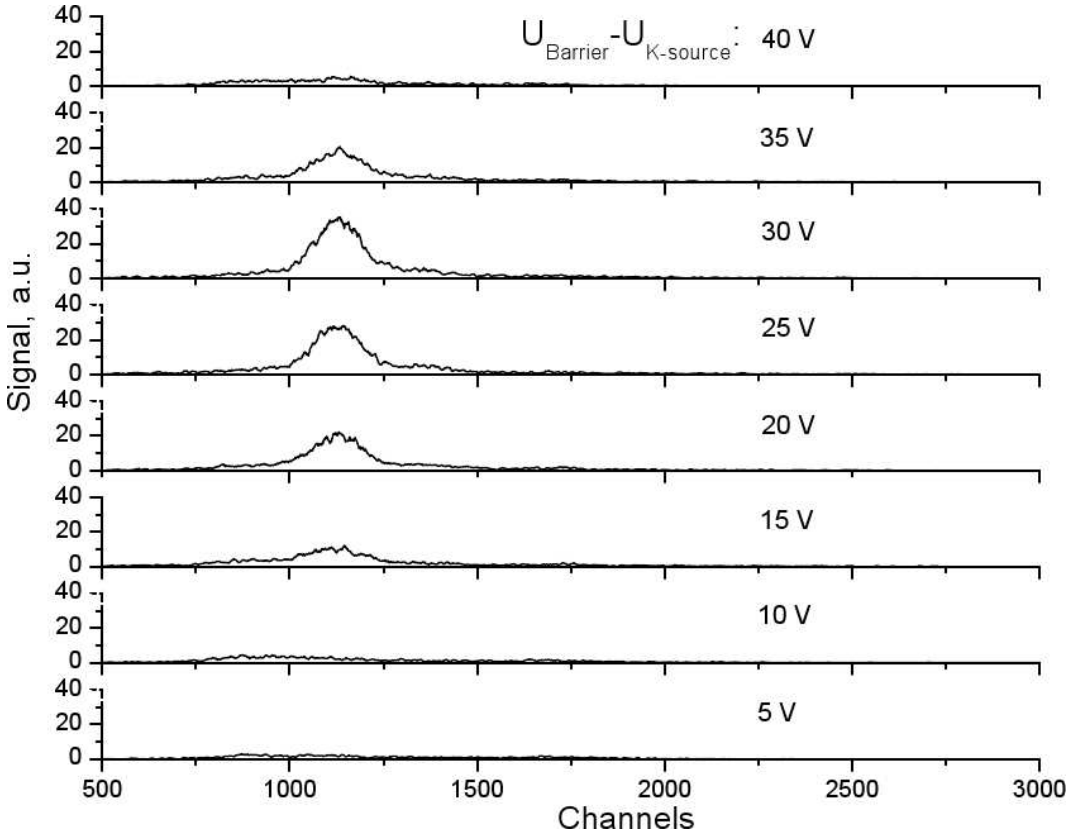

Figure 7.6: X-rays spectra with injected K^+ ions for different extraction barrier potentials. K^+ ion source potential is fixed 5 V above the ionization chamber potential.

Our first successful experiment with injection of K^+ ions from the external source was performed below the extraction barrier potential. The electron beam energy and current were 7.4 keV and 23 mA, respectively, the ionization chamber potential was set to 4.83 kV, the first drift tube to 4.9 kV and the K^+ ion source to 4.835 kV. The extraction (barrier) electrode potential was varied from 5 V to 40 V above the potassium source potential. On fig. 7.6 one can see different X-ray spectra for different potentials. It is clearly seen that the mixture of not resolved K_α and K_β lines appears in the spectra for rather high barrier potentials with maximum intensity at 30 V above the potential of the singly charged ion source. Further increase of the potential decreases the amount of ions entering the trap and completely reflect the upcoming ion beam at 40 V above the potassium ion source potential. Approximately 30 V is a depth of the potential well created by the electron space charge for the set conditions (see formula 5.12). Fixing further the barrier hight the potential of the ionization chamber was varied. The result showed that the best setting is when the ionization chamber potential is equal to the potential of the potassium ion source. That in principle means that the ions in the middle

electrode moving along the axis, are rather fast with 30 eV kinetic energies (above the bottom of the potential well). Still this is not really true for the closed trap region where the electron potential is at list partially screened by residual gas ions which can not escape easily as in the case of the barrier electrode and thus the injected ion velocities should be rather low. Charged spieces screening the electron space charge also can serve as a Coulomb target for the incident K^+ ions decelerating them efficiently.

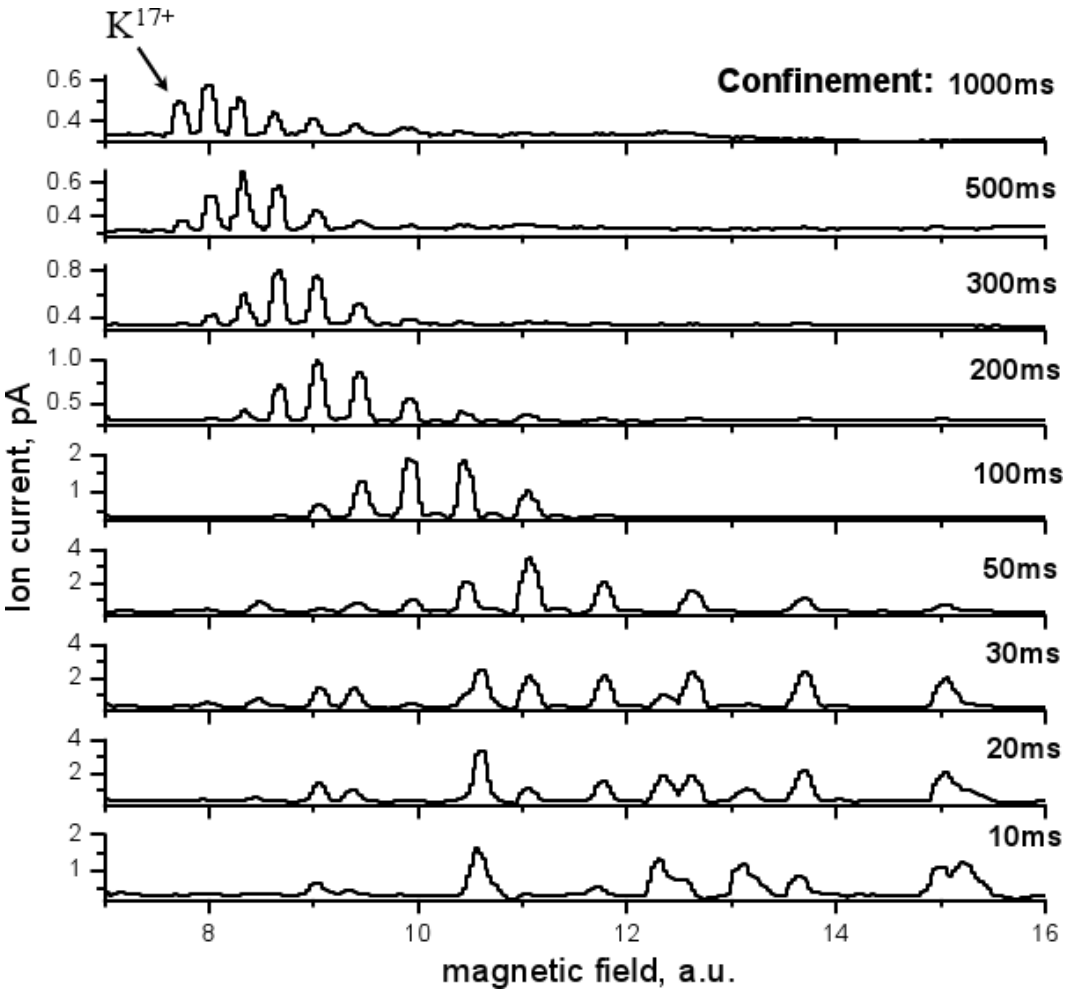

Figure 7.7: Magnetic scans of K ions extracted from the SPARC EBIT for different confinement times. The K^+ was continuously injected from the surface singly charged ion source.

As the main settings for the injection were established the further optimization and charge state manipulations were performed. On fig. 7.7 one can see charge state distributions for different confinement times of the charge bred potassium ions, measured on a FC2 after the MPS scanning the magnetic field. During the measurements the ions were injected continuously over (or better to say into) the barrier. As in the case of the gaseous Ar injection (see fig. 6.13

for comparison) the common behaviour can be seen. At first within 20 ms the residual gas ions dominate the charge state distribution. After a longer confinement higher and higher charge states of K ions show up in the spectra. Finally only potassium ions fill the storage capacity of the trap, with the same amount of HCI as for the gaseous Ar injection. At approximately 1000 ms the equilibrium is reached and there are no further changes in charge state distribution. The continuous influx of K^+ plays the same role as the continuous injection of neutral Ar, replenishing the trap. That led to a bit broader distribution compared to the pulsed injection, due to the constant production of low and medium potassium charge states which replace some HCI. Also the collisions between singly charged upcoming K^+ ions and there captured highly charged species influence the charge balance due to a Landau-Spitzer heating, caused not (only) by the high energetic electrons in this case, but by a flux of heavy low energetic ions. Additional disadvantage of continuous injection is that the effeciency of captured and charge bred species is rather low, when the trap is full within a short time. In continuous injection case the efficiency was estimated to be around $4 \cdot 10^{-6}$.

If one will take into account the rate of charge compensation in the trap (see fig. 6.12), which is filled approximately up to 85% within 20 ms, it is clear that the continuous injection is not very necessary. So we tried to perform a pulsed injection into the trap. For that purpose the voltage applied to the Einzel lens in front of the EBIT was also pulsed, stopping the injection of the beam from the K-source for a chosen time. On fig. 7.8 one can see a charge state distribution in case of 50 ms injection, right after the moment when the trap was closed again, for different confinement times.

The injection of K ions within a short time period happens in parallel with creation of the residual gas ions in the trap. Still due to the charge limit and increase of the average charge state in the trap the number of initially captured ions is decreasing (see fig. 7.9). As the K is the heaviest element in comparison to the residual gas species and has higher possible charge state, and thus better confinement, it repells the residual gas ions from the trap. Longer charge breeding time increases the K ions charge states and allows to contain effeciently the species in the source without losses. On fig. 7.9 one can see that the number of captured K ions is pretty stable for long confinement times.

As there is no additional influx of singly charged species and there is no increasing of multiply charged ions in the trap, which can repel higher charge states, the only thing which slows down and stop the charge evolution is the charge exchange with the residual gas ions. As one can see on fig. 7.8 the charge state distribution after 1000 ms of confinement is narrower than in the case of continuous injection and even more, afterwards the equilibrium does not happen. Charge states evolution continues up to 2000 ms. After that confinement time the production of hydrogen-like and even a small amount of bare K ions were observed. The maximum of the ion charges (around 80%)

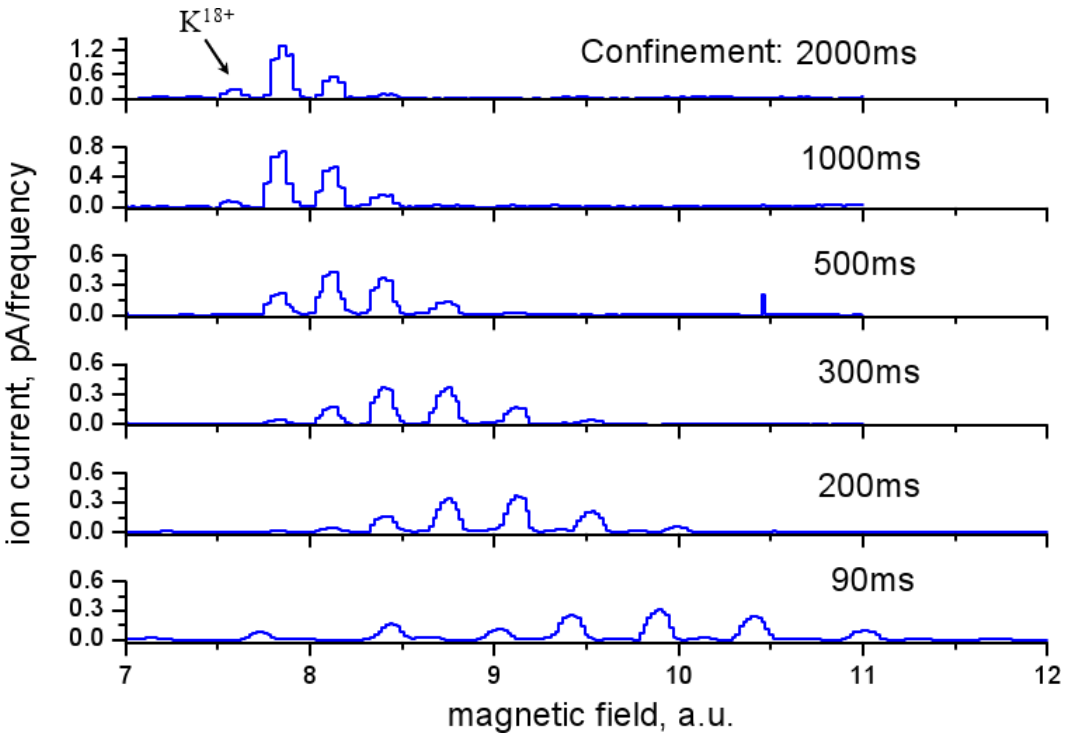

Figure 7.8: Magnetic scans of extracted K ion species from the SPARC EBIT for different confinement times. The K^+ was injected as a 20 ms pulse from the surface singly charged ion source.

was concentrated in the K^{17+} state. Unfortunately longer charge breeding was not possible to detect with magnetic scans due to the small signal on the currentmeter.l higher charge states, the only thing which slows down and stop the charge evolution is the charge exchange with the residual gas ions. As one can see on fig. 7.8 the charge state distribution after 1000 ms of confinement is narrower than in the case of continuous injection and even more, afterwards the equilibrium does not happen. Charge states evolution continues up to 2000 ms. After that confinement time the production of hydrogen-like and even a small amount of bare K ions were observed. The maximum of the ion charges (around 80%) was concentrated in the K^{17+} state. Unfortunately longer charge breeding was not possible to detect with magnetic scans due to the small signal on the currentmeter.

Thus to increase the number of charge states in the trap one should get rid of the continuous injection into the ionization chamber. Using the pulsed scheme of injection increased the mentioned efficiency of charge breeding by a factor of 50 (for 20 ms of injection) and thus is $2 \cdot 10^{-4}$ in the moment.

To summarize the results obtained on charge breeding in a compact room temperature EBIT it should be stated that the reached overall injection-capture-extraction efficiency is lower than in existing charge state breeders,

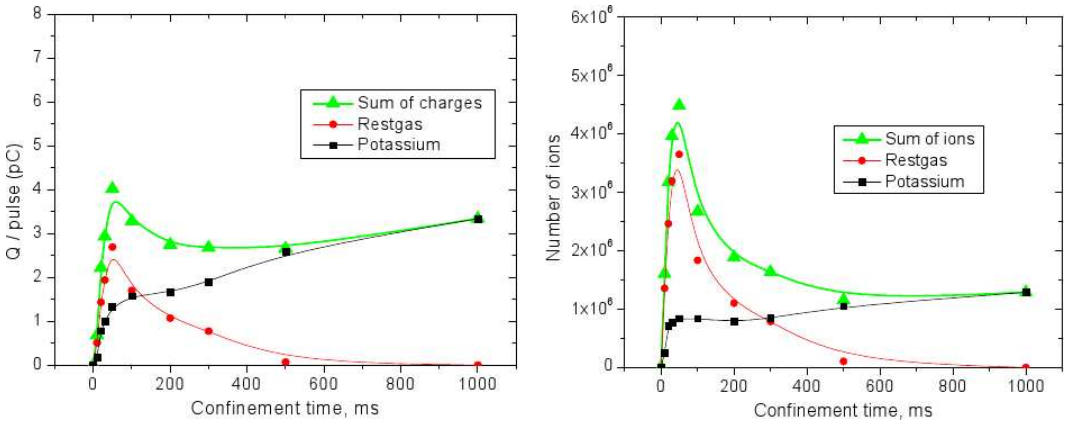

Figure 7.9: The charge and number of different ions contained in the trap in dependence on confinement time.

but quite high for this compact type of source. It can be increased even further with a better quality of the injected beam and using pulsed injection. To our knowledge up to the moment no charge breeding experiments were performed with such new type of room temperature EBITs, which show rather good possibility for that purpose. Different ion sources can be installed instead of the potassium ion source and so in future due to the successful charge breeding with the EBIT different highly charged species will be provided for HITRAP.

Due to the efficiency of the charge breeder, which is still less in comparison to the big set-ups, like REXEBIS, where the efficiency is in the range of 6% to 33% and also due to the small capacity of the trap, the SPARC EBIT is definitely not suitable for post-acceleration facililties. Still a production of low and medium Z highly charged species is possible for mass and g-factor measurements, and even for laser spectroscopy[1]. Due to a rather fast production rate, even small number of ions can be accumulated in the traps, where a sufficient amount of ions can be reached. So the HITRAP experimental setups will be provided in future with different HCI for interesting offline experiments.

[1]The number of ions necessary for the measurements is $\geq 10^5$

Chapter 8

Summary and outlook

During this PhD work design, simulation, installation and operation of the electron beam ion source and ion trap setups were performed, dedicated to the charge breeding experiments and off-line delivery of highly charged ions to the HITRAP facility, for which commissioning and preparation to the multi-electron ion-atom collision investigations using MOTRIMS technique were also done.

In the thesis an overview on the HITRAP project is given and the main parts of the decelerator facility as well as the proposed future experiments are described. During construction of the HITRAP facility, six beamtimes with highly charged ions at an energy of 4 MeV/u from the ESR storage ring have been held since 2007 for the commissioning tests. The double-drift buncher was fully commissioned and showed the design values in transmission, emittance and expected time structure of the beam. To have efficient deceleration in the IH-structure the injected ion beam should have a well-formed nanoseconds-bunches matched to the rf-phase of the IH-structure. The performance of the IH decelerator was tested and showed also good transmission, emittance and efficient deceleration from 4 MeV/u to 500 keV/u. Still there is room left for improvements by optimization of the amplitude and the relative phases of the double-drift buncher and the IH-structure. After the deceleration the energy distribution is measured by polycrystalline and single crystall diamond detectors, which have a high energy- and time- resolution. The Radio Frequency Quadrupole decelerator has been partially commissioned. The beam was transported through it and no significant losses were detected on the MCP-phosphor screen detector. The amount of ions decelerated down to 6 keV/u in the RFQ is an issue for future measurements. The Low Energy Beam Transport section has been set up and the Cooler Trap with the vertical beam line are nearly completely finished. On the HITRAP experimental platform the EBIT is installed and is fully operational. It will be used to deliver highly charged ions to establish the settings for the vertical beamline and to test the Cooler Trap. The ions from the source will be helpful to speed up the commissioning of the HITRAP facility. As soon as the RFQ parameters will be optimized, the rest

of the beamline will have also been tested from the other end and there should be no problem to deliver finally heavy highly charged ions from the ESR to the experimental setups.

One of the future experiments at HITRAP will be ion - atom collision studies. This topic is thus covered from the theoretical point of view and with experimental investigation on ions from ion source. An overview on the classical-over-barrier and statistical phenomenological models is presented with quantitative calculations. At HITRAP the experiments will be conducted with heavy highly charged projectiles for which the theoretical models predict multi-electron charge exchange and allow to make estimations of the collision cross sections. Still the predictive power of the models is limited and further theoretical development should be done. Already existing Basis Generator and Classical Trajectory Monte Carlo methods are suitable tools to tackle the problem of multi-electron charge exchange. Still the number of experimental results does not allow to approve the application of one or another model in the field of future investigations. For collision experiments gas jet and MOT targets will be involved in the future. The study of the collision products will allow to determine cross sections and Q-values of different processes. An experiment at KVI/Groningen with a MOTRIMS setup provided experimental results on this topic. Ion optical simulations were done for the Recoil Ion Momentum spectrometer from Heidelberg attached to the Rb - MOT, which will be used at HITRAP later on. The spectrometer is suitable for collision studies with ions in low and medium charge states. Additional modifications will allow to use the setup for heavy highly charged projectiles as well.

Low- and medium - Z ions in high charge states as well as high - Z ions in low and medium charge states can be delivered off-line from the existing EBIT ion source at HITRAP not only for collision studies, but also for other experiments as well. In the moment HCI are very interesting for high-precision mass measurements. Few-electron systems, as hydrogen- or Li- like ions are required for precise bound electron g-factor measurements. Some of the experimental setups are already being installed (g-factor trap) or already exist (SPECTRAP for laser spectroscopy) on the HITRAP platform. The beamlines to connect the setups with the ion source and the vertical beamline will be built in the beginning of 2010.

During this work two ion sources were put into operation and intensely studied. Experiments on charge breeding of singly charged species injected into an EBIT/S from an external ion source were performed. This investigation was covered by the EU networks EURISOL-DS and by the I3-EURONS projects. The main goal of the investigation was to obtain a high efficiency for the charge breeding process, which was successfully achieved with the cryogenic MAXEBIS setup. Our results can be used in principle in planned facilities like MATS, EURISOL or existing facilities, like REX-ISOLDE, which will or already deal with the charge breeding of rare isotopes for nuclear physics studies. Charge breeding was also investigated by us in the room temperature

SPARC EBIT and revealed interesting features, like the necessity to inject the ions below the barrier potential into the gate way created by the electron beam or efficient pulsed "into"-barrier injection. Such kind of experiments was never performed to our knowledge for this type of ion source. Besides the direct interest in the physical process itself, the successful charge breeding in SPARC EBIT will provide the HITRAP experiments with a variety of elements in high charge states.

Appendix A

Atomic units

In the atomic unit (a.u.) system the following main constants are equal to unity:

$$\frac{h}{2\pi} = m_e = e = 4\pi\epsilon_0 = 1, \tag{A.1}$$

here h is the Planck's constant, m_e and e are the electron mass and charge, respectively, ϵ_0 is the vacuum permittivity. The speed of light c in atomic units is equal to $\alpha = 1/137$ - the fine structure constant. The Bohr radius $a_0 = \epsilon_0 h^2/(\pi m_e e^2) = 1$ is used as a unit of length. As a unit of energy $2 \cdot Ry = 27.6$ eV is used, where Ry is the Rydberg constant. In the table below some SI (International System of units) values related to 1 atomic unit of the corresponding quantity are listed.

Table A.1: Several SI values related to 1 atomic unit of the corresponding quantity

Atomic unit of:	SI value
length	$0.529 \cdot 10^{-10} m$
time	$2.419 \cdot 10^{-17} s$
velocity	$2.188 \cdot 10^{6} m/s$
mass	$9.110 \cdot 10^{-31} kg$
energy	$4.359 \cdot 10^{-18} J$
charge	$1.602 \cdot 10^{-19} C$
momentum	$1.993 \cdot 10^{-24} kgm/s$
angular momentum	$1.055 \cdot 10^{-34} Js$

To convert keV/u kinetic energy value into velocity in atomic units one should use the formula:

$$v[a.u.] = 0.2\sqrt{E[keV/u]}. \tag{A.2}$$

From the eq. A.2 using tab. A.1 one can obtain another useful formula for the

velocity in SI units:

$$v[m/s] = 1.39 \cdot 10^4 \sqrt{E[eV]/m[u]}. \tag{A.3}$$

Appendix B

Magnetic field in case of cylindrical symmetry

Magnetic field in a free space is described by Maxwell equations:

$$\nabla \times B = 0, \tag{B.1}$$

$$\nabla \cdot B = 0. \tag{B.2}$$

The first one B.1 allows the magnetic field to be derived from a scalar potential defined by $B = \nabla\varphi$ substituting which into the B.2 will lead to the Laplace equation $\Delta\varphi = 0$. Actually the electrostatic field is described by the same couple of equations, thus the final result for the magnetic field is valid for the electrostatic field as well. In cylindrical coordinates (z, r, θ) the Laplace equation can be solved separating veriables. As the magnetic field is independent on the angle, only two components remain, i.e. radial (B_r) and longitudinal (B_z) for which the final result is:

$$B_z(r,z) = \sum_{n=0}^{\infty} \frac{(-1)^n}{n!^2} (\frac{r}{2})^{2n} B_z^{(2n)}(0,z), \tag{B.3}$$

$$B_r(r,z) = -\frac{r}{2} \sum_{n=0}^{\infty} \frac{(-1)^n}{n!(n+1)!} (\frac{r}{2})^{2n} B_z^{(2n+1)}(0,z) \tag{B.4}$$

here $B_z(0,z)$ is the magnetic field along the axis of symmetry. In the vicinity of the axis when the variable r is small, one can use the first terms of expansions B.3 and B.4 to get the components in the form:

$$B_z(r,z) = B_z(0,z), \tag{B.5}$$

$$B_r(r,z) = -\frac{r}{2} \frac{\partial B_z(0,z)}{\partial z} \tag{B.6}$$

On the axis of a solenoid at the distance a from the solenoid center one can use the Bio-Savart's law to obtain the magnetic field:

$$B_z(0,a) = \mu_0 \frac{NJ}{4(R_2 - R_1)}((l-a)ln\frac{R_2 + \sqrt{R_2^2 + (l-a)^2}}{R_1 + \sqrt{R_1^2 + (l-a)^2}} + (l+a)ln\frac{R_2 + \sqrt{R_2^2 + (l+a)^2}}{R_1 + \sqrt{R_1^2 + (l+a)^2}}), \tag{B.7}$$

where R_1 and R_2 are the inner and outer radii of the solenoid, respectively, N - number of coils, J - electron current, μ_0 the vacuum permeability and l is a length of the solenoid. Using the formulas above B.3 and B.4 one can get magnetic field around the axis.

Appendix C

Emittance measurements using 3- (multi-) gradient method

Ions in the beam, moving along the optical axis, has velocity components in the plane perpendicular to the flight direction. Taking into account two orthogonal coordinates of the plane and velocity components along them, ions occupy a volume in the 4D phase space (x, y, v_x, v_y) which due to the Liouville theorem is kept constant over time[1]. Usually to obtain analytical solution for the volume deformation along the axis the volume is assumed to be a 4D ellipsoid[2]. Projection on the (x, v_x) and (y, v_y) planes will give the ellipses for which the equations are in the form:

$$\gamma x^2 + 2\alpha x x' + \beta x'^2 = \epsilon, \tag{C.1}$$

where instead of v_x the normalized value $x' = v_x/v_z$ is used. The α, β, γ are called Twiss parameters for which the relation:

$$\beta\gamma - \alpha^2 = 1 \tag{C.2}$$

is true. The ϵ value is the emittance of the beam, i.e. the constant phase space area divided by π. The correspondence between the ellipse coordinate (x_0, x'_0) at the position z_0 and the ellipse coordinate (x, x') at the position z is determined by a transport matrix A:

$$\begin{pmatrix} x \\ x' \end{pmatrix} = A \begin{pmatrix} x_0 \\ x'_0 \end{pmatrix} = \begin{pmatrix} c & s \\ c' & s' \end{pmatrix} \begin{pmatrix} x_0 \\ x'_0 \end{pmatrix}. \tag{C.3}$$

[1] In principle invariant is the total 6D phase space, but here the time structure of the beam is kept constant and thus only transverse planes are considered

[2] The shape of the beam is nearly ellipsoidal for example for the ions extracted from the EBIT with small magnetic field. The ions inside such a source are moving in the electrostatic harmonic potential well created by the electron space charge (see chapter 5), thus their radial velocity components are maximal on the axis, and nearly equal to zero at some distances from the axis. Assuming the energy conservation (no interaction with the environment) for a single ion in a harmonic trap one can write a formula $av(R)^2 + bR^2 = c$, where R is a distance from the axis.

The transport matrix for the drift without any optical element is:

$$A_{drift} = \begin{pmatrix} 1 & l \\ 0 & 1 \end{pmatrix}, \tag{C.4}$$

where l is a drift length. For the thin lens the transport matrix is:

$$A_{lens} = \begin{pmatrix} 1 & 0 \\ -\frac{1}{f} & 1 \end{pmatrix}, \tag{C.5}$$

where f is a focal length of the lens. Expressing x, x' coordinates at the position z through the transport matrix components and x_0, x'_0 coordinates at the position z_0 one can substitute them then into the eq. C.1. Comparing the coefficients of the $x_0^2, x_0x'_0, x_0'^2$, in the obtained equation, with $\gamma_0, \alpha_0, \beta_0$, respectively, one can find out the relation between $\gamma_0, \alpha_0, \beta_0$ and γ, α, β in the form:

$$\begin{pmatrix} \beta \\ \alpha \\ \gamma \end{pmatrix} = \begin{pmatrix} c^2 & -2sc & s^2 \\ -c'c & s'c + c's & -s's \\ c'^2 & -2s'c' & s'^2 \end{pmatrix} \begin{pmatrix} \beta_0 \\ \alpha_0 \\ \gamma_0 \end{pmatrix}, \tag{C.6}$$

If the beam passes through a thin lens with focal length f and hit the screen after a drift distance l for profile measurements the correspondent transport matrix from behind the lens to the screen is:

$$A = A_{drift}A_{lens} = \begin{pmatrix} 1 - \frac{l}{f} & l \\ -\frac{1}{f} & 1 \end{pmatrix}. \tag{C.7}$$

Substituting the components of the final transport matrix into the system of linear equations C.6 one can express the parameter β at the screen position through the Twiss parameters in front of the lens in the form:

$$\beta = (1 - \frac{l}{f})^2\beta_0 - 2l(1 - \frac{l}{f})\alpha_0 + l^2\gamma_0. \tag{C.8}$$

On fig. C.1 one can see the phase space ellipse described by the formula C.1. Different parameters of the ellipse like maximal x or x' can be expressed through the Twiss parameters and emittance. So measuring the radius of the beam will give a $\sqrt{\epsilon\beta}$. Multiplying both parts of equation C.8 by ϵ one obtain in the left part radius (r) of the beam squared and in the right part three unknown parameters $\epsilon\beta_0, \epsilon\alpha_0$ and $\epsilon\gamma_0$. Changing the focal length of the lens applying different voltage and measuring the beam radius on the screen will provide enough information to calculate the unknown parameters and thus, using eq. C.2 the emittance.

In principle three measurements are enough to obtain ϵ from:

$$\begin{pmatrix} r_1^2 \\ r_2^2 \\ r_3^2 \end{pmatrix} = \begin{pmatrix} (1 - \frac{l}{f_1})^2 & -2l(1 - \frac{l}{f_1}) & l^2 \\ (1 - \frac{l}{f_2})^2 & -2l(1 - \frac{l}{f_2}) & l^2 \\ (1 - \frac{l}{f_3})^2 & -2l(1 - \frac{l}{f_3}) & l^2 \end{pmatrix} \begin{pmatrix} \epsilon\beta_0 \\ \epsilon\alpha_0 \\ \epsilon\gamma_0 \end{pmatrix}, \tag{C.9}$$

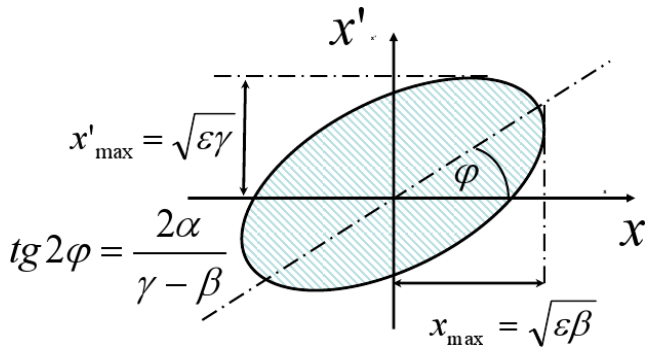

Figure C.1: Phase space ellipse. The maximal radius and angle are related to the Twiss parameters β, γ and emittance ϵ

that's why the described method is called originally a 3-gradient method. Still to obtain a more precise value for emittance more than three measurements are usually done. In that case a system of equations C.9 is represented as:

$$\begin{pmatrix} b_{11} & b_{12} & b_{13} \\ b_{21} & b_{22} & b_{23} \\ \dots & & \\ b_{n1} & b_{n2} & b_{n3} \end{pmatrix} \begin{pmatrix} \epsilon\beta_0 \\ \epsilon\alpha_0 \\ \epsilon\gamma_0 \end{pmatrix} = \begin{pmatrix} r_1^2 \\ r_2^2 \\ \dots \\ r_n^2 \end{pmatrix}, \tag{C.10}$$

where in the B - matrix the coefficients are of the form as in the C.9. Introducing vectors $\vec{r} = (r_1^2, r_2^2, ..., r_n^2)$, $\vec{b}_j = (b_1, b_2, ..., b_n)$ and variables $z_1 = \epsilon\beta_0$, $z_2 = \epsilon\beta_0$, $z_3 = \epsilon\beta_0$ one can obtaine "the best solution" for the C.10 solving a system of only three equations:

$$(\vec{r}, \vec{b}_j) - \sum_{i=1}^{n} z_j(\vec{b}_i, \vec{b}_j) = 0, \tag{C.11}$$

where $(\vec{x}, \vec{y})$ is a scalar product. For details to the 3-gradient method I would refer to [Kes92, Wol87].

Bibliography

[And91] L. H. Andersen, *Dielectronic and radiative recombination with highly charged ions*, Zeitschrift fr Physik D Atoms, Molecules and Clusters **21** (1991) S29.

[Ban85] J. Bang, J. De Boer, *Semiclassical descriptions of atomic and nuclear collisions*, Proceedings of the Niels Bohr Centennial Conference Copenhagen, March 25-28, Elsevier Science Publishers B.V., 1985.

[Bec99] R. Becker *INTMAG*, Internal software (1999).

[Bec07] R. Becker, O. Kester, and T. Stoehlker, *Simulation of charge breeding for trapped ions*, J. Phys.: Conference Series **58** (2007) 443.

[Bee99] E. Beebe, J. Alessi, S. Bellavia, A. Hershcovitch, A. Kponou, R. Lockey, A. Pikin, and K. Prelec, *Results of Beam Tests on a High Current EBIS Test Stand*, Conf. Proc., Particle Accelerator Conference, New York (1999) BNL 66021 (1999)

[Bei00] T. Beier, *The g-factor of a bound electron and the hyperfine structure splitting in hydrogenlike ions*, Phys. Rep. **339** (2000) 79.

[Bei03] T. Beier, L. Dahl, H. J. Kluge, C. Kozhuharov, and W. Quint, *HITRAP Technical Design Report*,GSI internal document (2003)

[Bla07] I. Blank, *Rueckstossionenspektroskopie mit magneto-optischen Fallen*, Diplomarbeit, Freiburg (2007)

[Bla06] K. Blaum, *High-accuracy mass spectrometry with stored ions*, Phys. Rep. **425** (2006) 1.

[Blo06] M. Block, D. Ackermann, K. Blaum, A. Chaudhuri, Z. Di, S. Eliseev, R. Ferrer, D. Habs, F. Herfurth, F. Heberger, S. Hofmann, H. J. Kluge, G. Maero, A. Martn, G. Marx, M. Mazzocco, M. Mukherjee, J. Neumayr, W. Pla, W. Quint, S. Rahaman, C. Rauth, D. Rodrguez, C. Scheidenberger, L. Schweikhard, P. Thirolf, G. Vorobjev, and C. Weber, *Mass measurements in the endpoint region of the rp-process at SHIPTRAP*, Hyp. Int. **173** (2006) 133.

[Bri80] J.S. Briggs and L. Dube, *The second Born approximation to the electron transfer cross section*, J. Phys. B **13** 771 (1980).

[Bri45] L. Brillouin, *A Theorem of Larmor and Its Importance for Electrons in Magnetic Fields*, Phys. Rev. **67** (1945) 260.

[Cai03] X. Cai, D. Yu, X. Chen, R. Lu, Z. Cao, W. Yang, C. Shao and X. Ma, *The Transfer Ionization of* $Ar^{q+} - He$, $Ar^{q+} - Ne$ *and* $Ar^{q+} - Ar$ *Collisions*, Physica Scripta **68** (2003) 227.

[Cle08] G. Clemente and U. Ratzinger, *HITRAP: IH Beam Dynamics Investigation*, GSI internal document (2008).

[Col68] J. P. Coleman and S. Trelease, *Electron capture into excited states in the impulse approximation*, J. PHYS. B (PROC. PHYS. S O C .) 1 (1968) 172.

[Cur03] F. J. Currell, *The Physics of Multiply and Highly Charged Ions*, Vol. 1 Sources, Applications and Fundamental Processes, Kluwer Academic Publishers (2003)

[Dal75] J. Dalibard and C. Cohen-Tannoudji, *Laser cooling below the Doppler limit by polarization gradients: simple theoretical models*, J. Opt. Soc. Am. B 6 (1989) 2023.

[Dah00] D.A. Dahl, *Simion 3D version 7.0 user's manual*, BECHTEL BWXT IDAHO, LLC (2000)

[Dah04] L. Dahl, Th. Beier, W. Vinzenz, *The HITRAP - decelerator for heavy highly-charged ions*, Proceedings of LINAC 2004, Luebeck, Germany (2004) 39.

[deJ04] V. L. B. de Jesus, A. Rudenko, B. Feuerstein, K. Zrost, C. D. Schrter, R. Moshammer, and J. Ullrich, *Reaction microscopes applied to study atomic and molecular fragmentation in intense laser fields: non-sequential double ionization of helium*, Journal of Electron Spectroscopy and Related Phenomena **141** (2004) 127.

[Don67] E. G. Donets, *Electron Beam Ion Source*, USSR Inventor's Certificate N 248860 (1969)

[DREEBIT] http://www.dreebit.com

[DuB86] R. D. DuBois, *Charge transfer leading to multiple ionization of neon, sodium, and magnesium*, Phys. Rev. A **34** (1986) 2738.

[Gra80] G. Graeff, H. Kalinowsky and J. Traut, *A direct determination of the proton electron mass ratio*, Z. Phys. A **297** (1980) 35.

[Gru03] P. Gruber, *Normalized emittance in the case of large momentum spreads*, J. Phys. G **29** (2003) 1693.

[GSI-webpage] http://www.gsi.de/fair/experiments/sparc/coltrims.html

[Hae00] H. Haeffner, T. Beier, N. Hermanspahn, H. J. Kluge, W. Quint, S. Stahl, J. Verdu, and G. Werth, *High-Accuracy Measurement of the Magnetic Moment Anomaly of the Electron Bound in Hydrogenlike Carbon*, Phys. Rev. Let. **85** (2000) 5308.

[Has06] V. G. Hasan, *MOTRIMS investigations of electron removal from Na by highly charged ions*, PhD Thesis, Kroningen (2008).

[Her06] F. Herfurth, T. Beier, L. Dahl, S. Eliseev, S. Heinz, O. Kester, C. Kozhuharov, G. Maero, and W. Quint, *Precision measurements with highly charged ions at rest: The HITRAP project at GSI*, Int. J. of Mass Spectrometry **251** (2006) 266.

[Her57] G. Herrmann, *Optical Theory of Thermal Velocity Effects in Cylindrical Electron Beams*, JAP, **29**, 127 (1957)

[Hei06] S. Heinz, *HITRAP LEBT and experiments*, GSI internal report.

[Hof07] B. Hofmann, *Konstruktion und Aufbau einer kompakten RFQ-Spiral-Structur zum Abbremsen hochgeladener Schwerionenstrahlen fuer das HITRAP-Projekt ger GSI.*, PhD thesis, Frankfurt (2007).

[Hor94] M. Horbatsch, *A semiclassical time-dependent Hartree model calculation of capture and multiple ionization in heavy ion-Ar collisions*, Phys. Let. A **187** (1994) 185.

[Jai96] A. Jain and T. G. Winter, *Single electron transfer and target excitation in $He^{2+} + Na(3s)$ collisions at 2 - 50 keV/u in the coupled-Sturmian-pseudostate approach*, J. Phys. B: Atomic, Molecular and Optical Physics **29** (1996) 4675.

[Kar06] F.F. Karpeshin, *Nuclear fission reaction in muonic atoms*, Izdatel'stvo "Nauka", 2006

[Kes92] O. Kester, R. Rao, and L. Rinolfi, *Beam Emittance Measurements from CERN Thermionic Guns*, CERN, CH-1211 Geneva **23** (1992).

[Kes06] O. Kester, H. Zimmermann, R. Becker, and M. Kleinod, *The Frankfurt MAXEBIS setup for advanced charge breeding experiments*, Rev. Sci. Inst. **77** (2006) 03B102.

[Kes08a] O. Kester, R. Becker, J. Pfister, A. Sokolov, G. Vorobjev, M. Vogel, D. Winters, and H. Zimmermann, Rev. Sci. Inst. **79** (2008) 02A705.

[Kes08b] O. Kester, *Charge breeding application of EBIS/T devices*, AIP conference proceedings 1099, p.7 (2008).

[Kin01] T. Kinugawa, F. J. Currell, and S. Ohtani, *Pulsed Evaporative Cooling of Ion Cloud in an Electron Beam Ion Trap*, Physica Scripta **T92** (2001) 102.

[Klu05] H.-J. Kluge, T. Beier, K. Blaum, M. Block, L. Dahl, S. Eliseev, F. Herfurth, S. Heinz, O. Kester, C. Kozhuharov, T. Khl, G. Maero, W. Nrtershuser, T. Sthlker, W. Quint, G. Vorobjev, G. Werth, and t. H. Collaboration,*HITRAP - A facility at GSI for Experiments on Stored and Cooled Highly Charged Ions at Rest*, Frankfurt, Conference Proceeding (2005) P. 89.

[Klu07] H. J. Kluge, W. Quint, and D. F. A. Winters, *Atomic physics experiments with trapped and cooled highly charged ions*, J. Phys.: Conference Series, **58** (2007) 9.

[Kno05] S. Knoop, R. E. Olson, H. Ott, V. G. Hasan, R. Morgenstern, and R. Hoekstra, *Single ionization and electron capture in $He^{2+} + Na$ collisions*, J. Phys. B **38** (2005) 1987.

[Kno06] S. Knoop, *Electron Dynamics in Ion-Atom Interactions*, PhD Thesis, Kroningen (2006).

[Knu81] H. Knudsen, H. K. Haugen, and P. Hvelplund, *Single-electron-capture cross section for medium- and high-velocity, highly charged ions colliding with atoms*, Phys. Rev. A **23** (1981) 597.

[Kos71] V. O. Kostroun, M. H. Chen, and B. Crasemann, *Atomic Radiation Transition Probabilities to the 1s State and Theoretical K-Shell Fluorescence Yields*, Phys. Rev. A **3** (1971) 533.

[Kos83] V. O. Kostroun, E. Ghanbari, E. N. Beebe, and S. W. Janson, *An EBIS for Atomic Physics Experiments*, Physica Scripta **T3** (1983) 47.

[Kos09] S. Koszudowski, *Developments for the HITRAP Cooler Trap and mass measurements around A=96 at SHIPTRAP*, PhD Thesis, Heidelberg (2009)

[Koz08] C. Kozhuharov, *Diamonds for HITRAP and for Future Electron Spectroscopy*, Talk during the 4th NoRHDia Workshop, GSI (2008).

[Kro99] O. J. Kroneisen, H. J. Ludde, T. Kirchner and R. M. Dreizler, , Journal of Physics A: Mathematical and General **32** (1999) 2141.

[Lak92] A. Lakatos, *Ein magnetisches Ionen-Spektrometer mit Mehrfachdurchgang als Energie- und Massenanalysator sowie als Strahlweiche und Speicher*, Diplomarbeit, Frankfurt, 1992

[Lan89] L.D. Landau, E.M. Lifshits, *Quantum mechanics*, Vol. 3, Izdatel'svo nauka, 1989.

[Lot68] W. Lotz, *Electron-impact ionization cross sections and ionization rate coefficients for atoms and ions from hydrogen to calcium*, Zeitschrift für Physik A Hadrons and Nuclei **216** (1968) 241.

[Lue96] H. J. Ludde, A. Henne, T. Kirchner and R. M. Dreizler, *Optimized dynamical representation of the solution of time-dependent quantum problems*, J. Phys B **29** (1996) 4423.

[Ma99] X. Ma, H. Liu, Y. Wang, Z. Yang, D. Yu, X. Chen, Z. Shen, X. Cai and Z. Liu, *Multiple Electron Transfer in Collisions of Highly Charged Ar Ions on Argon Atoms*, Physica Scripta T80B (1999) 375.

[Mae08] G. Maero, *Cooling of highly charged ions in a Penning trap for HITRAP*, PhD Thesis, Heidelberg (2008)

[Mad75] D.H.Madison and E. Merzbacher in Atomic Inter Shell Processes, ed. B. Crasemann (Academic Press, New York, 1975) p. 1.

[Mar04] J. Marriner, *Stochastic cooling overview* Nuc. Inst. Meth. in Physics Research Section A: Accelerators, Spectrometers, Detectors and Associated Equipment **532** (2004) 11.

[Mel94] G. Melin, F. Bourg, P. Briand, M. Delaunay, G. Gaudart, A. Girard, D. Hitz, J. P. Klein, P. Ludwig, T. K. Nguyen, M. Pontonnier and Y. Su, *Status of development of ECR ion sources at Grenoble (invited)*, in Proceedings of fifth international conference on ion sources, Vol. **65**, AIP, Beijing (China), 1994, p. 1051.

[Mon82] Montenegro and D. Pinho, *A general expression for the PWBA low-energy limit of ionisation cross sections by heavy ions*, LETTER TO THE EDITOR (1982)

[Mue83] A. Mueller, W. Groh and E. Salzborn, *Statistical Interpretation of Transfer Ionization in Slow Collisions of Multiply Charged Ions with Atoms*, Phys. Rev. Let. **51** (1983) 107.

[Mue77] A. Mueller and E. Salzborn, *Scaling of cross sections for multiple electron transfer to highly charged ions colliding with atoms and molecules*, Phys. Let. A **62** (1977) 391.

[New84] J. Newcomb, T. R. Dillingham, J. Hall, S. L. Varghese, P. L. Pepmiller and P. Richard, *Electron capture by metastable projectiles on He and Ne*, Phys. Rev. A **29** (1984) 82.

[Nie86] A. Niehaus, *A classical model for multiple-electron capture in slow collisions of highly charged ions with atoms*, J. Phys. B (1986) 2925.

[Nik89] V. K. Nikulin and A. V. Samoylov, *On the role of correlated double-electron capture in slow multiply charged N^{7+} collisions with He*, J. Phys. B. **22** (1989) L201.

[Ols72] R. E. Olson, *Charge Transfer at Large Internuclear Distances: Application to Asymmetric Alkali-Ion-Alkali-Atom Systems*, Phys. Rev. A **6** (1972) 1822.

[Ols76] R. E. Olson and A. Salop, *Electron transfer between multicharged ions and neutral species*, Phys. Rev. A **14** (1976) 579.

[Ols77] R. E. Olson and A. Salop, *Charge-transfer and impact-ionization cross sections for fully and partially stripped positive ions colliding with atomic hydrogen*, Phys. Rev. A **16** (1977) 531.

[Ovs07] V. P. Ovsyannikov, G. Zschornack, F. Grossmann, R. Heller, U. Kentsch, M. Kreller, S. Landgraf, M. Schmidt, and F. Ullmann, *First investigations on the Dresden EBIS-A*, J. Phys.: Conference Series **58** (2007) 399.

[Pen91] B. M. Penetrante, J. N. Bardsley, D. DeWitt, M. Clark, and D. Schneider, *Evolution of ion-charge-state distributions in an electron-beam ion trap*, Phys. Rev. A **43** (1991) 4861.

[Pen91a] B. M. Penetrante, J. N. Bardsley, M. A. Levine, D. A. Knapp, and R. E. Marrs, *Evaporative cooling of highly charged dysprosium ions in an enhanced electron-beam ion trap*, Phys. Rev. A **43** (1991) 4873.

[Per71] J. Perel and H. L. Daley, *Charge-Transfer Collisions Involving Electron Transfer to Excited States*, Phys. Rev. A **4** (1971) 162.

[Pfi09] J. Pfister, *Entwicklung und Anwendung schneller Strahldiagnose fr Ionenstrahlen*, PhD Thesis, Frankfurt (2009)

[Phi98] W. D. Phillips, *Nobel Lecture: Laser cooling and trapping of neutral atoms*, Rev. Mod. Phys. **70** (1998) 721.

[Qui05] W. Quint, M. Vogel, J. Alonso, S. Djekic, H. J. Kluge, S. Stahl, J. Verdu, and G. Werth, *Towards electronic g-factor measurements in medium-heavy hydrogen-like and lithium-like ions*, Nucl. Inst. Meth. in Physics Research Section B: Beam Interactions with Materials and Atoms **235** (2005) 7.

[Qui08] W. Quint, D. L. Moskovkhin, V. M. Shabaev, and M. Vogel, *Laser-microwave double-resonance technique for g-factor measurements in highly charged ions*, Phys. Rev. A **78** (2008) 032517.

[Run98] S. Runkel, O. Hohn, L. Schmidt, K. E. Stiebing, H. Schmidt-Bocking, A. Schempp and R. Becker, *Electron-beam extraction system for the Frankfurt 14 GHz electron cyclotron resonance ion source*, in Proceedings of the 7th international conference on ion sources, Vol. **69**, AIP, Shirahama, Wakayama (Japan), 1998, p. 721.

[Rus63] A. Russek, *Ionization Produced by High-Energy Atomic Collisions*, Phys. Rev. **132** (1963) 246.

[Rus58] A. Russek and M. T. Thomas, *Ionization Produced by Atomic Collisions at kev Energies*, Phys. Rev. **109** (1958) 2015.

[Sal76] A. Salop and R. E. Olson, *Charge exchange between H(1s) and fully stripped heavy ions at low-keV impact energies*, Phys. Rev. A **13** (1976) 1312.

[Sal77] A. Salop and R. E. Olson, *Electron removal from atomic hydrogen by collisions with fully stripped carbon*, Phys. Rev. A **16** (1977) 1811.

[Sav08] G. Savard, S. Baker, C. Davids, A. F. Levand, E. F. Moore, R. C. Pardo, R. Vondrasek, B. J. Zabransky and G. Zinkann, *Radioactive beams from gas catchers: The CARIBU facility*, Nucl. Inst. Meth. in Physics Research Section B: Beam Interactions with Materials and Atoms **266** (2008) 4086.

[Sch95] S. Schippers, P. Boduch, J. v. Buchem, F. W. Bliek, R. Hoekstra, R. Morgenstern, and R. E. Olson, *Polarized light emission in keV* $He^{2+} + Na(3s)$ *collisions*, J. Phys. B **28** (1995) 3271.

[Sch92] A. R. Schlatmann, R. Hoekstra, H. O. Folkerts, and R. Morgenstern, *Electron capture and excitation in* $He^{2+} - Na$ *collisions*, J. Phys. B **25** (1992) 3155.

[Sch97] H. T. Schmidt, H. Cederquist, R. Schuch, L. Bagge, A. Kllberg, J. Hilke, K. G. Rensfelt, V. Mergel, M. Achler, R. Drner, L. Spielberger, O. Jagutzki, H. Schmidt-Bcking, J. Ullrich, H. Reich, M. Unverzagt, W. Schmitt, and R. Moshammer, *A design study for an internal gas-jet target for the heavy-ion storage ring CRYRING*, Hyp. Int. **108** (1997) 339.

[Sch08] S. Schwarz, G. Bollen, M. Kostin, F. Marti, P. Zavodszky, J.R. Crespo Lopez-Urrutia, J. Dilling and O. Kester, *A high-current electron beam ion trap as a charge breeder for the reacceleration of rare isotopes at the NSCL*, Rev. Sci. Instrum. **79** (2008) 02A706.

[Sha79] R. Shakeshaft and L. Spruch, *Mechanisms for charge transfer (or for the capture of any light particle) at asymptotically high impact velocities*, Rev. Mod. Phys. **51** 369 (1979).

[Spi56] L. Spitzer Jr., *Physics of fully ionized gases*, Interscience publishers, inc. New York (1956)

[Spr78] L. Spruch, *Retardation effects and the vanishing as R [infinity] of the nonadiabatic R-6 interaction of the core and a high-Rydberg electron*, Phys. Rev. A **18** 2016 (1978).

[Tar05] O. Tarvainen, *Studies of Electron Cyclotron Resonance Ion Source Plasma Physics*, PhD thesis, Jyvaeskylae, (2005)

[Tar04] O. Tarvainen, P. Suominen, and H. Koivisto, *Effect of the gas mixing technique on the production efficiency of ion beams extracted from an electron cyclotron resonance ion source*, Nucl. Inst. Meth. in Physics Research Section B: Beam Interactions with Materials and Atoms **217** (2004) 136.

[Tau86] K. Taulbjerg, *Reaction windows for electron capture by highly charged ions*, J. Phys. B **19** (1986) L367.

[Tho27] L.H. Thomas, Proc. Roy. Soc. A114 561 (1927).

[Ull97] J. Ullrich, R. Moshammer, R. Dorner, O. Jagutzki, V. Mergel, H. Schmidt-Bocking, and L. Spielberger, *Recoil-ion momentum spectroscopy*, J. Phys. B **30** (1997) 2917.

[Ver04] J. Verdu, S. Djeki, S. Stahl, T. Valenzuela, M. Vogel, G. Werth, T. Beier, H. J. Kluge, and W. Quint, *Electronic g Factor of Hydrogenlike Oxygen*, Phys. Rev. Let. **92** (2004) 093002.

[Vog05] M. Vogel, D. F. A. Winters, D. M. Segal, and R. C. Thompson, *Proposed precision laser spectrometer for trapped, highly charged ions*, Rev. Sci. Inst.**76** (2005) 103102.

[Wen02] F. Wenander, *EBIS as charge breeder for radioactive ion beam accelerators*, Nucl. Phys. A **701** (2002) 528.

[Win82] Thomas G. Winter, *Electron transfer in p-He+ and He2+-H collisions using a Sturmian basis*, Phys. Rev. A **25** (1982) 697.

[Wol87] H. Wollnik, *Optics of Charged Particles*, Academic Press, Inc., 1987 (1987)

[Zha96] M. Zhang, *Emittance Formula for Slits and Pepper-pot Measurement*, FERMILAB, report (1996)

[Zwi06] G. Zwicknagel, *Electron Cooling of Highly Charged Ions in Penning Traps*, in: M. Drewsen, U. Uggerhoj, H. Knudsen, Non-neutral Plasma Physics VI , AIP Conf. Proc. **862** (2006) 281.

Acknowledgments

Big institutes and big projects always mean a lot of people whom you cooperate with during your hard work, trying to honor a Dr. prefix before your family name. During sometimes long, sometimes short periods of time in different fields people share with you there experience and provide you with useful knowledge and skills. Writing the acknowledgments is the right time to thank all the people who contributed to this work.

My gratitude goes to my supervisor Priv. Doz. Dr. Wolfgang Quint for accepting me as a PhD student, for his guidance during the writing and corrections of the thesis and for introduction into the world of magneto-optical and Penning traps. I'm also thankfull to Prof. Dr. Andreas Wolf for accepting to be my second supervisor, as well as to Priv. Doz. Habil. Ulrich Glasmacher and Prof. Dr. Juergen Schaffner-Bielich for joining the examination committee.

I sincerely thank Prof. Dr. Oliver Kester whose contribution to this work can not be over-estimated. There are numerous things to thank for, starting from the received knowledge in ion optics, ion sources, emittance measurements, charge breeding, etc. and finishing with a pleasant and guiding company in Heckhalle running MAXEBIS, SPARC EBIT and nice time during conferences in Heidelberg and Helsinki.

I would like to thank Prof. Dr. H.-Juergen Kluge for accepting me in the atomic physics division of GSI after which this PhD became possible and also with Prof. Dr. Thomas Stoelker, who took over the atomic business, for the steady support of the HITRAP project.

Gratitudes, of course, go to Dr. Frank Herfurth for help in organizing our work in 2009, for useful discussions, remarks and comments on the thesis, and wonderfull supper in Dresden.

Many thanks to Prof. Dr. Yurii N. Novikov and Prof. Dr. Reinard Becker for wise advices, encouragements, fruitfull discussions and shared experience.

I am very glad to express my sincere gratitude to Dr. Gleb Vorobjev, (upcomning Dr.) Jochen Pfister, Dr. Holger Zimmermann and Sabrina Geyer - our Hackhalle crew isolated outside of the GSI in 2006-2008 to perform experiments.

Of course the HITRAP beam times would not be so successful without already mentioned people and staff from the injector group - Dr. Ludwig Dahl, Michael Kaiser and Dr. Winfried Barth, who are also a perfect company to

play builliard with. Many thanks to Dr. Christophor Kozhuharov and Dr. Peter Gerhard for night shifts spent together in front of the HITRAP control pannel.

Personal thanks to Alexandra Thorn for help to make our charge breeding experiments successful and to Davide Racano for the technical support.

Kind regards and thanks to Prof. Dr. Ronnie Hoekstra and Dr. Gabriel V. Hasan for conducted experiments in KVI and invaluable experimental experience.

Best fishes and thanks for discussions to the Freiburg group: Prof. Dr. Matthias Weidemueller, Dr. Wenzel Salzmann, Simone Goetz and Ina Blank, our close collaborators in planned heavy HCI - MOT target collision experiments at HITRAP.

For assistance and help I would like also to thank Nikita Kotovskiy, Dr. Sergey Eliseev, Dr. Uwe Spillmann and Dr. Danyal Winters.

For the working and friendly atmosphere my gratitudes to the whole AP-group, especially to Dr. Alex Gumberidze and my fellow PhD and ex-PhD students Zoran Andjelkovic, Klaas Brantjes, Sergiy Trotsenko, Stephen Kozhudovski, Giancarlo Maero, Svetlana Fedotova and Mouwafak Shaaban.

For off-GSI activities and perfect time spent in boulings, bars, cinemas, during the grill-parties, journeys and playing football I am especially thankful to Leha Gorda, Toha Lymanets, Vetal' Gostishchev, Serg Litvinov, Max Miski-Ogly, Sasha Patalakha, Katja Kozlova, Sasha Chernii and Tolyan Byelikov. Many thanks goes to my friends Baatar, Zula and Kani for the nice time spent together.

My sincere gratitudes to Prof. Dr. Boris V. Novikov and Dr. Vadim G. Talalaev, my former supervisors during my master study, for the knowledge and experience obtained before the start of my PhD in Heidelberg Uni.

Many thanks to my old friends Pahen, Irisha and Dimas who made my home visits exciting and for always creazy and interesting ideas to spend the vacation time.

And of course my hearty and everlasting gratitudes to my dear mother and father who brought me up and cultivated this "strange" scientific spirit...

List of Acronyms

AO Atomic Orbitals

AOM Acousto - Optical Modulator

BGM Basis Generator Method

BL Bohr, Lindhard (model)

CBM Classical over - Barrier Model

CTMC Classical Trajectory Monte Carlo method

CVC Curren - to - Voltage converter

CW Continuous Wave (mode of operation)

EBIS/T Electron Beam Ion Source/Trap

ECRIS Electron Cyclotron Resonance Ion Source

EOM Electro - Optical Modulator

ESR Experimental Storage Ring

FAIR Facility for Antiproton and Ion Research

FC Faraday Cup

GSI Gesselschaft fuer Schwerionenforschung, Darmstadt, Germany

HCI Highly Charge Ions

HFS HyperFine Splitting

HITRAP Highly charged Ion TRAP

KVI Kernfysisch Versneller Instituut, Groningen, Netherlands

LZ Landau, Zener (model)

LEBT Low Energy Beam Transport section at HITRAP

MCP Micro - Channel Plate

MO Molecular Orbitals

MOT Magnito - Optical Trap

MOTRIMS Technique of ion - atom collision experiment which combines MOT - target and RIM spectrometer

MPS Multi - Passage Spectrometer

PES Photon Emission Spectroscopy

PSB Proton-Synchrotron Booster

PWBA Plane Wave Born Approximation

QED Quantum Electro Dynamics

REX-ISOLDE Radioactive beam EXperiment at ISOLDE

RFQ Radion Frquency Quadrupole

RIMS Recoil Ion Momentum Spectroscopy

SCDD Single Crystal Diamond Detector

SPARC Stored Particles Atomic Physics Research Collaboration

TDC Time - to Digital Converter

TES Transition Energy Spectroscopy

TI Transfer Ionization

UNILAC UNiversal Linear ACcelerator (LinAc)